UNIVERSITÀ
DEGLI STUDI
DI PADOVA

Facoltà di scienze FF.MM.NN.
Dipartimento di Astronomia

SCUOLA DI DOTTORATO DI RICERCA IN ASTRONOMIA

CICLO XXIII

Ph.D. Thesis

Very Fast Photon Counting Photometers for Astronomical Applications

Supervisor : prof. Sergio Ortolani

Co-supervisor: prof. Cesare Barbieri

PhD Student:
Enrico Verroi

«Quindi una nuova percezione dello spazio astrale potrebbe immanentemente prefigurare uno scenario intelligibile di vita aliena nel nostro sistema solare. Ecco perchè è necessario un approfondimento ottico del sistema di misurazione PCA, nella fattispecie X=y/z4pi2 -9 Si, è proprio così.»

CONTENTS

Estratto

Gli argomenti trattati in questa tesi sono la progettazione, l'integrazione e l'utilizzo del fotometro ultrarapido a conteggio di singolo fotone IQuEYE (Italian Quantum Eye). L'implementazione di questo strumento rappresenta un passo fondamentale in un progetto avviato nel 2005 che mira alla realizzazione di un fotometro quantistico, QuantEYE, per il telescopio EELT (European Extremely Large Telescope) di 42 metri di diametro, oggi in fase di costruzione, la cui ultimazione è prevista per il 2018.

Un tale strumento rappresenterebbe una svolta nell'astronomia osservativa, permettendo di estendere le conoscenze sviluppate nell'ambito dell'ottica quantistica teorica e sperimentale all'ambito astrofisico. QuantEYE è progettato per estrarre dalla luce raccolta le informazioni contenute nella statistica di distribuzione spaziale e temporale dei fotoni mediante l'analisi delle funzioni di correlazione di ordine superiore al primo, limite al quale si fermano gli strumenti astronomici "classici".

Lo strumento descritto nella presente tesi, IQuEYE, è un prototipo destinato all'uso su NTT (ESO New Technology Telescope). Si tratta essenzialmente di un contatore di singoli fotoni progettato per raccogliere la luce suddividendo la pupilla del telescopio attraverso quattro canali indipendenti che utilizzano dei rivelatori di tipo SPAD. L'innovativo sistema di etichettatura temporale dei fotoni rilevati si basa su un orologio atomico al rubidio, per corregere la deriva del quale viene usato un segnale GPS interpolato su lunga scala temporale. Tale sistema permette di identificare ogni fotone con una precisione relativa migliore di 100ps ed una precisione assoluta riferita ad UTC di 500ps per un'ora di osservazione. Lo strumento è in grado identificare in questo modo fino ad otto milioni di fotoni al secondo, cioè di sostenere flussi di fotoni fino ad un limite massimo di 8MHz. Tutti i tempi di arrivo, digitalizzati a 25ps, vengono salvati e permettono l'analisi differita e la rielaborazione nel tempo.

La prima parte della tesi è dedicata alla descrizione dettagliata dello strumento, a partire dalla fase di progettazione, il disegno optomeccanico, fino alla sua integrazione.

IQuEYE è oggi perfettamente funzionante ed è stato già utilizzato in tre campagne osservative a La Silla (Cile) durante i mesi di gennaio e dicembre 2009 e luglio-agosto 2010. La tesi raccoglie quindi i risultati di alcune delle osservazioni effettuate e li presenta nella seconda parte, con l'intento di dimostrare le potenzialità dello strumento.

Vengono descritti sommariamente un primo esperimento di fattibilità per l'interferometria di intensità e l'osservazione di un transito esoplanetario che permette di raddoppiare la precisione nella determinazione del periodo di metà transito rispetto agli strumenti utilizzati da altri autori. Per finire sono esposti i risultati ottenuti

nell'osservazione di oggetti rapidamente variabili, tre pulsar ottiche, e alcuni strumenti di analisi dati sviluppati specificatamente. I dati acquisiti hanno una qualità eccellente e hanno permesso di ottenere la miglior determinazione mai conseguita del periodo di pulsazione per PSR B0531+21 (la pulsar della nebulosa del Granchio). Sono inoltre state ricavate le prime curve di luce ottiche da decenni a questa parte per PSR B0833-45 (debole pulsar nella costellazione della Vela, ai limiti di visibilità per NTT) e per B0540-69. In questo modo la validità di IQuEYE nell'ambito dell'astronomia ad alta risoluzione temporale è stata ampiamente dimostrata.

Abstract

The topics treated in this thesis are the design, the integration and the use of the ultra-fast single photon photometer IQuEYE (Italian Quantum Eye). The implementation of this instrument represents an important step in a project, initiated in 2005, for the realization of a Quantum Photometer (QuantEYE) for the telescope EELT (European Extremely Large Telescope) of 42 meters in diameter, now under construction, which is scheduled for completion in 2018.

Such an instrument would represent a breakthrough in observational Astronomy and it would allow extending the knowledge gained from theoretical and experimental Quantum Optics to the Astrophysics. QuantEYE is designed to extract from the light collected the information enclosed in the statistical distribution of photons through spatial and temporal analysis of the correlation functions of order higher than first, beyond the capability of "classics" instrumentation.

The instrument described in this thesis, IQuEYE, is a prototype for NTT (ESO New Technology Telescope). It is essentially a fixed aperture photometer that collects light within a field of view of few arcseconds, dividing the telescope light beam into four equal parts, and focuses each sub-beam on an independent single photon-counting diode SPAD. The innovative photon time-tagging system is based on a rubidium atomic clock, corrected on long time scale the by means of a GPS signal. This system allows the identification of each photon with a relative precision better than 100ps and an absolute UTC precision of 500ps for an hour of observation. The instrument can identify in this way up to eight million photons per second, that means IQuEYE is able to sustain flows of photons up to a maximum rate of 8MHz. All arrival times, digitized at 25ps, are stored, in this way post-processing analysis and data reprocessing in time are allowed.

The first part of the thesis is devoted to the detailed description of the instrument, starting from design phase, with particular attention for optomecanics, to its integration.

IQuEYE is now fully operative and has already been used in three observation campaigns at La Silla (Chile) during the months of January and December 2009 and July-August 2010. The thesis then collects the results of some observations performed and presents them in its second part, with the aim of demonstrating the potential of the instrument.

So a brief description of a first experiment for the feasibility of intensity interferometry is given. Moreover the observation of an exoplanetary transit which allows us to double the accuracy in determining the period of mid-transit, is described. Finally the results for the observation of rapidly varying objects (three optical pulsars) are exposed, together with some analysis tools developed specifically for our data. The acquired data have an excellent quality. Through their analysis the best determination

of the Crab pulsar (PSR B0531 +21) period was achieved. Furthermore the optical light curves for PSR B0833-45 (weak pulsar in the Vela constellation, at the limits of visibility for NTT) and B0540-69.

In this way the validity of IQuEYE in HTRA High Time Resolution Astronomy has been demonstrated.

Introduction

This thesis is inserted in a broader framework of a proposal initiated in 2005 for the realization of a *quantum photometer*, QuantEYE, dedicated to the 100m ESO* telescope: OWL, the OverWhelmingly Large Telescope.†

Today, in the meanwhile, the OWL project was scaled down to 42m diameter telescope and the project is now called European Extremely Large Telescope (EELT), for which the completion is planned for 2018.‡

QuantEYE was designed to be the highest time-resolution instrument ever; it was conceived to explore astrophysical variability beyond the micro and nanosecond scales, down to the quantum-optical limit and to the single-photon distribution analysis. Many discoveries come from high time resolution Astronomy and the availability of EELT equipped with instruments able to overcome the microsecond threshold could improve the current science timescale of one or more order of magnitude, as well as allow the observation of targets orders of magnitude fainter than those observed today.

But QuantEYE is not only planned to be a better instrument mounted at a larger telescope, but actually to allow the use of photons in a new, almost unexplored, perspective: the ambitious aim of QuantEYE is to represent a turning point in the observational Astrophysics, allowing a new way of looking at the universe.

In fact all existing astronomical instruments that analyze electromagnetic radiation (and this represents the primary way to obtain information from the universe) measures or the directions of photons incoming (and they produce images) or their energy (spectrum) or their number and the number fluctuations on certain time scales (photometry), or polarization or combination of these properties. But the development of quantum optics through theoretical studies and laboratory experiences has led us to understand that in photons may be encoded more information. Where and What?

"*Each photon interferes only with itself. Interference between two different photons never occurs.* " wrote Dirac.§

In other words, the possibility of detecting a photon is only due to its single probability function. Instead it was shown that under certain conditions, the probability of finding a second photon at a given time or a certain position is somehow related to the presence of the former. This means going beyond the concept of photons as separate units and analyze their mutual correlation. And in the correlation of photons, information

* European Southern Observatory.
† For details the reader is referred to [*owl*], in the sitography.
‡ See [*elt*] for further information.
§ P.Dirac in "The Principles of Quantum Mechanics" §.1

about their origin (which type of source, the mechanism by which they were generated) and their history (which processes they underwent during propagation) can be deduced. This concept will be deepened in §.4.

No classical instruments analyze this correlation, that is, instead, the purpose of the so-called Quantum Astronomy.

But the extension of Quantum Optics to Astronomy struggles to take off, because a very limiting requirement is a large flux of photon not achievable by the size of existing telescopes. Notwithstanding the quantities related to the quantum effects grow with the square of the telescope area (i.e. the fourth power of radius) or with even higher powers, so the incisiveness of these second-order effects has a steep increment with telescope radius increasing. The design of QuantEYE involves 100 parallel channels, each sampling a portion of the telescope pupil and capable to time-tag single photons detected with accuracy of the order of 10ps.*

The requirements for an instrument such as QuantEYE are really stringent: with the flux allowed by a collecting area of 1300 m^2 to study timescales down to nanoseconds, there is the corresponding need to sustain photon acquisition rates up to some GHz.

At present there is no experience on such completely new concept instrument, so, the road that leads to a real quantum photometer must be faced in steps.

The first step was the implementation of a small prototype named AQuEYE, the Asiago Quantum Eye, for a 1.82m Italian telescope. With that project the basic technology has been developed as well as the necessary know-how. We gained knowledge of the field and the potentiality of the instrument has been demonstrated† making us ready for the next step.

So the main aim of this thesis was to design, integrate and use a prototype of instrument such as QuantEYE. A very fast photon counting photometer for ESO New Technology Telescope NTT: **IQuEYE**, the Italian Quantum Eye. The instrument is now fully functional at the NTT and it has been used by us in three observation campaigns in January and December 2009 and in July and August 2010.

The thesis is divided in two parts: the first is devoted to the description of the instrument, while the second —functional to prove the validity of this instrument concept— contains three chapters related to the observations and the results obtained, including a brief overview of what an instrument like IQuEYE could get.

All the analyses that have lead to the actual design of IQuEYE are described in chapter One, where the observational requirements, the kind of single-photon detectors available and the telescope characteristics that dictate the structure of the instrument are analyzed. Then the complete design is illustrated and discussed, with particular attention to the optical part, which was my main occupation in the course of this thesis. Also the mechanical design is treated, and, in the second part of the chapter, the

* Full description in [QE1], [QE2], [QE3].

† See for ex. [IQ3], [IQ10], [IQ12].

acquisition system. Assigning a precise time-tag to each photon detected is a very difficult operation, so the acquisition and timing solutions we have implemented are described along with software for the data treatment.

Chapter number two treats the analysis of the IQuEYE components and presents a brief outline on the integration and alignment activity performed in 2008 and 2009. The chapter concludes analyzing the expected instrument performances.

Chapter Three concludes the first part of the thesis. There, a revision of the instrument is treated. Some improvements and the reasons led us to implement them are therefore described.

In chapter Four an overview on basic issues of quantum optics is presented. As anticipated, the instrument, due to its prototype nature, does not allow a real "quantum" approach to astronomical observation, so the chapter aims to introduce the topics that would be the final QuantEYE goals. In one section, in particular, the intensity interferometry is presented and the software development for the correlation of long strings of data (the time-tags of photons), with sub-nanosecond temporal resolution, is described. Furthermore a brief discussion is given on which may be the benefits introduced by using an IQuEYE-like instrument: the capability of storing the raw data acquired, which enables the post processing analysis and allows to abandon the need for a direct link between the telescopes involved.

Chapter Five is devoted to a theme not entirely tied to the high time resolution photometry: the detection of exoplanets. After a brief introduction to the topic, a preliminary analysis of some results obtained during the last observing run at NTT (July-August 2010) and still under study, is presented.

The thesis concludes with chapter six, the only that presents real scientific results. This chapter finally comes on subjects fully in the domain of this instrument and it presents the observations of Crab, Large Magellanic Cloud and Vela pulsars performed along the three observation campaigns. Concepts are introduced for the analysis of periodic signals from these targets and the results obtained through different techniques, some standard, some developed for this purpose, are exposed.

At the end a brief outlook is proposed.

PART ONE - IQuEYE

1 Optomechanical Design

IQuEYE is a single photon non-imaging photometer for visible band, based on single photon avalanche diodes technology.
It splits the telescope pupil in four collecting areas and it gathers the light with four independent channels. This architecture, combined with the wide dynamic range and the ability to save the arrival time of each photon detected, determines the great versatility of the instrument, as will be shown. This chapter will propose a full description of the instrument, starting from the main components that led us to develop its current design.

1.1 Preliminaries for the design

1.1.1 The detectors

The crucial element around which the instrument is constructed is the single photon detector for this kind of application. The detector structure determines the rest of the instrument design: the opto-mechanical architecture, the control systems and the devices for the acquisition and storage of the data, even up to the analysis software of the same. We considered several photon counting detectors, but at the present state of the art do not exist (yet) a detector which really fulfilled our scientific requirements. The ideal solution is a photon counting imaging-array detector directly placed at the telescope focus. Each kind of detector taken in account during the design phase presents some weakness or drawbacks that do not meet our needs.

The image intensifiers coupled with either CCD or CMOS sensors has a poor time resolution completely incompatible with our purposes. MCP-based detectors [DAT],* have extremely good temporal resolution (few tens of picoseconds), but are limited by the maximum count rate of a few kHz and by low efficiency in the visible band. At present a second generation H33D MCP-based photon-counting detector [MI1], [MI2] is developing and has expected time resolution of the order of 250ps and maximum count rate around 20 MHz but it was unavailable at the time of the design of IQuEYE. Other detectors considered, as the SPAD-A (arrays of single photon avalanche photodiodes) have good count rate limit and timing accuracy, but a very small fill-factor and, most of all, a quantum efficiency really low [NIK], [BOI].

Our ultimate choice was to penalize the imaging aspect of the instrument in favor of, instead, the aspects related to the quantum efficiency and the time-tag capability. Among the count, the detector that is closest to our needs is the Single Photon Avalanche Diode (SPAD).

* Bibliographic references are indicated by capital letters in brackets. Lowercase letters indicate references to websites.

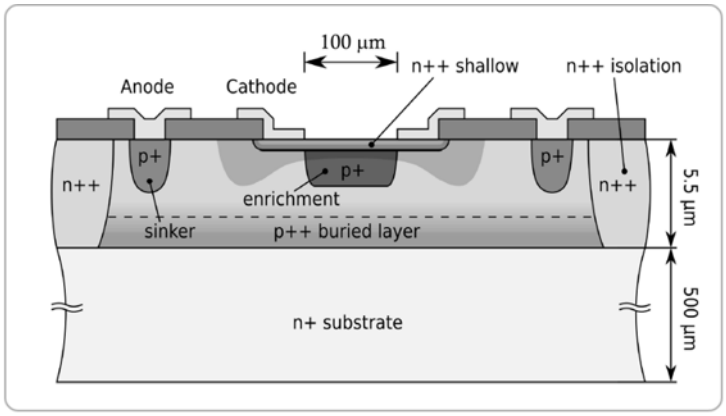

Figure 1: Cross-section of the planar SPAD structure. Image adapted from [REC]. The sensitive area is indicated by the 100µm quote.

A SPAD is a Geiger-mode avalanche photodiode based on a reverse *p-n* junction, biased above the breakdown limit, in which a photo-generated charge carrier causes an avalanche current. So the avalanche, generated on picoseconds time scale, indicates that a photon has interacted with the device. Thermally generated carriers cause an avalanche too, originating in this way the detector noise (or dark counts). This kind of detector grant an extremely good timing accuracy, have quantum efficiency peak around 50%, and low dark count. Like the others, SPADs too have their drawbacks: the cross-talk between the sensors does not allow the possibility of a matrix of pixels and so, they are single-pixel detectors with a tiny sensitive area (30÷200 µm) very difficult to couple with the target image given by a large telescope. The dimension of this area makes very critical the integration and alignment of the optics. After each detection, an active quenching circuit has to stop the avalanche, by lowering the bias voltage and has to restore the initial condition for a new photon interaction. During this phase (called dead time) the SPAD is blind and unable to detect any photon. The selected Geiger-mode SPAD detectors are produced by the Italian company Micro Photon Devices and has a ~75ns long dead time. The limitations caused by a so long inactive period of the detector are particularly harmful for High Time Resolution Astronomy (HTRA) and quantum applications, where photon statistics must be measured. For this reason the instrument was conceived introducing a splitting of the light from the telescope in four distinct channels, each feeding an isolated SPAD. In this way the problem is partially overcome; in fact the statistical distributions of events over the four channels allow the recovery of many events otherwise lost. This effect is depicted in Figure 2 where the curves shown are histograms of the time differences between contiguous time-tags of the photon detected. The histogram bins are 1ns long and the top panel shows the single SPAD situation in which there are no events separated for less than 75ns, i.e. the dead time value. The partial recovery of the signal is, instead, clearly shown in the bottom panel, where the differences between consecutive events in the case of four SPADs are considered. In those cases the photon rate is quite high

and four SPADs are not even sufficient to eliminate the effect of dead time. Further details on the SPAD devices used in IQuEYE are presented in [COV].

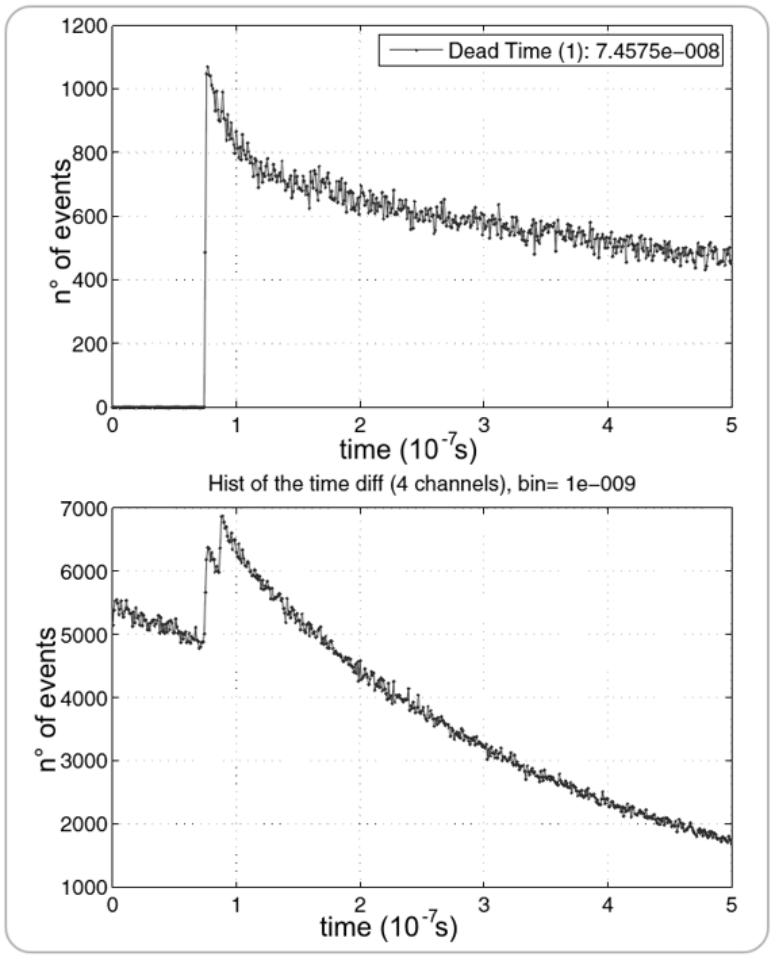

Figure 2: single detector and four-detectors comparison. Histogram of the arrival inter-times (see text). **Top:** one SPAD. **Bottom:** four SPADs.

.

1.1.2 AQuEYE

During the early phase of the design realization, we took into account different structural constraints, in large part coming from lessons learned in the implementation of a prototype instrument realized in the years 2006-2007 for a 1.8m telescope (Details about the instrument in [IQ8] and [IQ9]). The conceptual design of this prototype called AQuEYE (Asiago Quantum EYE) has the same basic ideas of the IQuEYE design: through a mirror pyramid put where the beam coming from the Telescope is diverging, the light is split into four independent optical paths (two of them shown in the cross-section of Figure 3). The beams reflected by the pyramid are independently sent along four perpendicular directions and each of them is collimated by a suitable lens. At this position filters or polarizers can be inserted, and then the beam is focused by means of a second lens on a SPAD. The detectors used are four 50μm SPADs produced by the MPD Company (Micro Photon Devices - Bolzano, Italy).

AQuEYE saw its first light at the 182cm telescope of Cima Ekar (Asiago, Italy) the 20th of June 2007. This telescope offered a good availability of observing time and an excellent test ground for the development of this completely new concept instrument. AQuEYE was mounted on AFOSC (Asiago Faint Object Spectrograph and Camera): a focal reducer type spectrograph/camera installed at the f/9 Cassegrain focus. AFOSC utilities afford the direct link to the telescope without a necessity of equipping the instrument with a focal reducer. Furthermore it had two filters and grisms wheels available, which made unnecessary implementing additional filters in AQuEYE, except those for single channels. The instrument does not have its own system of pointing, tracking and monitoring the sky; for these operations the telescope facilities are used.

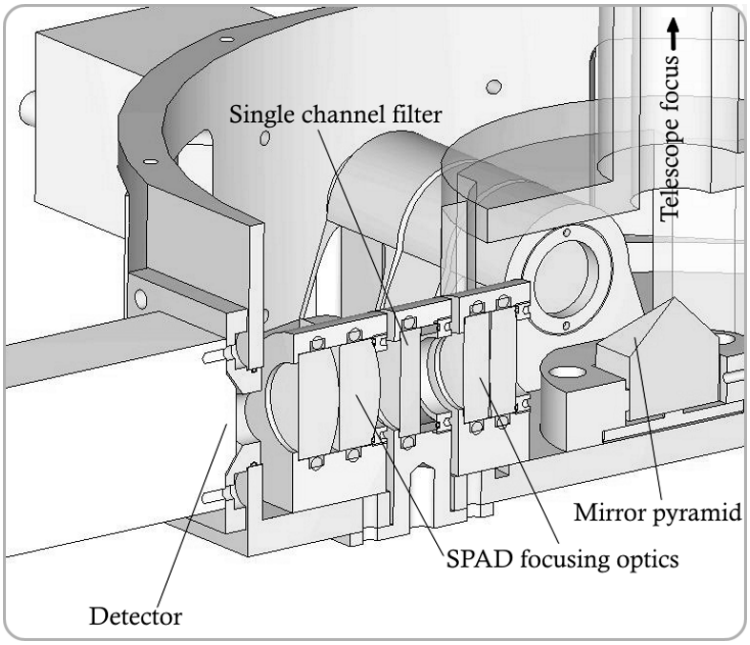

Figure 3: Schematics of AQuEYE design. The concept is the same of IQuEYE: a pyramid splits the beam incoming from the telescope focus and subdivides it in four channels (two shown). Each channel is focused through an optical train on a Single Photon Avalanche Photodiode.

To avoid spurious signal enters the instrument an entrance pin-hole is used on the telescope focal plane (actually AFOSC focal plane), its dimension corresponds to 3arcsecs in sky.

1.1.3 Seeing

Over many observation runs at Asiago telescope, we found some trouble related with the single-pixel configuration of the instrument. In particular we observed unexpected anomalous fluctuations of the incoming flux of photons. An example is shown in Figure 4: the photons detected by observing the star G29-38 is binned in intervals of 0.1 s and the intensity of the star in function of the time is reconstructed. The star in question is a ZZ Ceti type variable white dwarf with period longer than 600s, so the variability of the star does not interfere with the short acquisition and is not the responsible for the large fluctuations.

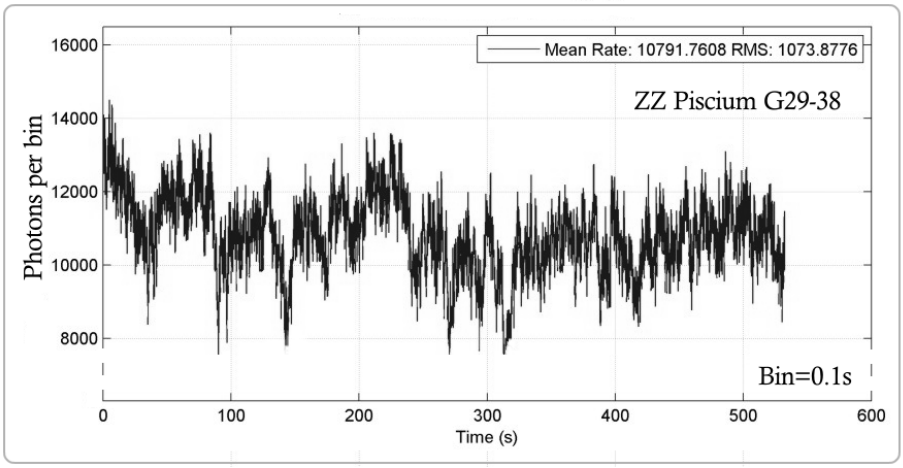

Figure 4: signal from G29-38 detected by AQuEYE at cima Ekar observatory in about 500s of acquisition, binned at 0.1s intervals.

The depth of the fluctuations is very variable and depends on the seeing conditions, the intensity and the position of the targets. The fact that, in some occurrence, the Fourier transform of the signal gave an unexpected peak between 0.12 and 0.15 Hz, that coincide with the refreshing frequency of the telescope tracking system, suggested us to investigate the role of the pin-hole on the focal plane of AFOSC as possible responsible of the fluctuations.

To understand this kind of optical problems, we turned to data obtained with another instrument used by an IASF* CNR group of Milan, at the Asiago 1.8m telescope. The instrument is a PC-ICCD, a photon counting intensified CCD, optimized for observation in the optical band, based on a high-gain Micro Channel Plate image intensifier, read out by means of a CCD optically coupled to a phosphor screen. In practice the phosphor intensifier is linked to a photocathode and converts each photon detected by the latter into a luminous spot on the phosphor screen that is reimaged onto the CCD. The reading out frequency of the CCD can be pushed up, through a windowing mode, to 220 Hz. The frames are then analyzed in real time by a digital electronic device based on an FPGA (Field Programmable Gate Array) unit, and for each event produced by the photoelectrons in the photocathode, a time tag with time resolution of 4.5 ms and an XY coordinate on the CCD is stored. Further details on the instrument is given in [US1] and in [US2]. In this way, except for the absence of AFOSC it is possible to reconstruct (although with less resolution in time) the behavior of the targets in the focal plane of the same telescope, that is the plane where the pin-hole of AQuEYE lies, with a field of view of 30 arcsec diameter and a spatial resolution, after the windowing, of 0.78 arcsec per pixel. While AQuEYE has no imaging possibility, this CCD instrument allows us to see how the light from the star is spread by the atmospheric seeing and by the telescope vibrations, and then we

* Consiglio Nazionale delle Ricerche, Istituto di Astrofisica Spaziale e Fisica cosmica, sez. Milano

can understand how and how much the signal would be cut off by the presence of the pin-hole plate in the focal plane. We emphasize that, obviously, in the simulation is not relevant that the spectral response of the two instruments is very different, as well as their quantum efficiency.

Here it is presented the data obtained from an observation 20 minutes long of the star PG0911+456, a subdwarf B pulsator with period longer than 160 s and amplitude of the pulsation of few mmag [KOE] that, for us, is a simple test star to replicate a plausible signal entering AQuEYE.

The original intensity signal given by the PC-ICCD (integrated over 15x15 arcsec^2 FoV) does not present macroscopic fluctuation, so the data acquired for a large FoV was used to simulate the AQuEYE single-pixel configuration and to explain the unexpected intensity fluctuations (as those in Figure 4).

After a sky\noise subtraction, a preliminary analysis of the target returns a seeing* of 3.7 arcsec over 20min of integration. In particular the 20 minute image is slightly elliptical and the FWHM along the two axes of the CCD are faintly different (3.6 arcsec along the X axis and 3.9arcsec along Y); the X axis correspond with the right ascension direction, and that ellipticity is explained by observing that the tracking correction in RA is the most frequent, so the star centroid fluctuates in α direction of a few tenths of arcsec. Unfortunately the Asiago cima Ekar telescope is not equipped to perform seeing measurements independently from the main instrument and, since AQuEYE is not able to provide image, it is not possible to go back to the precise measure of the seeing during the observation nights, and is only possible to obtain a rough estimation through the tracking camera. 3.7 arcsec corresponds to slightly bad condition not very far from the "average" conditions.

To understand how the signal from PG0911 would be detected by AQuEYE, we have implemented a code in IDL (Interactive Data Language) that reads the stream of data stored by the ICCD, centers a simulated pin-hole in the star centroid (calculated over the whole acquisition period) and treats the data subtracting the photons not entering the pin-hole.

Figure 5 contains 15 frames from data obtained with the ICCD and elaborated with that code. The dashed circle represents the position that the pin-hole would have if AQuEYE was positioned on the telescope focal plane.

* Precisely we refer to the FWHM of the photons distribution.

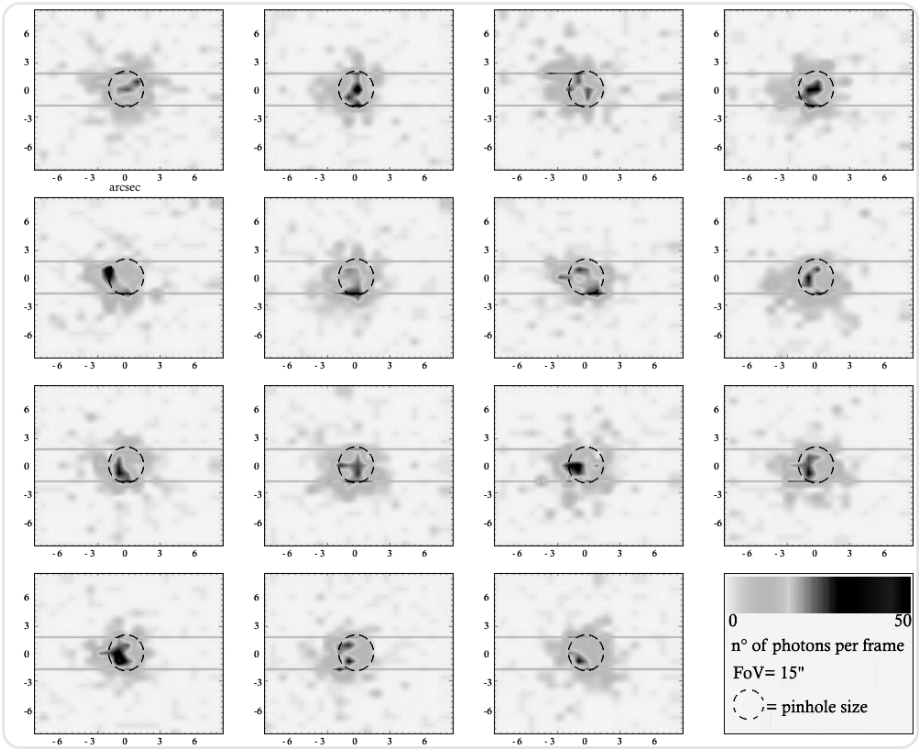

Figure 5: Some Frames from PG0911+456 obtained whit the PC-ICCD. Each frame represents a field of 15x15 arcsec^2 in the sky and collects the photons detected in 0.5 s. Only the photons in the dashed circle would be detected by AQuEYE.

The upper panel in Figure 6 represents the simulated intensity signal obtained cutting off the photons outside the pinhole area. The data are binned at $\Delta t=1$ s. The fluctuations have a standard deviation that is about the 17% of the mean intensity and are well visible in the figure. In the same figure, the lower panel shows the original data not shielded by the pinhole plate, integrated over a FoV of 15 arcsec and binned with the same $\Delta t=1$ s .

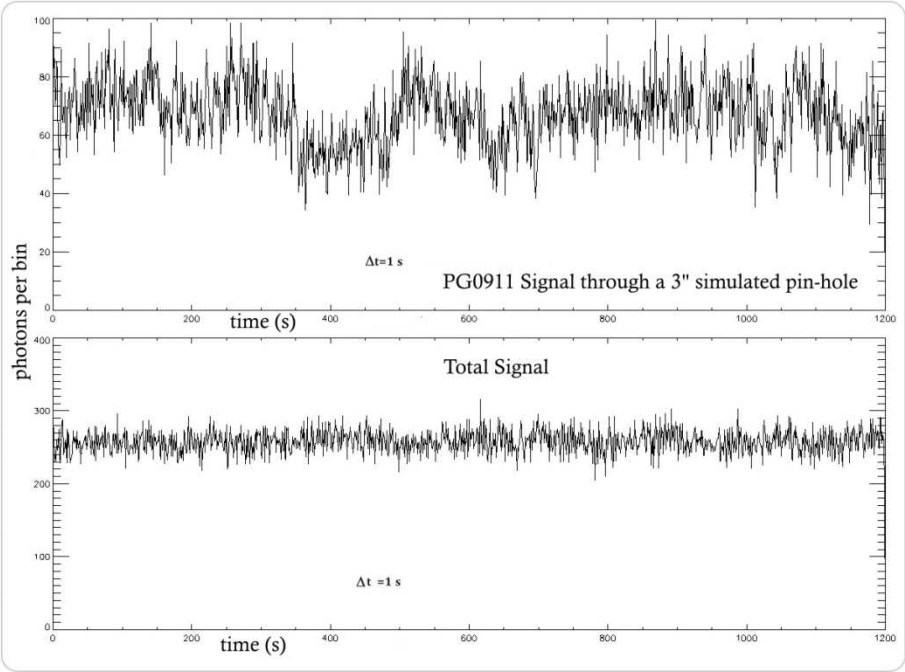

Figure 6: Intensity of PG0911+456. The upper panel simulate the signal as it was detected downstream of a 3" pin-hole. The lower panel shows the same signal without any kind of screen, integrated on a FoV of 15x15 arcsec^2. In both cases the time bin is Δt=1s.

The analysis shows that, for those seeing conditions, more than 65% of the photons are stopped by the pinhole plate. The results are summarized in Figure 7, where the fraction of photons detected is plotted in function of the pinhole diameter. In particular, the pinhole diameter required for collecting the 90% of the flux from the target is around 8 arcsec in sky.

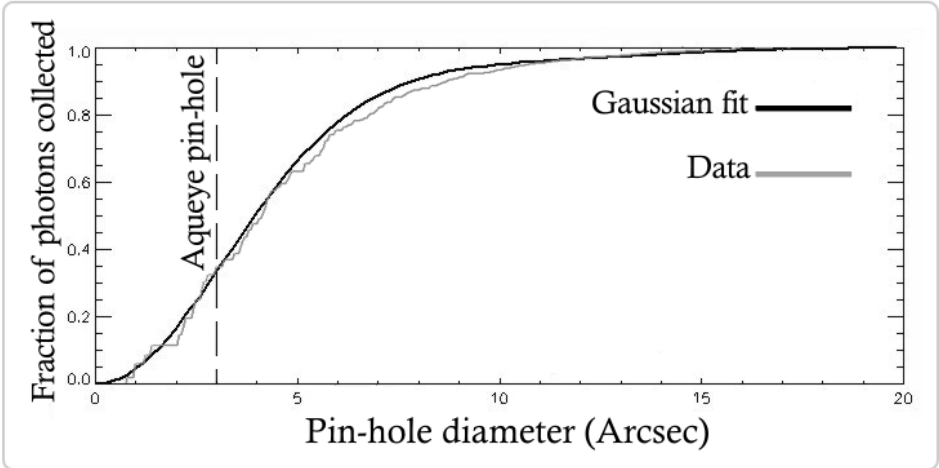

Figure 7: Fraction of photon collected in function of the pin hole diameter. The pin hole is considered to be centered in the position of the star centroid calculated over 20mn of exposure. The gray line represents the photon number obtained from the real data from the ICCD, the black line represents the photons fraction obtained from the Gaussian fit of the star intensity profile.

The Table 1 summarize, for ease of reference, the main results obtained from the PC-ICCD data with the simulation.

Table 1: Summary of the main results from IASF PC-ICCD data analysis	
target	PG0911+456
Total time of observation	20 min
FWHM Xaxis	3.6”
FWHM Yaxis	3.9”
% photons entering 3” pinhole	35%
Pinhole size required to collect 90% of the signal	8”
St.dev% for t bin=0.5s	21%
St.dev% for t bin=1s	17%
St.dev% of the original signal (without pinhole) t bin=1s	5%

Concerning the seeing, Asiago is a rather bad site whit averages around 3 arcsec. The seeing conditions in La Silla (Chile) are quite better, as will be shown in the next subsection.

1.1.4 NTT site seeing

Limiting the field of view with a diaphragm that eliminates the contributions coming from the field, that is the light from the surrounding sky or sources, and any contribution due to internal reflections in the instrument, is essential to make a good photometry. On the other hand, a field of view too limited leads instead, as has been demonstrated above for AQuEYE, to a loss of photons that are part of the signal. To determine the correct field of view to be assigned to IQuEYE, we analyzed the average seeing expected for NTT, using data provided by ESO La Silla Astroclimatology database [*eso*], collected on more than 20 years of acquisitions in the site (here updated to 2009). That monitoring of seeing in La Silla is obtained by Differential Image Motion Seeing Monitors, for further details we refer the reader to [SAR]. Figure 8 represents the monthly seeing averages acquired since 1988 through exposures 20 minutes long. From the figure it is possible to get an idea of the dimensions at stake; Figure 9 shows some statistics of seeing conditions, a frequency histogram and a cumulative frequency curve. Almost all the data are behind the threshold of 1.2arcsecs. Since an average obtained over a month resets the daily fluctuations, further analysis was performed considering the 2005daily data. The results obtained are not much different from those shown in the diagrams and, in particular, tell us that the 90% of the nights has a seeing lower than 1.5” (with seasonal variations that will not be considered here).

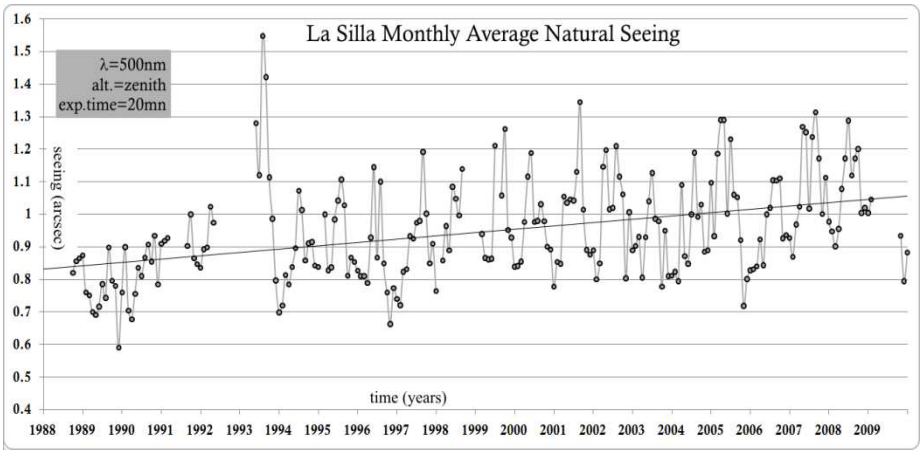

Figure 8: Monthly average natural seeing measured between the years 1988 and 2009. The data is provided by ESO astroclimatology database [*eso*], the measure of the seeing is obtained by Differential Image Motion Seeing Monitors (DIMM and DIMM2). The exposures for the seeing measure are 20 minutes long and taken at the zenith. The average wavelengths considered is λ=500nm.

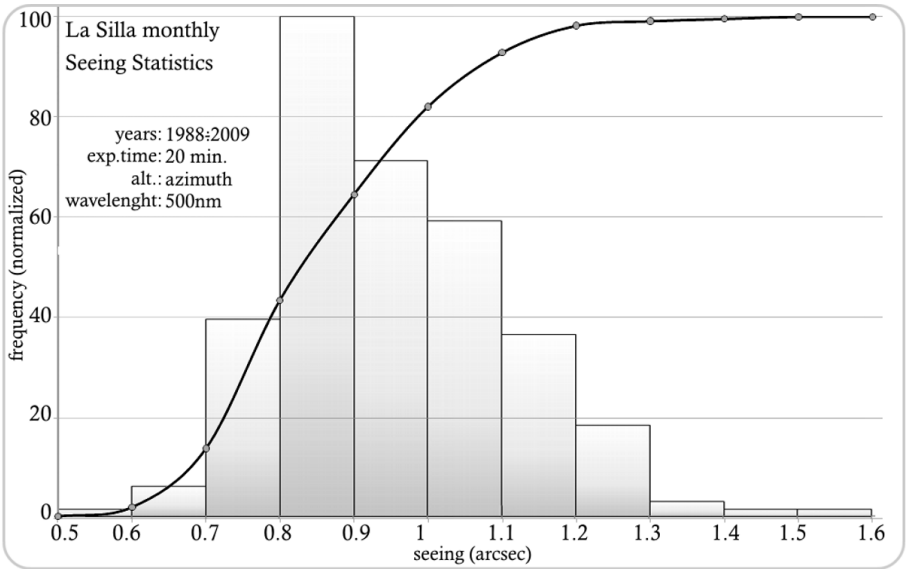

Figure 9: Statistics for the natural seeing at the NTT site (La Silla, Chile). The data is provided by ESO, the measure of the seeing is obtained by Differential Image Motion Seeing Monitors (DIMM and DIMM2) during the period between the years 1988 and 2010 with few interruptions (as depicted in Figure 8). The exposures for the seeing measure are 20 minutes long and taken at the zenith. The wavelength considered is λ=500nm.

We used the same software developed for the analysis of the PC-ICCD data to model a function of seeing and reproduce the effects of the diaphragm (hereinafter called pinhole) with variable diameter on the flow of photons from a source. In these simulations a source centered in the pinhole has been considered and, furthermore, possible centering variations due to the NTT tracking system corrections was taken into account, by considering an largely overestimated value of the fluctuations with maximum amplitude of 0.5". The total fraction of photons collected by a pinhole placed on a focal plane, in function of its diameter for four different values of seeing (0.8", 1", 1.5", 2"), is shown in Figure 10. It is clear that

for a seeing value around 1.5” the pinhole diameter necessary to collect 90% of signal is little less than 3”.

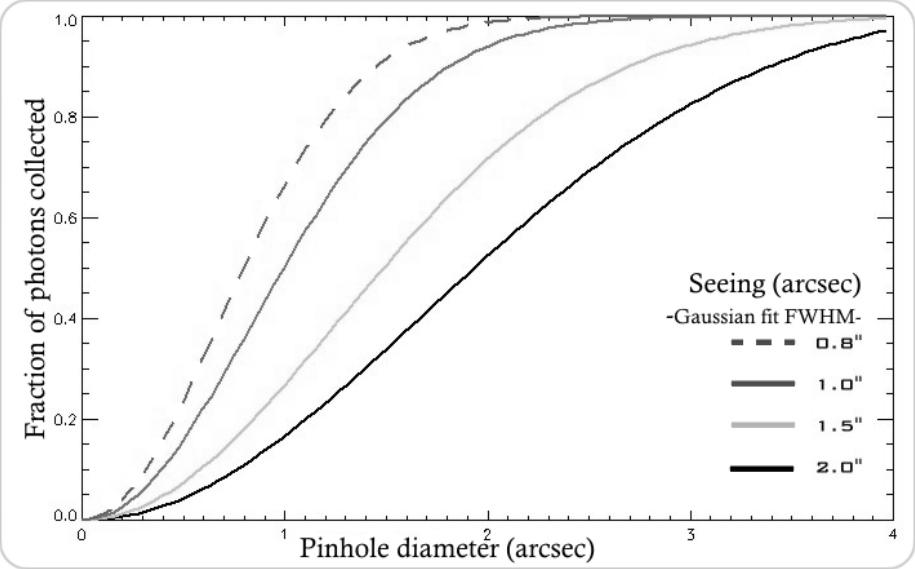

Figure 10: encircled energy (fraction of the total photons) collected through a circular aperture in the focal plane in function of its diameter. The fraction of photons is plotted for four different value of the seeing. The values listed in label refer to the FWHM of the Gaussian fit considered.

Depending on the target and the seeing conditions, the optimal settings for observing are variables, because the goals to be achieved change. Thus, for example, in the case of pulsars observations the field of view should be restrict to the minimum in order to reduce the signal to noise ratio and cut off the contribution of the bright nebula which surrounds the target. In other cases it is better not to reduce the noise in favor of an increase in the ratio between signal acquired and signal lost, avoiding to lose any fluctuations in the seeing tails. An example is furnished by the observations of exoplanets in which the parent star is very bright and the noise contribution from field is negligible. In fact, in many photometric acquisitions, procedures involve the defocusing of the target.

In order to increase the versatility of the instrument we decided to use a selectable pinhole with three diameter sizes available: 3.5, 5.2 and 8.3 arcsec, where the one with 8.3” diameter, with the actual optical configuration of the instrument, exceeds the corresponding dimension of the detector single pixel and, so, it does not represent a real field stop.

1.2 Optical design

The optical design of IQuEYE has a concept quite simple. With reference to the Figure 11, IQuEYE is linked to the telescope on the left side. The dashed line represents the NTT Nasmyth focal plane, where a holed field mirror positioned at 45°deflects the light from the telescope, sending it to a field camera. So the image of the field around the target star is focused by a photographic 60mm objective on the CCD. The light from the

target object, instead, passes through the conical hole in the mirror, continue to the right (still following the drawing) and here it is collected by a focal reducer. Between the two optical trains of doublets composing the reducer, two filter wheels are located in a collimated portion of the beam. The wheels allow the selection of different filters or polarizers described in the follow.

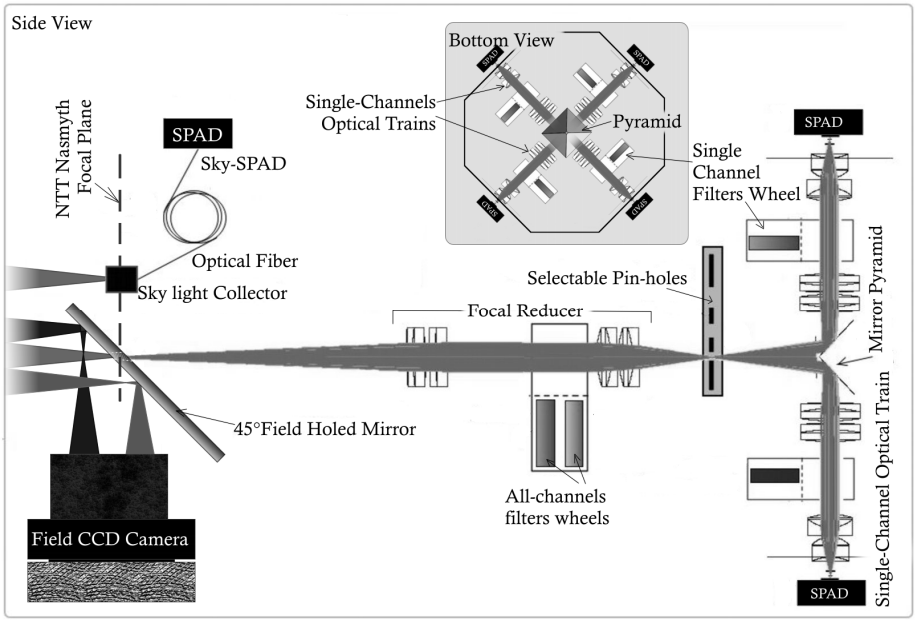

Figure 11: Schematics of optical designs. The ray tracing is superimposed on a schematic representation of the main elements. The gray rectangle on top shows a view of the part that contains the mirror pyramid and the four arms. NTT interface is on the left side.

After the second optical train the beam is refocused in a new focal plane where the image is demagnified by a 3.25 factor, compared to the telescope focal plane. Within this intermediate focal plane, one of three pinholes can be inserted. Taking in account the 5.36 arcsec/mm nominal NTT scale factor at the Nasmyth focus and considering the requirements analyzed in the previous section, their dimension was chosen to be 200, 300 and 500μm diameter, which, as said, correspond to fields of view of 3.5, 5.2 and 8.7 arcsec in sky. After the pinhole, the beam is split in four channels through a pyramid with four mirror surfaces. The truncated tip of the pyramid lies in the center of the shadow of the secondary mirror, as the section of the beam, till there, is a holed circle. The pyramid divides beam into four equal asymmetrical portions (the perpendicular section of the beam is a quarter of circle with the cape truncated, a ray tracing cross section of the beam taken where the single-arm filters are inserted in the optical path is shown in Figure 12).

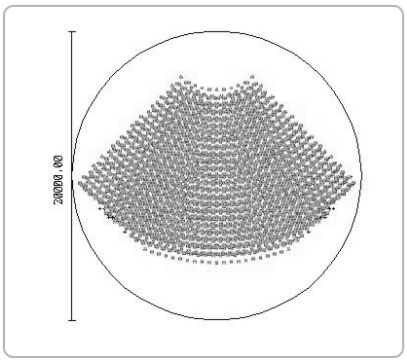

Figure 12: Shape of the beam at the single-arm filters position. The diameter of the circle is 200mm.

In this way the Telescope pupil is subdivided into four sub-pupils that can be used as different telescopes, because they feed four different detectors. The four perpendicular arms are each refocused by four couple of optical doublets, which further demagnifies the image by an additional 3.5 factor, over the SPAD. In the collimated portion of each beam is placed a filter wheel with 5 filters available (4+1clear) for multiband photometry. Considering the total factor of magnification produced by the focal reducer and arm optics, the SPAD circular sensitive area defines a Field of view of 6.1 arcsec, acting as a field stop in the case of the larger pinhole. For this reason the 8.3" pinhole is mainly used for alignment or calibration purposes. The intermediate one (5.2") is the default pinhole, usually selected for the standard operating condition because it is more closely matched to the both detector and seeing, and also accounts for the effects of the small spot broadening caused by system residual aberrations.

Because of these not too stringent optical requirements, it has been possible to design the optical trains using only commercial spherical lenses, yet still obtaining almost optimal performance.

Actually, after the first observations campaign at the telescope, we decided to replace the last two doublets of each arm with two custom spherical lenses to improve the optical performance. In this second integration phase was also added a fifth SPAD for the monitoring of the sky (see 3.1.1), shown in Figure 11, top left. Through a 6mm lens, the light from a portion of sky corresponding to 8arcsec (of which only the four central are not vignetted) is injected into an optical fiber that feeds the fifth SPAD.

1.2.1 Ray tracing

In the optical design we took into account several solutions with commercial lenses, all based on some fixed points: the final demagnification expected; the space needed for other structures (as the movable slide for the pinholes, the pyramid or the field mirror and its post); the need to have portions of beam collimated, in the focal reducer as in the individual arms, where to place the filters so that the rays hits perpendicularly their

surface. The ray tracing has been built with the software ZEMAX (Zemax Development Corp.) and the solutions analyzed in order to determine the performance of each configuration developed. Table 2 indicates some models considered. The first column (Dem) shows the optical train demagnification achieved by each individual channel (i.e. the demagnification of the focal reducer is not listed). In the second column it is indicated the RMS of the spread for a spot on the detector plane produced by a point-like source in the telescope focal plane (that is the RMS of the point spread function PSF). The spread is caused by the sum of all aberrations in series in the whole system. In the third column the fraction of energy collected from a circular area having diameter 100 μm, is indicated (EE). Again the source considered is a point. Some comments taken during the design phase are listed too and they indicate pro and cons of every configuration.

Table 2: Characteristics of some optical designs. Demagnification of the four arm lens trains (Dem), RMA spot size in μm on detector surface (RMS), SPAD detector Encircled Energy (EE).

Dem	RMS	EE	comments
4.2	39	0.971	All 25 mm diameter lenses. Beam footprint at 0.5 mm from the lens edge
4.2	38	0.972	40 mm focal reducer lens diameter; 25 mm the others. Beam footprint at 0.5 mm from the lens edge
4.2	38	0.976	All 40 mm diameter lenses with the exception of the last two (25 mm). The beam footprint here is slightly trimmed.
4.2	50	0.93	All 40 mm diameter lenses. Bad performance at the last two lenses
3.6	55	0.83	Changed last two lenses (Optosigma), but still bad performance
4.2	59	0.76	Changed last two lenses (Ross Optical), but still bad performance
4.2	39	0.956	All 40 mm diameter lenses except last two(30 mm).
5	41	0.914	All 40 mm diameter lenses except last two(30 mm).
3.1	50	0.936	All 40 mm diameter lenses. Reduced magnification of the last section
3.75	55	0.844	All 40 mm diameter lenses. Changed magnification of the last section: aberrations increased
3.33	42	0.991	All 40 mm diameter lenses with the exception of the last two (25 mm), as version 03. The first couple of lenses is too close to the pyramid...
3.73	39	0.983	All 40 mm diameter lenses with the exception of the last two (25 mm), as version 03. The first couple of lenses is 15 mm from the pyramid.... and the footprint ends at 2 mm from the lens edge
3.73	40	0.972	All 40 mm diameter lenses with the exception of the last two (30 mm), as version 03. The first couple of lenses is 15 mm from the pyramid...

In Figure 13 a spot diagram is shown: it represents a section of the ray-tracing taken on the focal plane of the instrument (i.e. the SPAD sensitive surface). The ray tracing is performed in 4 different wavelengths: 420nm, 520nm, 620nm and 720nm. The figure describes how the light rays coming out from a point-like source placed on the telescope plane are spread passing through the lenses. In particular the source considered in figure is composed by 5 polychromatic point-like sources placed each at 1arcsec from the others. One in the center of the field of view, two along the y-axis and two along the y-axis, simulating a 2arcsecs extended source.

The asymmetry induced on the beam profile by the pyramid make the spot diagram slightly elongated in the X direction, most of all for the V band light. This is due to the fact that the peripheral parts of the lenses induce more aberrations and the beam section is larger along the x-axis.

In this case (if the target is perfectly centered) almost all the rays are collected. It is however also evident that in case of larger spread of the source, for example because of the seeing, a very small amount of the beam exits the SPAD. In Figure 14 a 5arcsec extended source is simulated by five point-like source placed at 2.5arcsec from each other in the telescope plane (one in the center and the other four along the X and Y axes at 2.5arcsec from the first one). The wavelengths considered is the same and, as it is clear, the horizontal spread is more prominent.

In § 3.1.2 some changes to the optical design, performed after the first run at NTT, will be presented. For ease of comparison, the spot diagram for a 5arcsec extended source is added to this section and presented in Figure 15 (the source is the same used to obtain the spot diagram in Figure 14).Figure 14 It is clear how the aberration wings are greatly reduced by the new optical train. For further details on the changes carried out to the optical design, see §3.1.

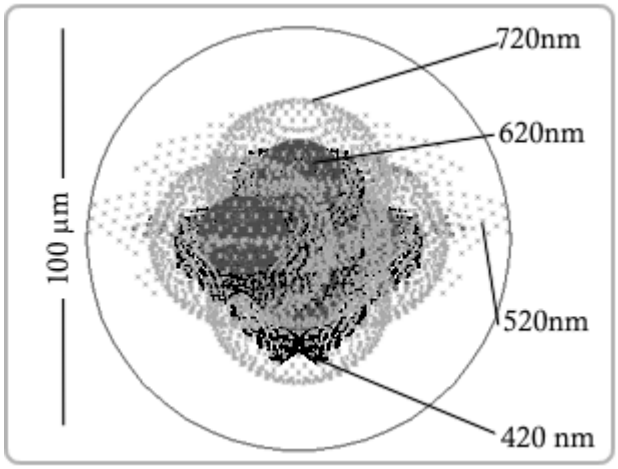

Figure 13: Spot diagram on SPAD focal plane of 5 polychromatic point sources: one point is on-axis, the other four are at 1 arcsec distance along the vertical and horizontal directions in figure to simulate the case of a 2 arcsec diameter source. The different wavelengths of the simulated beams are indicated by the arrows and are expressed in nm. The circle indicates the perimeter of the SPAD sensitive surface. N.B: This image is referred to the optical configuration with the changes implemented after the first run at NTT.

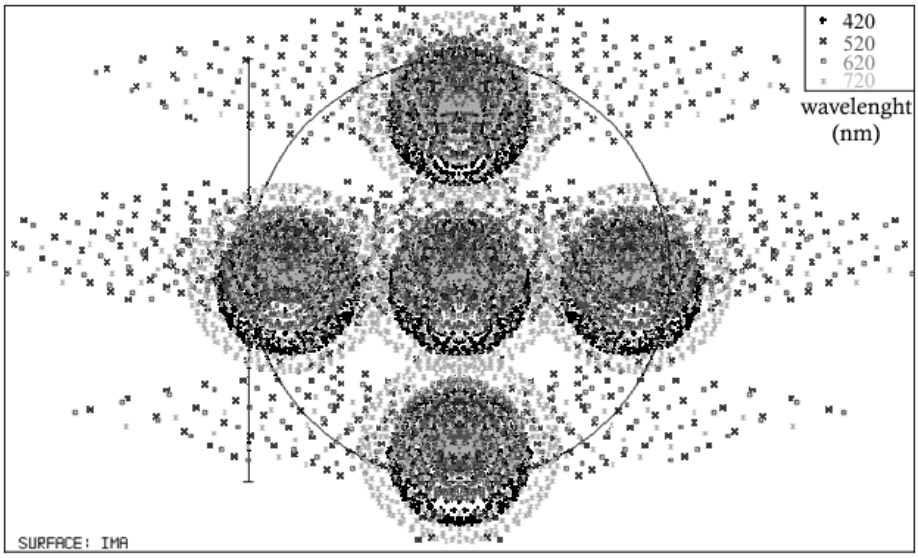

Figure 14: Spot diagram on SPAD focal plane of 5 polychromatic point sources. The distance between the source points on the telescope plane corresponds to 2.5arcsec, so the ray tracing shows the spot diagram for a 5arcsec diameter source. The different wavelengths of the simulated beams are indicated in the label. The circle indicates the perimeter of the SPAD sensitive surface (100 μm diameter).

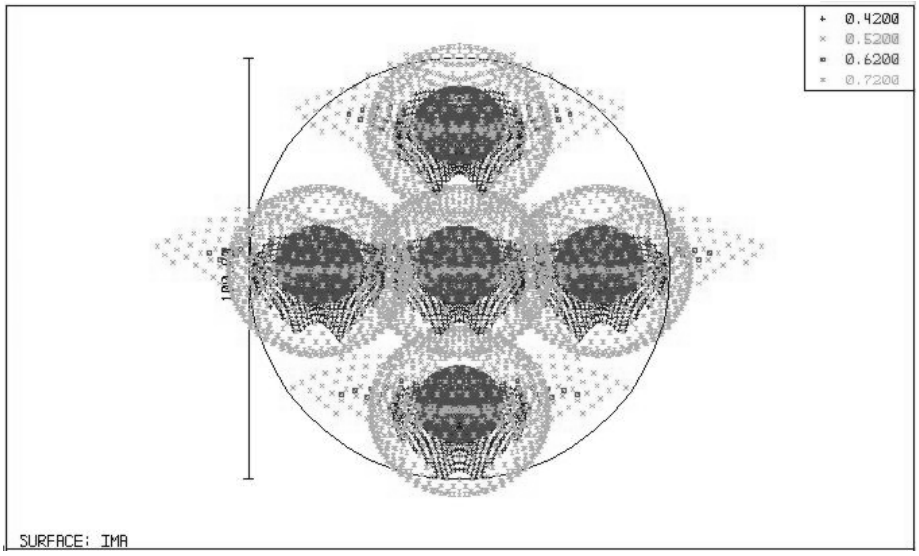

Figure 15: Spot diagram on SPAD focal plane for a source as in Figure 14.The aberrations are clearly reduced. The case considered is the improved version of IQuEYE with some optical elements changed (see 3.1.2). Label indicates the wavelengths in microns.

The optical performance is simulated considering the fraction of rays that reach a circular area in the image plane (the focal plane of the instrument, i.e. the surface of the SPAD detector) in function of the circle radius (the so-called encircled or enclosed energy function). Figure 16 shows the plot of the encircled energy on the 100 μm diameter SPAD for two polychromatic and uniformly illuminated sources, one having a diameter of 2arcsec and the other of 5arcsec. The second case is worse than expected in normal conditions, where the seeing define an approximate Gaussian distribution. However with the 5arcsec source the theoretical

energy encircled in the SPAD sensitive area is still about 94% of the total flux. Obviously here is not considered telescope vibrations and pointing misalignments. Values near 1 for the encircled energy (the 100% of rays or photons collected) are not reached even for a point-like source (the flatness of the curve related to the 2arcsec source near the limb of the SPAD could suggest this in Figure 16); the PSF has two horizontal tails that exit the detector, leading the value of the encircled energy just above 97%. Some improvements implemented after the first run at NTT brought this value above the 99%, as will be explained in § 3.1.2.

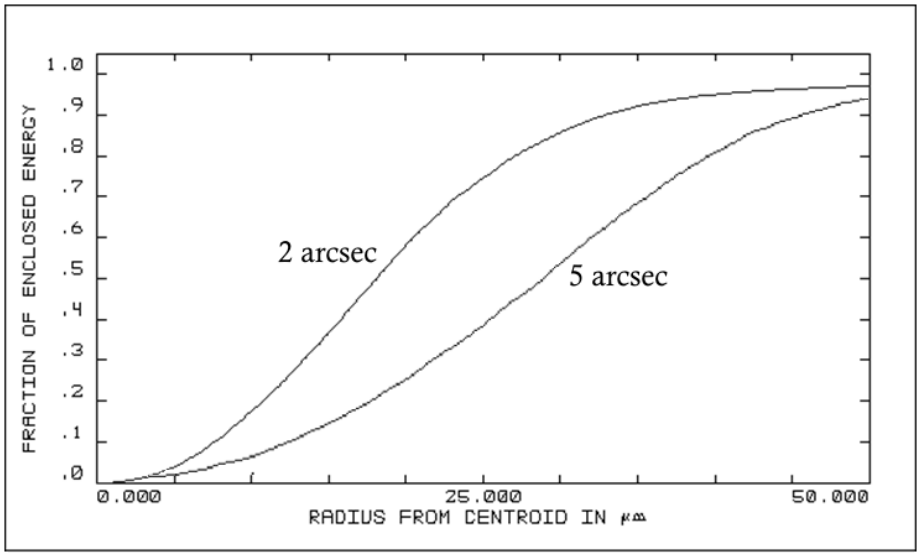

Figure 16: Encircled energy function in the focal plane of IQuEYE. Two polychromatic sources having 5 and 2arcsec diameter are considered. The wavelength ranges from 420nm to 720nm.

1.2.2 Tilt and Defocusing

The analysis performed in the previous subsection gives indications about the optical system for a source on axis and perfectly aligned and centered. The link to the telescope interface is done through an aluminum truncated cone attached to the flange of the derotator. This configuration can lead to tilt errors guaranteed to be in the range of 3" for a load of 800N at 400mm from the flanges face (from ESO documentation). To these must be added any twisting of the instrument (see § 1.3.2). Considering all the possible deformation, however the tilt obtained is less than 1'. A ray tracing performed in order to analyze the tilt effect does not bring differences with the in-axis situation for 1'. For values of tilt severely overestimated, the situation remains almost unchanged. The increases in aberration begin to have noticeable values only for major fractions of a degree.

More problematic are the defocusing. In addition to the normal spread of the area covered by the image out of focus, the presence of the pyramid involves a shift of the beam along the Y-axis of the detector. Figure 17 shows some shifts relative to a single point-like source in which the focus are translated along the Z-axis (the optical axis) between -100 and

+100μm. In addition to the spread, the focus translation along Y-axis is of the order of the translation along the Z-axis. Considering in this case all possible flections of the instrument when overhanging attached at the telescope and taking in account the thermal deformations, analyzed in the next sections, the ray tracing produced a critical situation. In fact, if the target is out-of focus, a simple focusing procedure can recover the right position, but this is not possible for difference of focus between the four SPADs. The simulation suggests that each SPAD must be aligned along the Z-axis with a position relative to the other three with a precision of ±3microns.

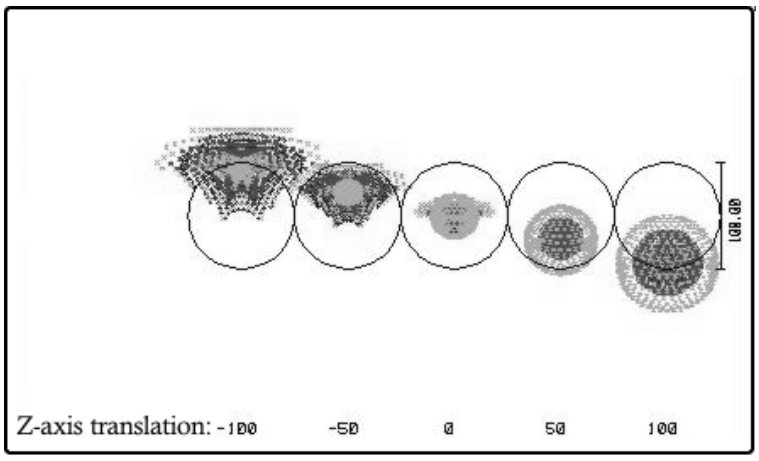

Figure 17: spot diagram in case of defocusing. The black circle indicates the size of the detector. All measures are in microns.

For this reason the alignment procedure results very and critical and the configuration reached during the instrument integration phase, in laboratory, must be absolutely stable and have to avoid even the smallest shifts and misalignments along the optical axis.

Moreover we have to take in account that IQuEYE has no own focusing mechanism and the focus is obtained by moving the NTT secondary mirror. Since the SPADs are one-pixel detectors, the pointing procedure and the focusing of the instrument, as we will see, are performed through the field camera. That means the focus on the SPAD is not obtained directly but only matching with the camera one. Therefore the camera has to be perfectly focused on the same focal plane on which the SPADs are.

1.3 Mechanical design

1.3.1 Solutions

Figure 18 shows a 3D view of the mechanical structure of IQuEYE after the changes performed in 2009. On the right side the instrument has a flange for the connection with the telescope interface, where the light beam enters and proceeds as described above. For the mechanical structure various solutions were taken into account and analyzed, among them, that which is stated here (and chosen) is the one that provides the best performances. The structure is conceived to be developed in two sep-

arate blocks, one is the bench connected to the flange, having trapezoidal cross-section, which supports all the optical elements of the focal reducer. In this block the eight boards for remote controlling of all the micrometric engines (for the filters wheels and the pinhole slide) are housed as the field camera and the sky-SPAD. The second block, the "Octagon", contains the optical elements downstream of the pinhole, to the SPAD. In Figure the blocks containing the optics are not shown and are only some of their supports are visible.

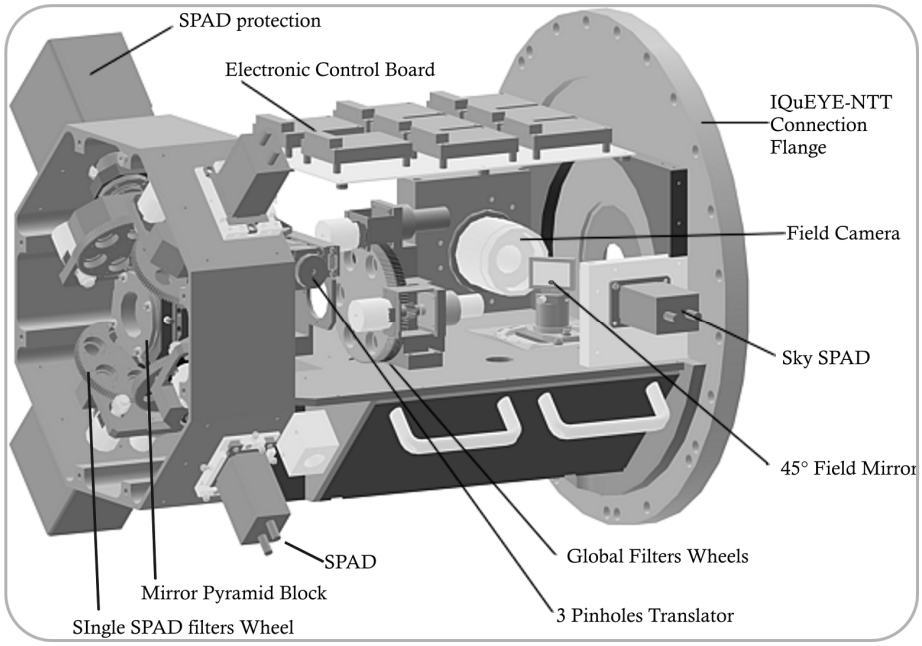

Figure 18: 3D view of the IQuEYE optomechanical bench. This image is referred to the version improved after the telescope run.

The original concept included a second centering device, which, through a mobile arm terminating in a prismatic mirror and positionable between the pinhole and the octagon, diverted the beam and then refocus it onto a CCD in order to control the centering of the target. Unfortunately, the optimal optical configuration leaves little space between the focal plane on which lies the pinhole and the pyramid, so the implementation of this device would make extremely complicated the mechanical design.

As we have seen, the most critical part is the final alignment of the four SPADs. The solution found is a flange allowing the micro-movements along the X-Y plane of the detector (perpendicular to the optical axis) which can slides on a second flange fixed to the octagon and providing the micro-movements along the optical axis. A total of ten high-precision micrometer screws for each SPAD allowed us to achieve submicron precision in the alignment phase.

The final design of the optomechanical support was performed by the Tommelleri srl company (Verona, Italy). All the mechanical parts are realized in 6061 T6 aluminum. The ultimate choice of the support structure is instead performed in collaboration with the Mechanical Engineering Department of Padua University which also performed a gravitational

and thermal deformation analysis for the structure. The detail of this analysis could be found in [PAR]. Five preliminary versions of design were drawn for each of the hypothesized configurations and were evaluated with specific simulations in order to determine how the relative positions of the optical elements change.

1.3.2 Gravity and Temperature deformations

The optical design was carried out considering a rigid structure. After defining the maximum optical tolerances, the actual elasticity of the materials has to be taken into account, in order to develop a real-world structure that satisfies these requirements. As previously described, IQuEYE is overhanging connected through a conical flange to the NTT derotator. The weight of the instrument causes bending of the structure and a displacement of all the objects it supports. For these reasons, it is necessary to verify that the instrument is sufficiently rigid to prevent excessive flections and relative misalignments of optics and detectors. For this purpose we have performed a FEM (finite element method) analysis with the software ANSYS and ANSYS Workbench. For the investigation of each version of the instrument we used different models because the whole system has many interfaces which can be modeled in different ways, in total, the finite element simulation was carried out through 147453 items for a total of 305739 nodes.

The results lead to the structure shown in Figure 18.

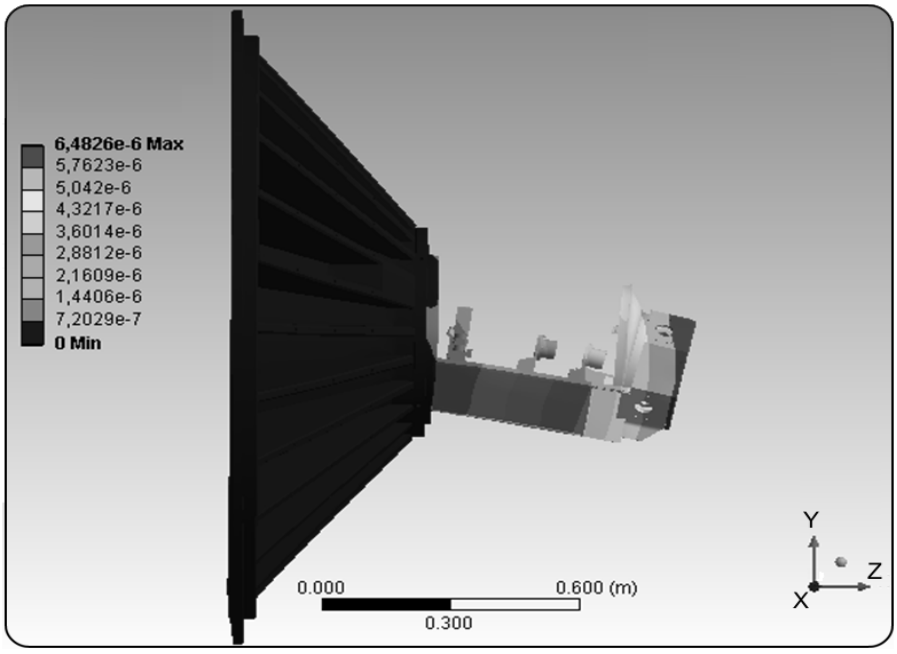

Figure 19: Flections of IQuEYE due to the gravity**.** The point considered as reference is the focus of NTT.

In Figure 19 a result of ANSYS analysis is depicted. The reference point on which the amount of deformation is indicated is the telescope focus (placed near the right edge of the conical flange); in particular, the struc-

ture adopted is subject to deformations that, in total, do not exceed 6.5µm along the whole instrument. The pinhole centering can be displaced, in the worst case, of 3µm along the axes perpendicular to the optical one (X and Y in figure) and of a negligible quantity along the optical axis, ensuring compliance with the requirements.

During the observations the derotator of NTT rotates around the optical axis and the structure change its positions, this situation was simulated and some of the results are shown in Figure 20, where the position of a SPAD (the one we have called channel B) in function of the rotation along the Z axis is depicted.

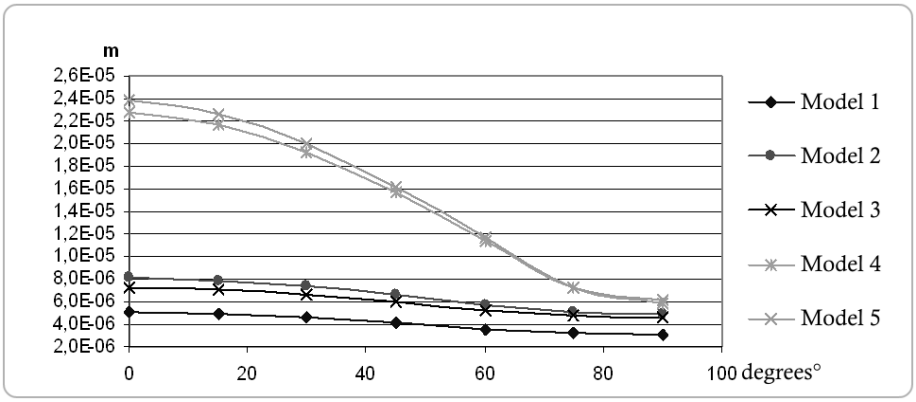

Figure 20: SPAD displacement due to the rotation of the derotator between 0 and 90 degrees.

The model chosen is the number 1 and gives displacements between 5 and 6µm distributed mostly along the axis parallel to the detector surfaces.

The presence of thermal gradients due to the power dissipated by electronic devices used in IQuEYE leads to the expansion of the structure, causing further deformations. We performed a thermal analysis and, starting from the temperature distribution calculated, we performed the corresponding deformation analysis. In this case the effects of temperature gradient can produce displacements greater than those determined by the gravitational force. (see Figure 21).

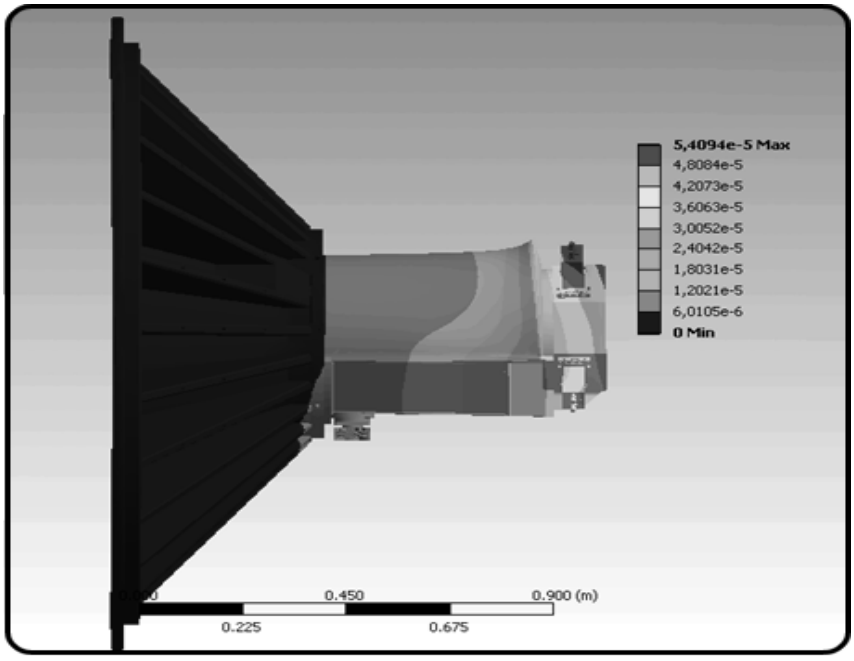

Figure 21 Analysis of the deformations induced by thermal gradients caused by the electronic devices.

It is also carried out a stress test on the optical components considering the temperature variations of which the instrument may be subject during shipment and the results show that the stress, even in the most extreme cases, are very much lower than the limit of glass compressive strength.

With those analyses it may be concluded that the flexions in the mechanic structure caused by the gravity are modest and below the limit established in the optical design, while the effects of thermal expansion may be more problematic for the stability of optics and detectors in particular conditions. Actually all the simulations were performed considering the maximum dissipation power for each device and are, therefore, overestimated. In normal working conditions it is reasonable to assume that the instrument performances are not affected by effects due to deformation of the mechanical structure.

1.4 Electronics

So far we have seen the part of IQuEYE related to the detection of photons. This section is devoted to the description of the IQuEYE Data Acquisition System (IDAS), which is the system designed to time tag the signals from the SPADs. We published a detailed description in [IQ1].

The system requirements are:

- a time tag capability with an absolute UTC referenced accuracy of the order of 500ps (RMS) for each detected photons.
- a relative time tagging resolution of the order of 100 ps (RMS)

- the capability of sustain hours of continuous operation for count rates ranging from few tens of Hz up to 8 MHz.

1.4.1 Time to Digital Converter

The first element to take into account is, again, the detector. Each SPAD produce, after a photon detection, a pulse. The SPAD electronic provides two kind of standard as output: a TTL signal which can sustain count rates up to 12 MHz in linear regime but has a ~250ps jitter and a NIM signal (Nuclear Instrumentation Module standard) which, for maintaining the linearity, is limited to run below a count rate of about 2 MHz, but has a much more accurate jitter of ~35ps.

Our choice is the NIM signal, while the TTL signal was sporadically used in parallel with the NIM one for check operations and not much more. For this kind of applications it is important to consider all possible sources of time delays, in fact even a rough estimate suggests that few centimeters of difference between two cables can induce an error larger than the resolution request. So NIM signals exiting the SPADs are brought by means of calibrated equal electrical length coaxial cables to a TDC board (time to digital converter). This board is the CAEN V1290N, developed for high energy physics applications at CERN and working with an internal clock at 40GHz.

So the TDC board is nominally able to time-tag the NIM voltage pulses with a time resolution of ~25ps obtained through an internal 40MHz oscillator with a DLL (delay locked loop) and PLL (phase locked loop) frequency multiplier by 1024. The quality of the internal oscillator is conceived for nuclear physics experiment so the clock is a quartz oscillator capable to sustain a high precision for short time, not good enough for our purposes. In fact the requirements are more stringent: our applications need to obtain simultaneously both the short-term stability, typical of a quartz oscillator, and the long-term one assured by a primary time reference.

The CAEN timing board could be fed by an external clock by means of which it can achieve higher performances.

Figure 22 shows a blocks schematic of the electronic acquisition, control and storage.

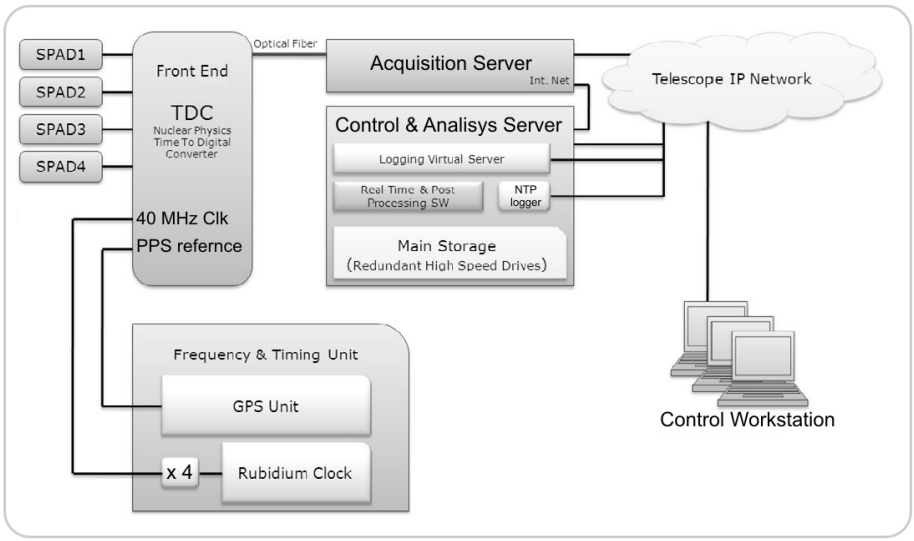

Figure 22: conceptual scheme of the acquisition electronics. (See text for details).

1.4.2 Timing System

Obviously the best solution in terms of stability and performances, in order to substitute the quartz oscillator, would be a hydrogen maser clock, but the available budget does not allow this kind of choice. For this reason we implemented a more sophisticated timing system, the IQuEYE time and frequency unit (ITFU), a trade-off in terms of precision and stability over long acquisitions. Basically the CAEN board is fed by a Rubidium oscillator subject to a post-processing correction for the long term drift based on the GPS signal.

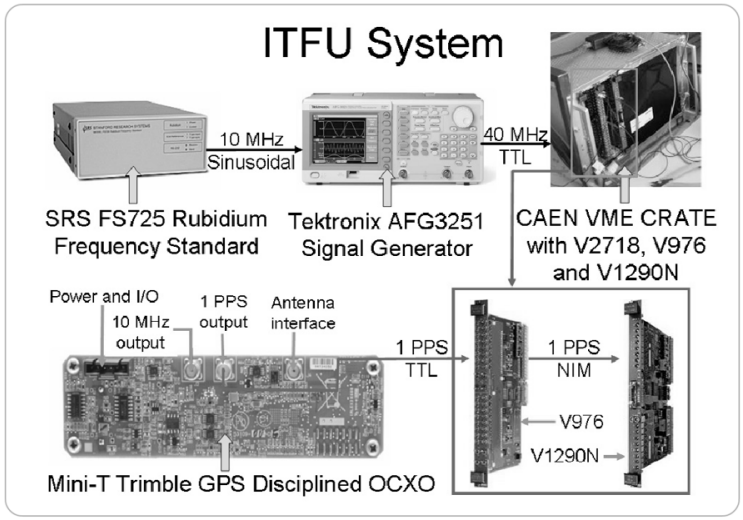

Figure 23:IQuEYE Time and Frequency Unit. Atomic clock signal multiplied by four fed the CAEN board. A GPS PPS signal is supplied to the board for a long-term drift correction.

As noticeable in Figure 22 and Figure 23, the primary clock is a Stanford Research System FS275 rubidium oscillator not disciplined by an external reference (because this worsens the phase noise). It produces a 10

MHz sinusoidal signal that is converted to a 40 MHz TTL signal through a frequency multiplication by a Tektronics AFG3251 pulse generator.

The clock was tested at the Laboratory of Time & Frequency of the Cagliari Astronomical Observatory (OAC) using a primary standard cesium clock as reference; it is subject to a linear drift of approximately 65ns in one hour. After the subtraction of this drift, only a residual stochastic phase error remains, with a RMS value shorter than 50ps for acquisition of about 1000 s, as shown in Figure 24.

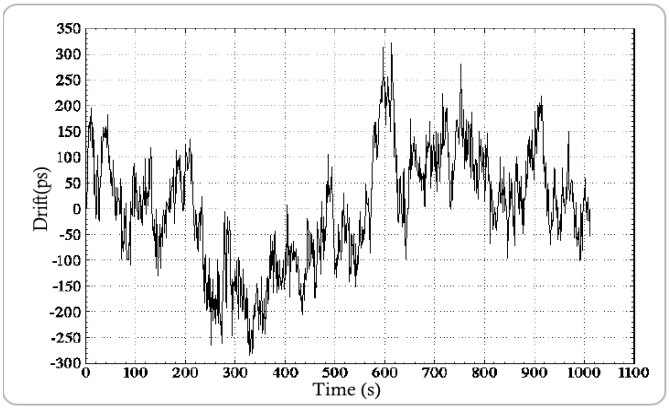

Figure 24: rubidium oscillator pulse per second (PPS) versus the Astronomical Observatory of Cagliari cesium oscillator over 1000s. The graph shows the residuals after removal of the linear phase drift.

The TDC CAEN board also collect a pulse per second (PPS) signal provided by a mini-T Trimble GPS receiver through a TTL\NIM converter. The PPS is acquired in a sixth channel as signal input and the time of arrivals (ToAs) are tagged and stored with the SPADs data. Since every pulse has low precision but the GPS PPS has long-term stability, a post processing algorithm consider the GPS pulses received over the whole acquisition and estimates and removes the rubidium oscillator long-term phase drift. The GPS signal is also used to determine the start time and the UTC-corrected time tags: the start signal is provided by the control PC whose system clock is disciplined by the Network Time Protocol (typical uncertainty of few ms). The software identifies the time origin with the first GPS pulse detected after the start signal. In this way the initial times have a RMS uncertainty of ~25 ns (typically value for good quality single frequency GPS receiver). But looking at the string of PPS, an interpolation reduces the error associated with the starting time in a way proportional to the number of acquired PPS. For example, after one hour of observation the uncertainty on the initial time is decreased to 0.4 ns RMS.

The RMS time errors associated to the SPADs jitter are approximately 35ps, the electronics chain leads to possible errors around 50 ps, the rubidium clock residual phase error has an RMS value around 50 ps and the internal sampling discretization of the TDC board is ~25ps. So a total relative RMS time error lower than 100ps is derived.

Considering this relative error and what was said for the UTC time tagging, an absolute RMS time accuracy, with respect to UTC, shorter than 500ps for one hour of observation is obtained.

1.4.3 Rollover

The data from the TDC is digitalized at 25ps (24.4 to be precise). The times of arrival are stored in a buffer using 5bits for the channel number that individuate in which SPAD the detection is done and 21bits for the time tag. This means that after $2^{21} \cdot 25ps \approx 52\mu s$ the counter is reset and the counting re-starts from zero, so the time tags coming from the TDC are actually number digitalized at 25ps spanned in the range [0÷52ms]. That implies the non-uniqueness of each tag. We called rollover each reset of these 52µs period. If the signal detected is quite intense the SPADs detect some photons between each rollover and the time of each event can be reconstruct simply by counting the number of rollover elapsed from the start time, which is marked by a stop in the ascending order of the ToAs. But if the signal is faint, there may be a situation in which no photon is detected between two rollovers, so a loss of 52µs affect the arrival times after that empty interval. An example is given in Figure 25 where in the x axis the "real" time is given and y axis indicates the time tags assigned to each detection by the TDC. The events A and B in figure are separated by a time interval larger than 52µs and, between them, two rollovers occur. But there are no other events between them indicating the presence of two rollovers instead of one.

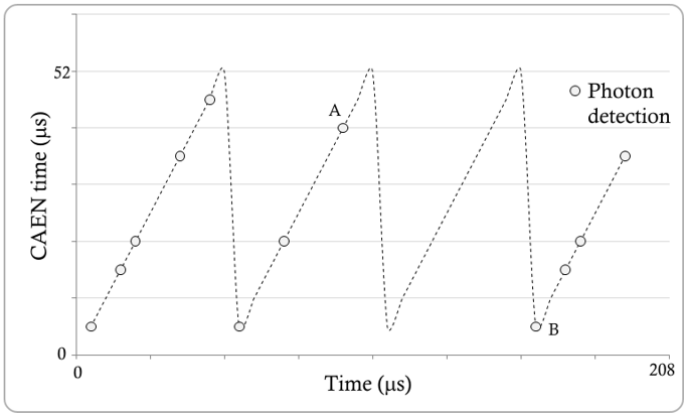

Figure 25:range of time tags assigned by the CAEN TDC board to the detected events. Every 52µs the counter is reset.

For this reason one of the 16 input TDC board channels is fed with an external 20 kHz reference pulse, time-tagged as signal, this operation allows us to determine the correct value of rollovers elapsed because the reference pulse produces at least an event between every rollover. Each (true) ToA stored is than corrected in post processing and the exact number of rollovers is added.

1.5 Control and Acquisition software

One of the most important characteristics of IQuEYE is the ability to store all the raw time-tags of the detected photons. In this way corrections, various temporal binning, correlations between different channels and any other operation on the original data can be performed in post-processing. This implies a large amount of data to store: from the CAEN board the data are passed to a dedicated acquisition server (Acquisizione) through a bridge and an optical fiber that can support a data exchange rate of ~60 Mb/s. This is the bottleneck limiting the maximum count rate of IQuEYE.

A second server (Controllo) is devoted to the acquisition and the data storage and is controlled through a user interface developed in Java. The interface allows the control of each instrument subsystem: the selectable pinholes slide, the filters wheels and the field camera. Moreover it provides real-time analysis of the acquiring data. By means of this software the field images incoming from the CCD camera can be stored and used to analyze in post processing the guiding errors and sky/reference stars fluctuations. Figure 26 shows a screenshot of the software running.

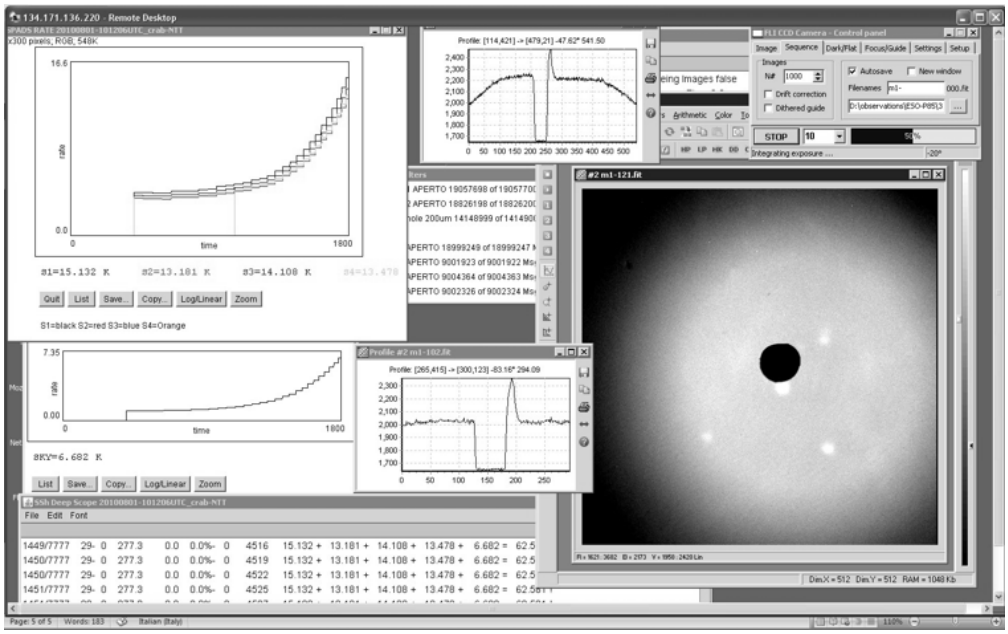

Figure 26: screenshot of the acquisition program running. On the left (top) the signal detected by the four SPADs and, behind, the sky-SPAD signal and the numerical flux detected for each channel. On the right one can see an image of the field (the hole in which the target is put is clearly visible) and some basic controls of the camera (cooling temperature, exposure time etc.).

The storage capability in the first version of IQuEYE was approximately 2 TB: all the data were recorded in a 6 SATA disks raid6 configuration. All the electronics equipment is mounted into a standard rack placed in the NTT Nasmyth focus room.

2 IQuEYE Integration

The two phases of integration, calibration and testing of IQuEYE (one in 2008 and one to implements the improvements conceived following the first observation run, in 2009) were performed in an ISO 6 (with ISO 5 areas) fully equipped clean room at the Department of Information Engineering of the Padua University.

Although not very informative from a scientific perspective, the integration phases of the instrument represent a large period in the evolution of this thesis. The alignment procedure is not described here and this chapter is intended to give a description of the IQuEYE main optical and mechanical components, with their alignment tolerances, required to fulfill the optical performance expected.

2.1 Quality of optical components

2.1.1 Lenses

All optical components were analyzed to verify the correspondence with the theoretical performances. The performance of each lens, of each adjacent pairs of lenses and of the optical trains composing the focal reducer and the four arms were simulated by ZEMAX interferogram and than the experimental setup was reproduced in clean room. Every optical train was tested after installation too, in order to identify possible deformations induced by mechanic holders. The experimental setup is depicted in Figure 27: the primary beam comes from the interferometer on left hand (indicated in figure with "Zygo") and passes through the target lenses, in this way it converges in the center of a spherical reference mirror. The mirror is tested and calibrated, it is free from aberrations and the surface has an optical quality superior to the resolution of the interferometer ($\lambda/20$)*, so does not produce detectable wavefront deformation. After reflection, the beam passes through the target again. There it is re-collimated and comes back to the interferometer where the interference with the reference plane waves allows the analysis of the wavefront deformation.

* With λ the wavelength of laser used by the interferometer is indicated, that is 632.8nm.

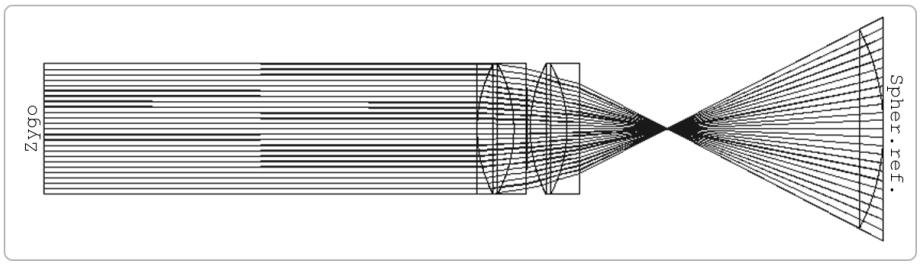

Figure 27: experimental setup for the analysis of lenses optical quality. The interferometer (He-Ne laser source) is on the left. Lenses at the center are the target under investigation and the mirror on the right reflects the laser beam back to the interferometer.

The outgoing wave surface is then analyzed with the interferometer software and compared with the theoretical results obtained by the ZEMAX models. An example of the analysis performed is shown in Figure 28, while Figure 29 compares the simulated interferogram with the real one.

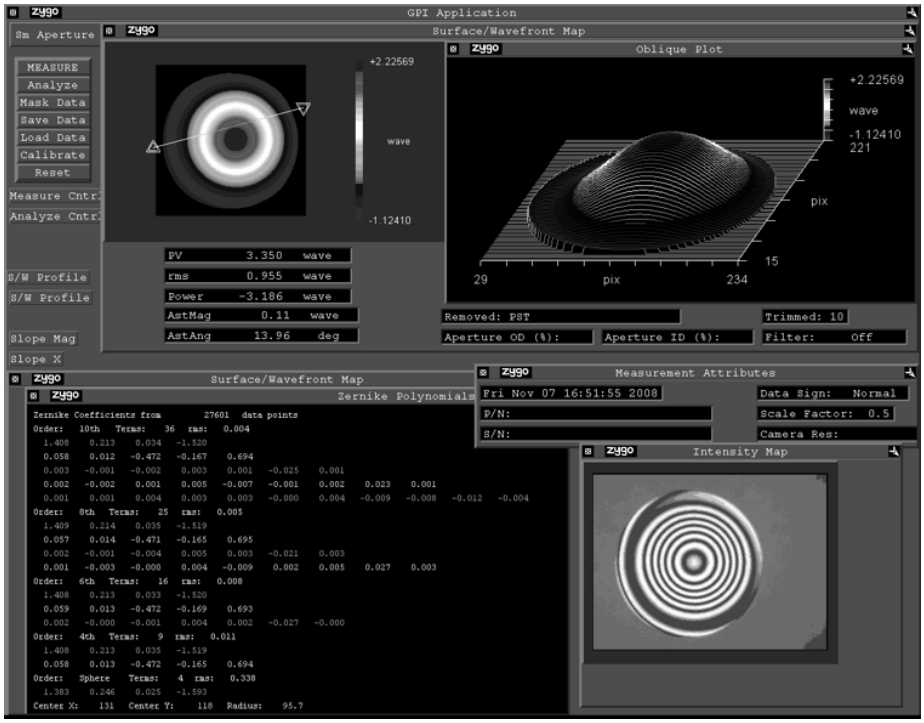

Figure 28: Interferogram for a single lens. The wave surface after a double passage through the lens (as in configuration depicted in Figure 27) is analyzed. On the right the shape of the wafefront is reproduced above the interference pattern. On the left the interferometer software returns the Zernike polynomial expansion describing the wavefront.

The analysis results confirm the expected performances for all optical elements and indicate that the lenses-holder and the attachment steps do not introduce significant strains on the lenses glass.

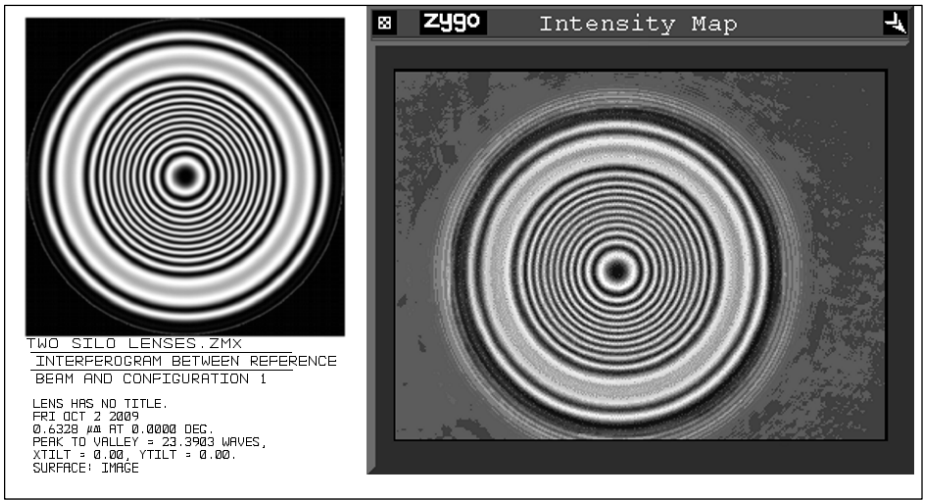

Figure 29: direct comparison between the interferogram obtained with the Zemax simulation (left) and real one (right) of the first two lenses in the focal reducer. The peripheral zone of the interferogram not matching the theoretical case corresponds to a peripheral zone of the lens that will be covered by mechanical holder.

The interferometric analysis was performed also for reflective surfaces.

2.1.2 Pyramid

The mirror pyramid reflects the part of the light directed to the detectors, which is the "true" signal to be collected. For this reason the roughness level required to the manufacturer (Gestione SILO s.r.l. - Scandicci, Italy) was a mirror surface quality at least λ/10 (RMS). Each face of the pyramid was analyzed finding that the request is abundantly satisfied and the quality of λ/10 is nearly reached even for the peak-to-valley values. In Figure 30 the surface map of one of the mirror face is shown.

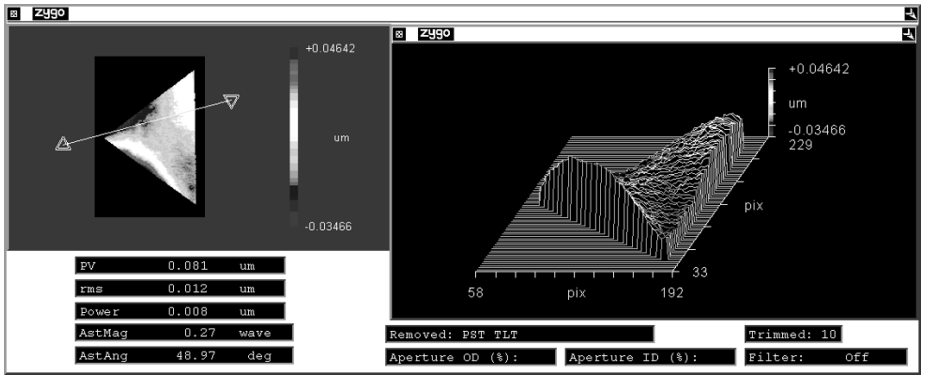

Figure 30: analysis of surface quality for one of the pyramid faces.

2.1.3 Field monitor

The field monitor system (see Figure 11) is composed by a holed mirror that reflects the images surrounding the target (centered in the hole) towards a field camera. The camera is a Finger Lakes Instrumentation MaxCam CM9 (see [*fli*] for details) with a KAF0261E CCD, 512 × 512 20µm pixels cooled till -30°C (the sensor data sheet can be found in [*kod*]). The focusing system is a simple commercial photographic objec-

tive (Nikon 60mm). The focus is locked and the objective is aligned so that the CCD plane represents a plane conjugate to the detectors focal planes. In this way the focusing operations through NTT secondary mirror is performed using targets in the field camera.

The field monitor system does not allow the availability of filters: it can be a problem for the pointing operation of very bright targets, over the saturation limit of the CCD.

The surface roughness of the mirror was analyzed as depicted in Figure 31 and the quality is better than $\lambda/10$ (RMS).

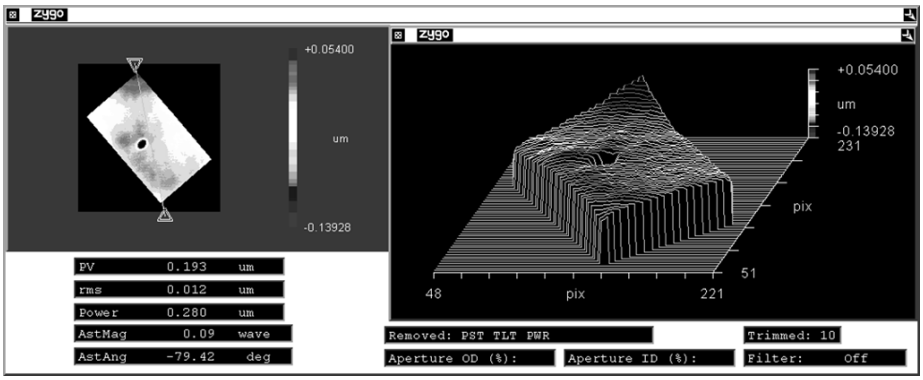

Figure 31: surface quality interferometric analysis for holed mirror**.**

2.1.4 Movement and repeatability of positioning

Each mobile mechanical part has been tested for positioning repeatability.

Filters wheels do not require particular precision: the wheels have a margin of error in the positioning of more than a millimeter before the edge of the optical beam is intercept. Test has shown that margin is widely respected.

The sole really critical element is the pinholes slide; in fact the diameters of the pinholes range between 200 and 500µm. An incorrect displacement in the intermediate focal plane may cut off a part of the image and, so, a reduction of the flux in the four SPADs is caused.

In order to analyze the positioning precision of the motorized OWIS linear stage we used a microscope aligned with a light source and fixed to the IQuEYE optical bench. In addition to the ordinary translations among the three available pinholes, we ran the stage through thermal and mechanical stress. The clean room temperature was varied between 20 and 10 degrees and the slide has been subjected to vibrations. The re-positioning precision is under the threshold of 5µm in the shift direction and negligible for the other directions.

In Figure 32 an image taken with the re-positioning checking microscope is shown. The white dot in the center of the 300µm pinhole is the focused image of the laser source used for the alignment activities that will be described below.

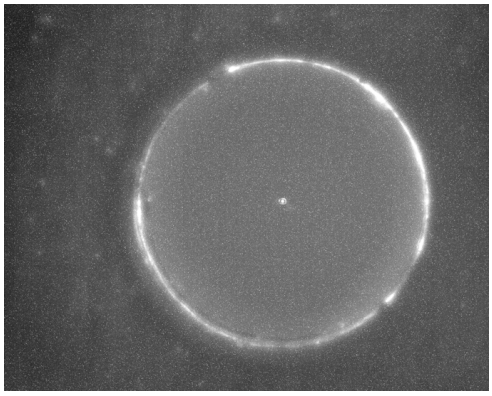

Figure 32: 300μm pin-hole. The source focused on its center is visible. Also the reflecting edge of the metal plate can be seen (see § 3.2.1 for an analysis of problems related to this).

The reflecting edge of the metal plate is clearly visible; it caused a slight contribution of reflected light during the first run at NTT, as will be shown in 3.2.1.

2.1.5 Filters and filter wheels

This subsection is only devoted to list the filters available for the observations. As seen in § 1.2, there are two filters wheels acting on the beam before it is split by the pyramid. Those filers are in common for the four SPADs and they are listed in Table 3. First and fourth columns indicate the kind of filter mounted on the wheel one (W1) and two (W2), for each filter the central transmitting wavelength is indicated in second and fifth columns (Peak) and, for the polarizers, the peak extinction ratio is listed. Third and sixth columns indicate (where possible) the full width at half maximum of the spectral transmission curve.

Table 3: Main characteristics of the filters/polarizers available on the two IQuEYE filter wheels. P.e.r. indicates the peak extinction ratio of the polarizer.

W1	Peak (nm)	FWHM (nm)	W2	Peak (nm)	FWHM (nm)
B	433	101	Neutral 1	-	-
V	531	82	Neutral 3	-	-
R	747	234	He II	468	2
IR	817	179	O I	630	2
OIII	501	1.3	Pol.Vis.	p.e.r>1:10^3	-
Ha	656	3	Pol.U.V.	p.e.r.>1:10^5	-
stop	-	-	Neutral 2	-	-
	-	-	-	-	-

Each of the four SPADs channels has a single-arm wheel. At present only two filters per channel are available.

The central wavelengths for the single-arm filters are:

394 and 410nm for SPAD A; 467 and 515nm for SPAD B; 546 and 580nm for SPAD C; and 610 and 694 nm for SPAD D. All these filters have a FWHM of 10nm.

2.2 Alignment procedure

The alignment procedure was performed using the collimated beam (diameter about 10cm) coming from the interferometer. To simulate the focus of the telescope an appropriate lens (L hereafter) was placed in front of IQuEYE in a 3D micrometric translator that allows micrometric movements along the three axes remaining within the collimated beam. The tilt of every main surface (the connecting flange to the telescope, the bottom of the octagon and the sides where the SPADs are attached) was verified with interferometric techniques using of a reference flat mirror. For the correct positioning of the lenses we used a beam analyzer, but the procedure followed will not be discussed here.

Once aligned all the optical trains for focusing the image on the detector, the three pinholes by using a microscope and after checking the quality of foci obtained, we proceeded with the alignment of the SPADs, using the intensity measured by themselves. The first step was to move the SPADs looking for the maximization of their counts. Because even after the passage through the optical trains the quality of the interferometer spot is high (diameter <10 microns) the maximization is not sufficient to ensure the good centering of the detector. Acting on the lens L we mapped with micro steps a circular region in the XY plane (perpendicular to the optical axis Z) simulating the extension of the source. A SPAD perfectly aligned gives a detected intensity profile extremely smooth, a vast region wide about 100μm in which the counts are stable between two steep drops to zero intensity. The steepness of the curve is actually dictated by the size of the laser spot that, however, is much smaller than the sensitive area of the detector. If the image is out of focus (i.e. the SPAD is not correctly positioned along the Z axis) the slope becomes sweeter and the central stability region more narrow. An example is provided in the first graph of Figure 33 in which a scan obtained by moving the focus of the telescope (the lens L) along the X axis produces a region of stabil-

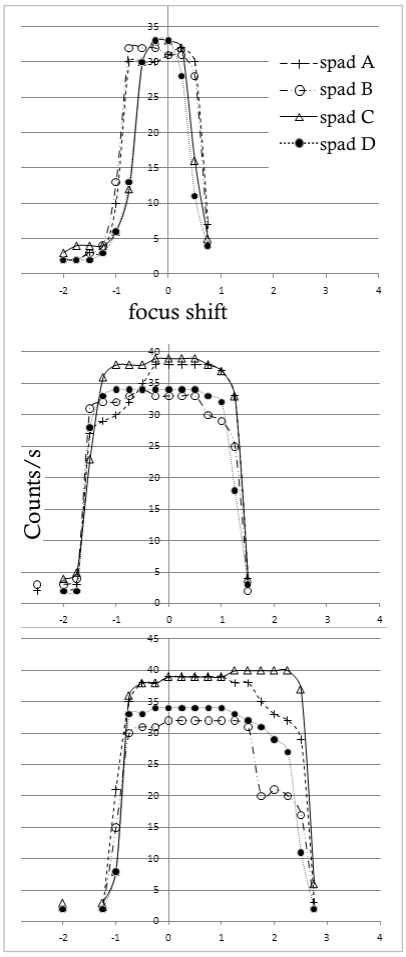

Figure 33:SPAD signal during three steps of the alignment phase. The X-axis units are arbitrary, the Y-axis units are expressed in 10^5 counts per second.

ity too narrow for all four SPADs. (Units along the X axis of the graph are arbitrary units of the micrometric translator). The second graph shows an improvement in the focus of all four SPADs and probably an off-center of the SPAD A along the Y axis. In the third graph the focus conditions are improved, but the centering is worse, except for the SPAD C. The same procedure was repeated for the Y axis and then again for the X one and so on, in order to obtain a grid of intensity sampling describing the detectors position.

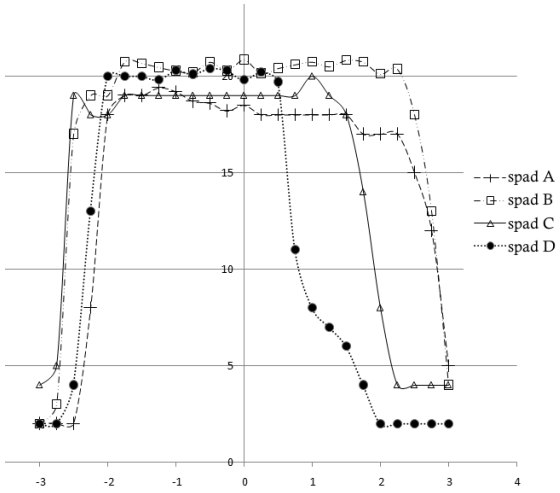

Figure 34: Intensity scan along the instrument Y axis. The SPADs are not yet well aligned. (the units in abscissa are arbitrary subdivisions of the micrometric translator, the ordinate axis shows values expressed in units of 10^5 counts/s).

Figure 34 is an intensity scan as above, but along the Y axis. Only the SPAD B is near the optimal alignment. Actually it was performed in a different period and with other filters used to attenuate the laser intensity. The maximum count rate, indeed, reaches the value of 2MHz (the ordinate axis unit are 10^5 counts/s). Finally in Figure 35 all the SPADs are near to the optimal alignment (along the Y axis!).

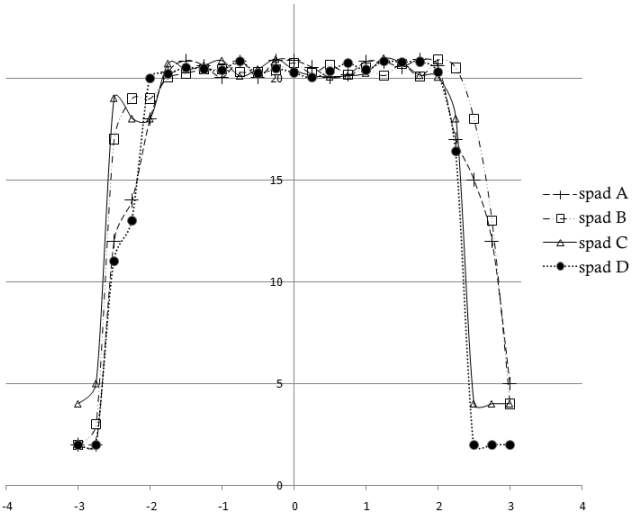

Figure 35: Intensity scan along the instrument Y axis. The SPADs are near the optimal alignment.

The complete intensity scan for each SPAD appears as in Figure 36: an X-Y grid of samples for the intensity detected by the SPADs. A detector is perfectly aligned when this grid describes correctly the shape of the SPAD sensitive area[†].

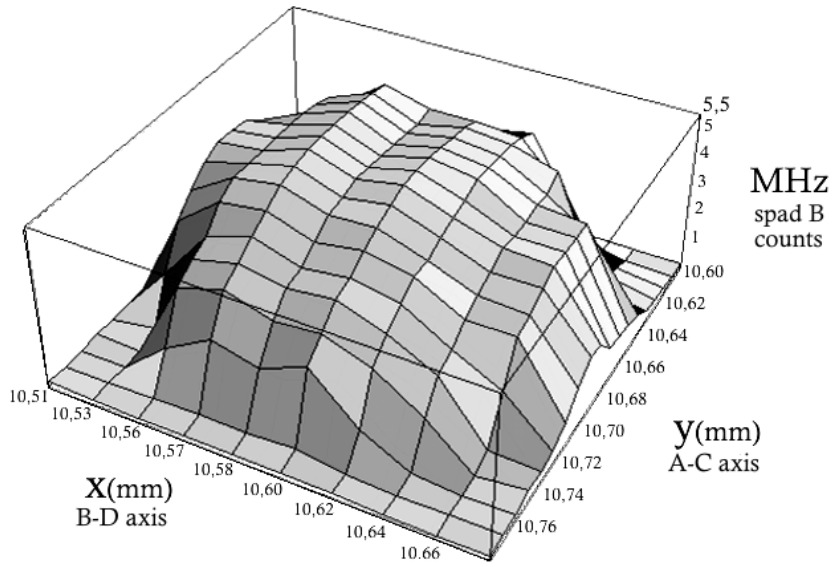

Figure 36: X-Y intensity scan performed by moving the image perpendicularly to the optical axis.

Considering the pitch of the micrometric screws used for the SPADs positioning, the aligning tolerances are of few microns for X and Y axis and of one micron for Z axis, in line with the requirements.

2.3 Performance

This section shows the total efficiency calculations performed for IQuEYE. It is obtained by multiplying the efficiencies of the single elements involved: telescope and pyramid reflectivity, lenses transmittance, SPAD quantum efficiency. For the accurate estimation of the last, the characterization of the detectors was performed at COLD laboratory of INAF Osservatorio Astrofisico di Catania. The measurement procedure will be not explained here, so the reader is referred to [BIL] for the details. The graph in Figure 37: shows the quantum efficiency of a SPAD as measured at COLD laboratory in function of wavelength.

[†] truly, saying it in strict terms, the convolution between the characteristic function of the detector sensitive area and the PSF of the source.

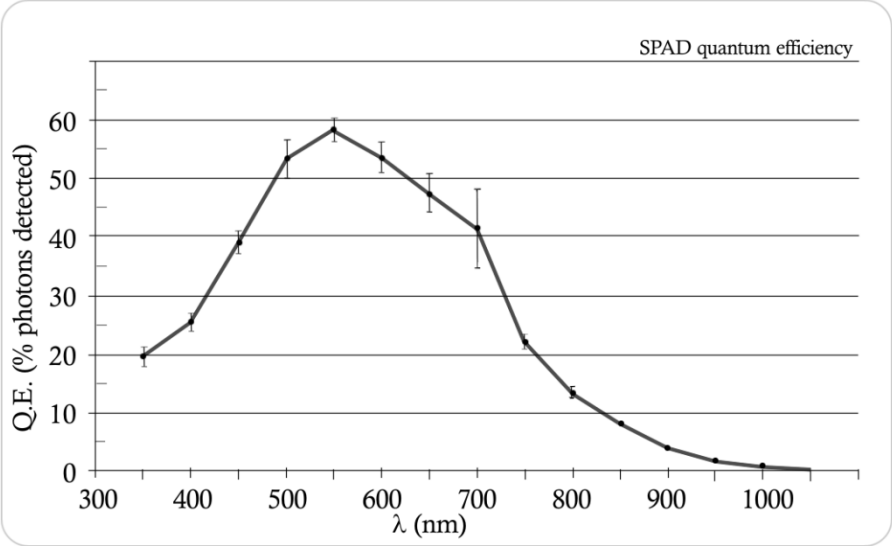

Figure 37: SPAD quantum efficiency in the 1050÷350 nm range measured at COLD laboratory in Catania.

Another important characteristic of SPADs, mostly involved in observations of faint objects, is the dark counts: detections due to random generation of charge carriers within the depletion region of the device, not related to real photon detections. In order to reduce the thermal carrier generations, the detectors are cooled at -10°C by a Peltier cell. We measured the dark counts in our laboratories finding an average value of 16c/s for the SAPDs A and C, 21c\s for the SPAD B and 26c/s for the SPAD D. The standard deviation is ~5 c/s for all. In Figure 38 four histograms relative to the SPADs are collected: the dark counts were measured every second in a 200 minutes long acquisition. Each histogram shows the number of occurrence along the acquisitions for a particular value of the measured dark counts in one second.

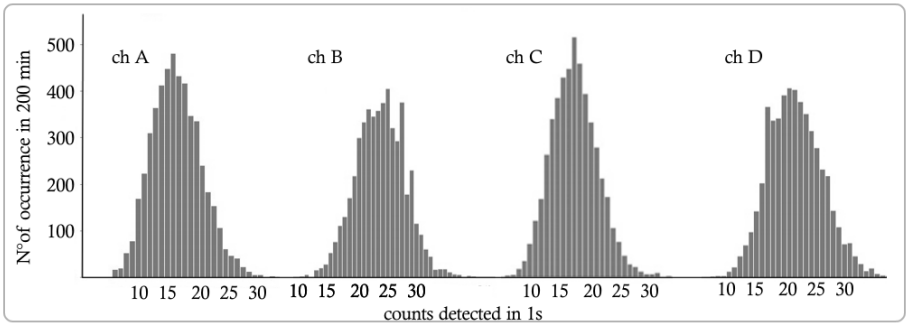

Figure 38: dark counts for the four IQuEYE SPADs.

Since our SPADs are a special selection carried by the producer, the average dark noise is ten times lower than the typical one listed in the datasheets ~250 c/s. [*mpd*]. However, at the faintest magnitudes, IQuEYE signal to noise ratio is limited by the detector dark count and not by the night sky.

Finally the overall quantum efficiency of IQuEYE has been estimated (further details in [IQ4] or [IQ11]) and is shown in Figure 39, with the expected sensitivity when using the three B, V, R and IR broadband filters. The global sensitivity curve is dominated by the SPAD efficiency (cf. Figure 37) and reaches a peak of more than 33% for 550nm.

Moreover the calculated exposure times needed to achieve the required Signal to Noise Ratio (S/N) per single SPAD in function of the target V magnitude is shown in Figure 40. The graph is obtained, assuming a source at zenith without moon light, a sky brightness of 21.9 mag/arcsec^2 (as indicated in [*esk*]) and a collected field of view of 3.5 arcsec diameter.

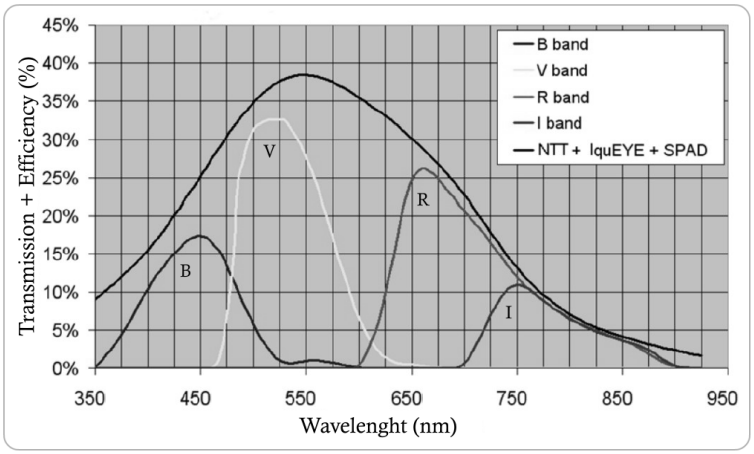

Figure 39: IQuEYE total effciency (black curve). Global system efficiency when using the broad band BVRI filters is also shown.

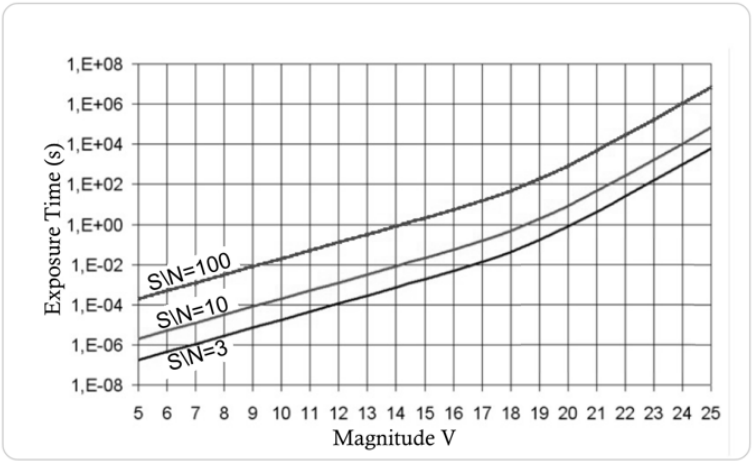

Figure 40: The calculated exposure time to reach a wanted Signal to Noise Ratio per SPAD (S\N in figure) for observations of target at the Zenith having the V magnitude listed on the X axis. The 3.5arcsec pinhole case is considered.

3 IQuEYE Improvement

The first run of IQuEYE at NTT was performed in January 2009. The instrument worked according with the performance expected acquiring a large amount of data. This first experience suggested some improvement implemented between the first and the second run, foreseen for December 2009. The main changes and the fixing of some problems are here summarized.

3.1 Optics.

3.1.1 Sky Monitor

In the first version of IQuEYE, the subtraction of the background signal was carried out by pointing the telescope in an area close to the target and acquiring the sky light for a few minutes. In the new version, also forecasting observations not only on rapidly variable objects, we added a fifth SPAD for the sky conditions monitoring. Through a small lens (6mm dia.) the light is collected and focused on a fiber that fed the fifth SPAD. This device collects light from an 8arcsec diameter sector, but only the central four arcseconds are unvignetted.

The position of the lens is fixed in the sky at 4arcmin far from the target (major mechanical complications did not allow us to achieve a closer position or a mobile system) and its orientation in the sky can be varied only using the NTT derotator to rotate the field of view. In particular it is not possible to acquire the signal from a reference star for photometric subtractions and this remain a problem for example for the issues treated in §.5.

The measured signal can be used to monitor sky transparency variations and the behavior of the overall electronic chain.

3.1.2 Lenses

As said in § 1.2, we used only commercial elements in the realization of original IQuEYE design: even if the performance of the system were nominally satisfactory, some data analysis pointed out that the residual aberrations could cause small fluctuations on the signal, when they are summed to bad seeing conditions or weather effect such as wind gusts that cause significant vibration of the structure of NTT. This kind of fluctuations takes place occasionally and they don't represent a problem observing quasi-periodic rapidly variable objects. Some problems could arise in photometric measurements of slow variable object or non-repeatable target behavior (an example is the exoplanet observation performed in July-August 2010, see §.5).

In order to reduce the residual aberrations we focus our attention on the last couple of doublets, (ref. to Figure 11) because they are the main source of them, since they work for beam aperture ~ *f/2,* condition in which commercial lenses not have high-performance.

We decided to change this focusing system designing a new couple of doublets, still spherical. Their design is depicted in Figure 41 where the ray tracing for the new custom optical train and the old one is shown.

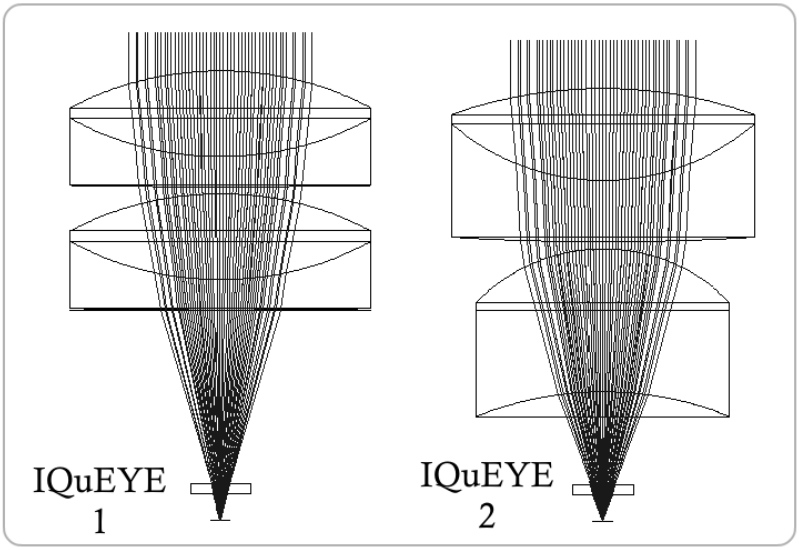

Figure 41: IQuEYE focusing system on the SPAD. Left: old catalogue lenses. Right: the new design, with custom made spherical lenses. The sensor is represented by the tiny line on the bottom. The last optical element near the SPAD sensor is the protection window, opportunely considered in the ray tracing.

These new doublets are conceived for working with output beam aperture ~ *f/1.5* bringing the total demagnification to 14.1. In this way they grant considerable improvements in terms of PSF shape and so the energy encircled over the detector area is increased.

The energy collected on the SPAD sensitive surface, in the case of a polychromatic 2 arcsec diameter source reach value very near 100% concentrating the 99% of the energy in a circle of 66 μm diameter.

Furthermore ray tracing analyses show that in the extreme case of a 5 arcsec uniformly illuminated polychromatic (420-720 nm spectral band) field of view, the 99.2% of the incoming photons are nominally collected by the SPADs.

Figure 42 shows a comparison between the encircled energy function of the first version of IQuEYE and the new one, performed for an extended uniformly illuminated source having 5arcsec diameter.

With the substitutions carried out, the optical system leaves more independence with respect to the real-world behavior of the instrument, conducing to an enhanced tolerance to poor seeing conditions or to centering errors.

In fig Figure 41 (right side) it is possible to notice that the distance between the sensor and the last lens surface is reduced: this forced the implementation of new SPAD support for the new aligning procedure.

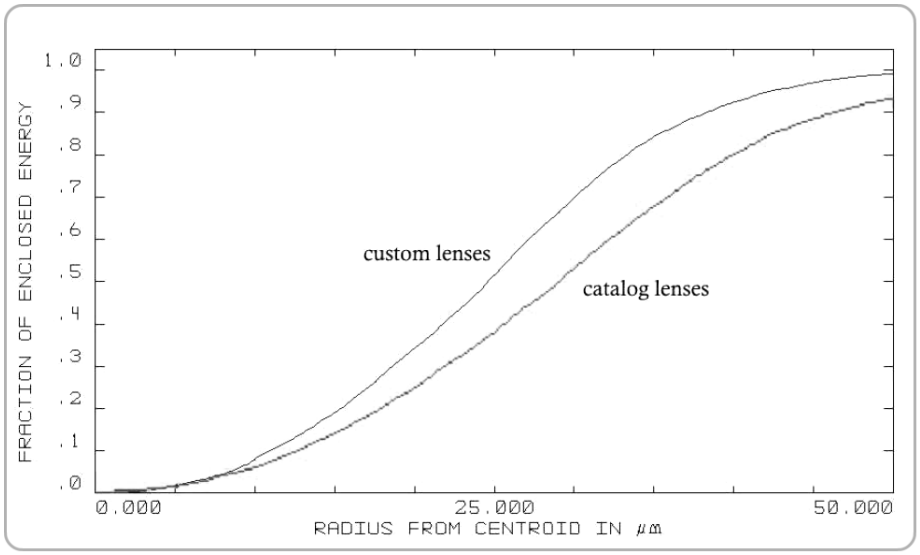

Figure 42: comparison between the optical performances of the two systems. The encircled energy function is plotted for a polychromatic extended uniformly illuminated source having 5arcsec diameter.

3.2 Mechanics

3.2.1 SPAD crosstalk

During the development of software for data analysis on very short time scales (see § 4), a peak of correlation between the intensities detected by the four channels, around the value of 2-3ns, was revealed. Results given by a crosscorrelation between the signals acquired by two SPADs is shown in Figure 43. The crosscorrelation is performed directly on the photons time-tags stream so the resolution is ~25ps and there is no binning in the data.

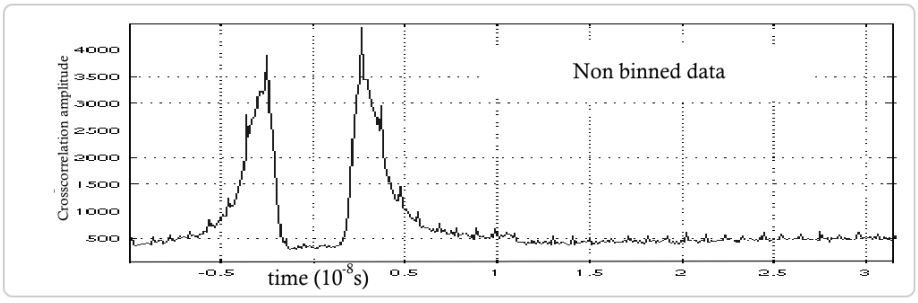

Figure 43: crosscorrelation between photons time-tags stream coming from two SPADs.

We checked the acquisition and de-rollover software, searching for bugs, without results, so we concluded that the signal had to be really detected from the TDC CAEN board. Because we have considered low

probability of electrical interferences (though all cables are gathered in a single pipe that leads them to the acquisition block), we concentrated on the optical part, considering plausible an internal reflection on any optical surface.

The surfaces of the lenses are treated with high quality anti-reflective coating, but 3 ns are approximately the length (in travel time of a light signal) that optically separates two SPAD.

As said, one of the largest drawbacks affecting SPAD is the optic cross-talk between the detectors. This phenomenon is due to photons emitted during the avalanche phase by the SPAD itself. When the incoming photon triggers the avalanche in the SPAD, secondary photons are emitted due to hot carriers relaxation. The emission spectrum ranges approximately from 500nm to 1500nm. Figure 44 shows the emission spectrum of a SPAD as measured in [REC]. Unfortunately a large part of the emission spectrum is overlapped to the frequency where the SPAD has quantum efficiency still not negligible. The result is that the new photons emitted can, in turn, give rise to new measures by the adjacent detector.

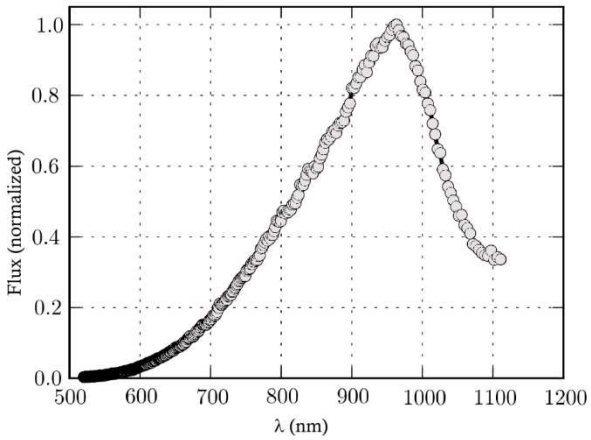

Figure 44: Measured SPAD emission spectrum . Image taken from [REC].

That photons are responsible for the after-pulsing detections in a single pixel device; if the current is quenched but the dead time is too short, some residual carriers could produce a new avalanche, not related with new photon detections. And for the same reason the multi-pixel SPADs devices have a low quantum efficiency: the photons thermally generated in one pixel can be detected by adjacent pixels giving rise to a “false” event. That imposes a limit to the array density because each pixel has to be shielded from the photons produced by the adjacent ones during their dead time. Figure 45 depicts a schematic representation of the phenomenon.

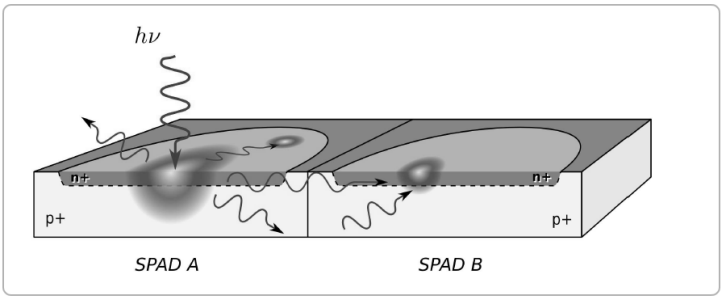

Figure 45: Schematic representation of optical crosstalk between two devices. Image taken from [REC].

We analyzed SAPDs whit a microscope: Figure 46 shows the 100µm SPAD's sensitive area. The image on the left shows a detector turned off and exposed to ambient light. When the SPAD is turned on, without any change in the illumination, on the sensitive area raises a slight luminescence (image on bottom-right side). Moreover it can be seen that the intensity distribution is not uniform and the peripheral zones are much luminous.

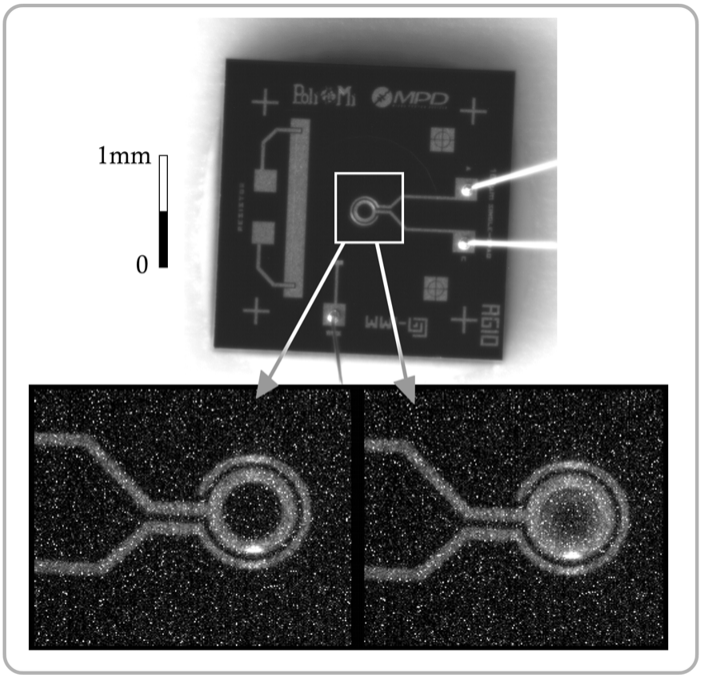

Figure 46: Microscope image of the SPAD sensitive area. Bottom-Left: the device is turned off and illuminated with ambient light. Bottom-Right: the light conditions don't change but the device is turned on. Photons are emitted.

Also if an ideal optical system is considered, this brightest annular region is a region that, in the conjugate-plane of the pinhole, corresponds to the annular region of the plate metal surface surrounding the hole. Or, in other words, the two 200 and 300µm diameter pinholes do not completely cover the detector and the light sent back from the edge of the detector do not enter the hole.

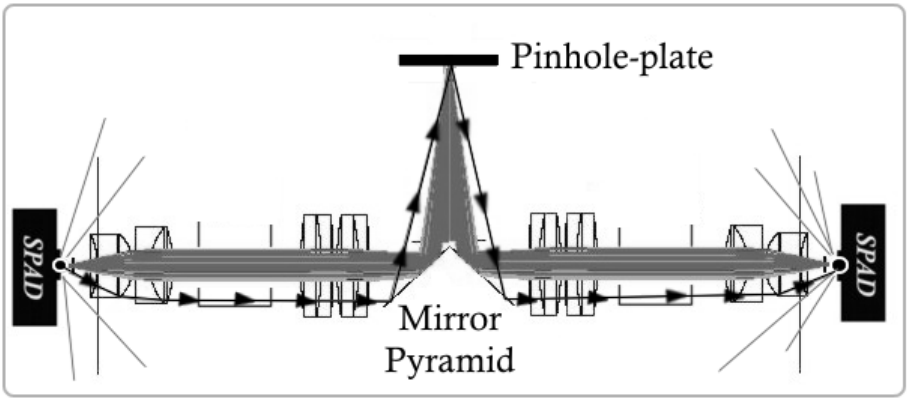

Figure 47: optical path between the pinhole and two opposite SPADs: the black light ray marked with the arrows emitted by the SPAD on the left travel through the optical path is reflected from the pinhole plate and continues til the second SPAD, on the right, where a false detection occurs.

To have an intuitive idea of the situation, in Figure 47 it is shown the optical path between the pinhole and two opposite SPADs: if the light rays (as the black one marked with the arrows) emitted by the SPAD on the left are intercepted by the last lens surface on the left, it goes to the plate and, after a reflection, it continues until the second SPAD, on the right.

Coming back to Figure 43, the number of photons involved in these false detections can be estimated and the detection probability is less than the afterpulsing probability (~1%). Moreover it can be seen that the phenomenon is not symmetric: if we consider the correlation between two SPAD, A and B, the peak for $t<0$ is determined by the false detection of A due to B emissions, vice versa the peak for $t>0$ arise because of false detections in B due to the light emitted by A. This fact can be ascribed to difference of reflectivity due to imperfections or slobbers on the pinhole plate. Unevenness of the plate is evident in Figure 48 where an image of the 300μm pinhole, taken with a microscope mounted on a beam analyzer, is shown. The light source is a dim led light near the optical axis of the system.

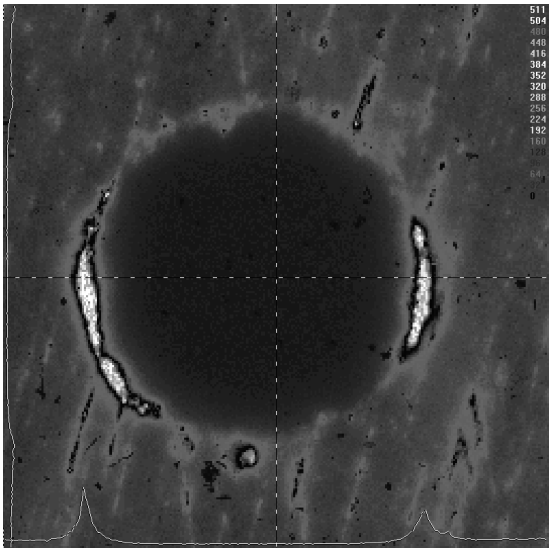

Figure 48: the 300µm pin-hole observed with a beam analyzer. The light from a lamp near the camera is reflected by the edge of the hole.

Actually this kind of problem can cause some complications in the analysis only if one is interested in a very short time-scale, such as, for example, the timing of statistical distribution of photons. In the other cases it implies only a decrease in signal acquired and, in the vast majority of cases, it is negligible (<<1%).

However, to overcome this problem, the plates of the pinholes were darkened with particular attention to the edge and the 200µm pinhole has been slightly tilted.

3.2.2 Minor changes

The mechanical structure of IQuEYE has been revised. The changes in the optical design needed the corresponded changes in the mechanical structure. Taking advantage of this, we planned a refurbishment in order to facilitate the alignment activities. In first version, indeed, the alignment phase was made more difficult by structural and design oversights (e.g. connections are difficult to reach once assembled the instrument, mechanical parts littered the access to optics etc…). Other changes was performed in order to help the mounting of the instrument at telescope (addition of a couple of handles, cover boxes to the SPAD's to avoid accidental knocks that could cause misalignment of the detectors etc.)

Actually the great part of these changes is not so important to be taken into account here*; we only mention, for the sake of completeness, that:

- the field camera position has been changed, from behind the horizontal bench, on the top of the same bench,
- the field mirror has been rotate in consequence.

* Further details in [IQ6].

- a middle section between the protective lid and optics was realized in order to reach the control boards, if needed, without removing the lid. This prevents dust from entering the instrument.

And, regarding the acquisition and storing system:

- The old server and a virtual machine were removed and, in their place, a new compact server equipped with Windows Server 2003 has been installed. The data storage capability during the observations has been increased at 2.5 Terabytes by a new 2 SATA HD; at the end of the observations, the data are copied on a 2 Terabytes external USB HD for subsequent processing.

PART TWO - Observations at NTT

4 Quantum Optics

4.1 Introduction

As already described in the introduction, the great majority of our knowledge of the Universe comes from the detection and the analysis of the electromagnetic radiation arriving from space, with the exceptions of a small fraction of data coming from material collected in space missions, detection of neutrinos and cosmic rays, meteorites and other extraterrestrial materials fallen on Earth and (hopefully) future detections of gravitational waves. However, an examination of the basic principles of the instrumentation for the electromagnetic radiation reveals that they all measures quantities related to the first-order spatial or temporal coherence of light (or some combination of these).

In other words, almost all the science performed on astronomical data can be described by referring to the first order correlation function $G^{(1)}$ for two coordinates in space *r* and time *t*:

$$G^{(1)}[r_1, t_1, r_2, t_2,] = \langle E^*[r_1, t_1]E[r_2, t_2]\rangle$$

where $E[r, t]$ is the electrical field at time *t* and position *r,* the asterisk represents the complex conjugation and $\langle \# \rangle$ the time average. In fact, almost all the instruments in use analyze quantities (spatial intensity distribution, spectra, polarization…) that can be ascribed to the *E*E* proprieties.

From a quantum perspective, that means limiting the analysis to observations of individual photons properties. For example, a photometer is a device that analyzes the function $G^{(1)}$ in the case of $r_1 = r_2$; $t_1 = t_2$ while a spectrometer could be seen as an analyzer for the case $r_1 = r_2; t_1 \neq t_2$.

Beyond this first-order correlation, light carries more information, encoded in the distribution of photons. This means that light with the same frequency and intensity could have different proprieties. Figure 49, albeit dangerous to a communicative point of view because it identifies the photons as small spheres defined with a particular position in space or time, can be understood as the corpuscular interaction of photons with a detector and it depicts the idea of different time distributions for beams of light having same intensity and same spectrum (same n° of photons with the same energy incoming in the detection device and detected at same position) but different "entropy levels". The presence of a photon is not statistically independent from each other and cannot be described by an isolated quantum state.

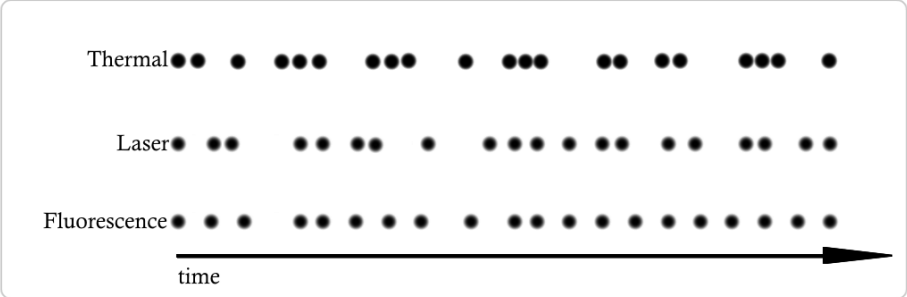

Figure 49: Statistics of photon arrival times in light beams with different entropies**.**

Such properties may be revealed by studying second (or higher) order degree of correlation, which reflects correlation properties of two or more photons. The second order (normalized) correlation function can be defined as:

$$g^{(2)}[r_1, t_1, r_2, t_2,] = \frac{\langle I[r_1, t_1] I[r_2, t_2]\rangle}{\langle I[r_1, t_1]\rangle\langle I[r_2, t_2]\rangle} = \frac{G^{(2)}[r_1, t_1, r_2, t_2]}{\langle I[r_1, t_1]\rangle\langle I[r_2, t_2]\rangle} \qquad \text{E1}$$

Where I is the intensity of the light and the denominator normalize the second order correlation function $G^{(2)}$.

In particular was found* that the distribution is strictly linked with the phenomena generating the light. The examples in Figure 49 show three different time distribution statistics. First is a "quantum random" statistic in which the photons tends to distribute themselves in bunches: this can be seen as a tendency of photons to be detected simultaneously by a detector. Photon bunching implies that the rate of coincidence at zero time delay is larger than the rate at finite delay t and, for brevity of notation omitting the part relative to r and denoting $g^{(2)}[t_0, t_0 + t] = g^{(2)}(t)$, we can write in this case $g^{(2)}(0) > g^{(2)}(t)$.

Thermal emission is an example of this detection statistic and can be classically explained by field fluctuations.

The case in which equality holds and $g^{(2)}(0) = g^{(2)}(t)$ corresponds to the second distribution in figure, that is a state where the detection statistic is quite similar to a "classical random" distribution (Poissonian). It could be obtained by laser emission, classically explained by coherent waves. But for quantum fields the inequality may be reversed. In this way the anti-bunching phenomenon depicted in third distribution of Figure 49 is obtained. This corresponds to a case in which the photons tend to avoid each other, and have no classical explanation. It was obtained, for example, from single photon emission by individual molecules or quantum dots fluorescence (see for ex. [LOU], [PTK], [BRO]).

The effect is detectable not only for photons but it is present for all identical bosons, including, for example, pions produced in high energy collisions. In Figure 50, adapted from [MAN], an example is given for the

* [GL1], [GL2], [GL3], [LOD], [ARE].

second order correlation function $g^{(2)}(t)$ calculated for ultra-cold helium gas*.

Top panel shows the $g^{(2)}(t)$ function for a beam of atoms obtained from a cloud of Helium just above the Bose Einstein Condensate transition temperature: the bunching is clearly noticeable since $g^{(2)}(0) > g^{(2)}(t)$ and the behavior of the atoms mirrors the behavior of thermal photons. For temperature under μK, the Helium gas confined in an external potential is subject to a phase transition and the new state is called Bose Einstein condensate (see for example[AND]). A beam extracted from the condensate presents the $g^{(2)}(t)$ function shown in the bottom graphics of Figure 50. In this case the time distribution of the atoms follows the statistic seen for laser photons ($g^{(2)}(0) = g^{(2)}(t)$) and it represents a coherent state for the propagating atoms. For this reason, this beam of atoms is often called atom-laser.

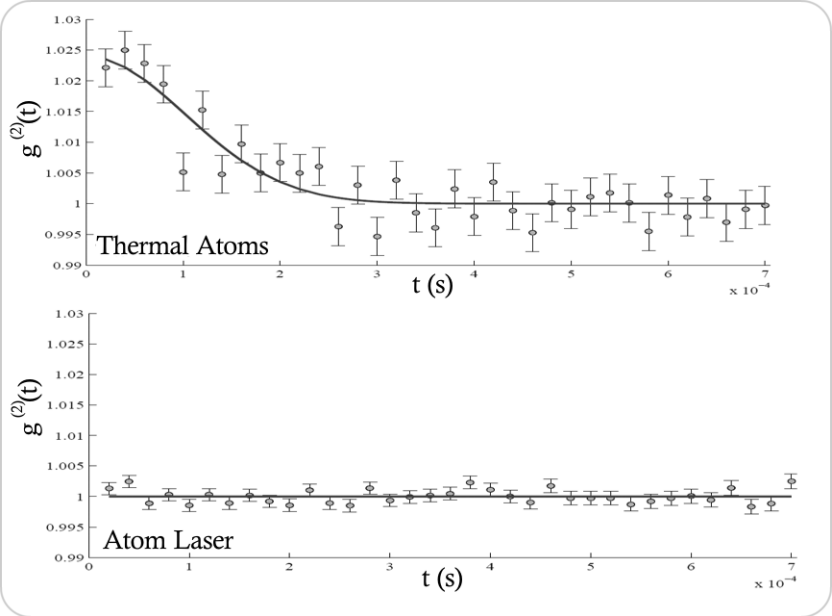

Figure 50: Plot of second order correlation function for thermal atoms at 850 nK (top) and for a pulsed atom laser (bottom). Image adapted from [MAN].

4.2 Quantum optics in Astrophysics

The information brought in the temporal coherence and in the spatial coherence has some significant differences. Simply put, the time distribution is related to the physical processes of light production in single or multiple atom systems, or to the physical process the light undergoes, while the spatial distribution could concern the spatial attributes of the emitting system.

* Actually He^4 is a bosonic composite that means a particle composed by an even number of fermions, which give a total integer spin, acting as a boson, at least for *large* space scales if compared with the dimensions of the composite.

As we did for the first order correlation function, we can consider the $g^{(2)}[r_1, t_1, r_2, t_2,]$ function calculated with $r_1 = r_2$ but for different t. This is the case of Correlation Spectroscopy, method known and used for various laboratory applications (see [BEC] for some examples) but never used in Astronomy. Correlation Spectroscopy makes possible spectral resolutions many orders of magnitude beyond classical spectrometers and could be employed in the field of astrophysics to recover important information on the nature of the light observed. One could search for natural amplified emission in atomic emission lines from extended stellar envelopes. For astronomical target, indeed, this spontaneous laser generation was predicted: If ionized plasma is rapidly cooled the electrons occupies the upper excited states and the population inversion, required for laser generation, may occur (see for ex. [JOH]); this envelope of recombining plasma can act as an amplifying medium for the star/pumping radiation. In this case part of the radiation follow a statistic in which $g^{(2)}(0) = g^{(2)}(t)$ (with the notation assumed in §4.1). Similar laser emission mechanism has suggested to explain the bright spectral lines observed in some astrophysical sources, as in the possible FeII laser mechanism in η-Carinae. In this case a 4-level laser scheme is proposed by Johansson and Letokhov in [JOH]. But these alleged laser emission lines are not yet spectrally resolved, and their width is suspected to be very far from the existing spectrometer capabilities. But the light coherence time for these emission lines is calculated to be of the order of some nanoseconds [DR3], thus detectable with a single photon photometer having ns time resolution, for a telescope large as VLT.

Other mechanisms for generation of light with non chaotic quantum statistics could be pulsar emission through stimulated synchrotron or curvature radiation, with calculated timescales of nanoseconds.

Moreover, quantum statistics of photons should permit to determine the Doppler broadening of a spectral line caused by motions of emitting atoms or by scattering in a medium [DR1].

Again, other discrepancies from the thermal statistics are proposed by Prendergast and Spiegel in [PRE] for photon bursts from photon bubbles in photo-hydrodynamic turbulence.

Actually the higher-than-one order correlation functions could, in many cases, retain some elements about the processes creating the light. Unfortunately those kinds of observations are beyond the IQuEYE capability, indeed a large flux of radiation, probably available only with the ELTs is needed to detect such correlations in the photon stream. Even the VLTs are at the limit to perform photoncorrelation spectroscopy for very bright star as η-Carinae or WR6 (V-mag~7) [DR2].

Going back to the $g^{(2)}[r_1, t_1, r_2, t_2,]$ function, a more approachable use is to consider the spatial coherence of the photons; the case in which the function is analyzed for $t_1 = t_2$, so the second order correlation function can be written as $g^{(2)}[t, r_1, r_2,] = g^{(2)}(d)$ where d is the path difference $d = \bar{r}_1 - \bar{r}_2$. Looking at the form of the equation E1 one can translate this

spatial coherence analysis in the study of the correlation intensity on short time scale between two (or more) detectors separated by a distance d.

The idea to use intensity correlation in order to obtain some information about the radiation source, instead of electromagnetic field correlation (for example using a Michelson interferometer), was developed in the 50s by two radio astronomers, Hanbury Brown and Twiss, with the aim of measuring the angular size of some radio sources. The optical analogue followed in a few years, flowing in the famous Narrabri Intensity Interferometer, which allowed the measurement of the angular diameter of 32 stars [HBD]. It was probably the only application of Quantum Optics in astronomy and it represented the mainspring for the development of this discipline in the following years by Sudarshan, Glauber, Mandel, Kimble etc.

Essentially the Hanbury-Brown and Twiss intensity interferometer (HBTII) consisted in two optical telescopes (of low quality -the star image has a diameter ~25mm-) placed at a variable distance (called the baseline) d. The diameter of the circular track along which the two telescopes could be moved was ~190m. The light collected was focalized on two 42 mm photocathodes then the photocurrent from the photomultipliers was sent to a wide-band amplifier, then to a phase-reversing switch and, after a broad-band filter (10-110 MHz), finally the signals was multiplied in an analogical correlator in order to identify the intensity correlations detected by the two telescopes.

In the next subsection we briefly describe the basic principle of intensity interferometry.

4.2.1 Intensity Interferometry

Let us consider two point-like sources X with coordinate $\bar{r}_x$ and Y in $\bar{r}_y$ radiating at the same frequency with (circular) wave number k and separated by $\bar{S} = \bar{r}_x - \bar{r}_y$. Two detectors v and w are placed at $\bar{r}_v$ and $\bar{r}_w$ and are separated by $\bar{r}_v - \bar{r}_w = \bar{d}$ (for clarity see Figure 51). We consider the case in which $Z \gg S$ or d.

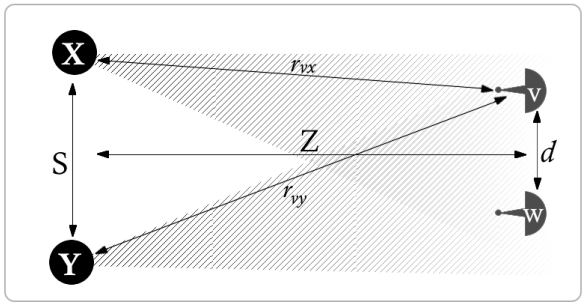

Figure 51: Sources and detectors displacement and variables used in the text.

The amplitude E_r^x of an electromagnetic spherical wave produced by X and measured in $\bar{r}$ in a given reference frame is:

$$E_r^x = \frac{A_x e^{i(k|\bar{r}-\bar{r}_x|+\phi_x)}}{\bar{r}-\bar{r}_x},$$

with A_x maximum wave amplitude and ϕ_x.random phase. Similarly, for Y, the amplitude at a position $\bar{r}$ is:

$$E_r^y = \frac{A_y e^{i(k|\bar{r}-\bar{r}_y|+\phi_y)}}{\bar{r}-\bar{r}_y}.$$

We are interested in intensity correlation between v and w in function of d, so we calculate the amplitude E_v in v due to the two sources. We denote with r_{vx} the distance between the detector v and the source X and with r_{vy} the distance between $v$and Y. (refer to Figure 51). So, considering $Z \gg S, d$ we obtain:

$$H_v = \frac{1}{Z}\left(A_x e^{i(kr_{vx}+\phi_x)} + A_y e^{i(kr_{vy}+\phi_y)}\right)$$

and the total intensity I_v in v is:

$$I_v = \frac{1}{Z^2}\left(|A_x|^2 + |A_y|^2 + A_x^*\, A_y e^{i(k(r_{vy}-r_{vx})+\phi_y-\phi_x)} + A_x A_y^* e^{-i(k(r_{vy}-r_{vx})+\phi_y-\phi_x)}\right).$$

A similar result can be found for E_w and I_w.
Averaging the intensities in time we find:

$$\langle I_v\rangle = \langle I_w\rangle = \frac{1}{Z^2}\left\{\langle|A_x|^2\rangle + \langle|A_y|^2\rangle\right\}.$$

The product of the temporal averages $\langle I_v\rangle \cdot \langle I_w\rangle$ is not dependent on d. But the product $I_v I_w$ performed before the time-averaging gives an extra term proportional to $\left(A_x^*\, A_y\right)\cdot\left(A_x A_y^*\right)$. Then a new time-averaging for $I_v I_w$ gives:

$$\langle I_v I_w\rangle = \langle I_v\rangle\langle I_w\rangle + \frac{2}{Z^4}|A_x|^2|A_y|^2\cos\left(k\left(r_{vx}-r_{wx}-r_{vy}+r_{wy}\right)\right) =$$
$$= \frac{1}{Z^4}\left\{|A_x|^4 + |A_y|^4 + 2|A_x|^2|A_y|^2\left[1+\cos\left(k\left(r_{vx}-r_{wx}-r_{vy}+r_{wy}\right)\right)\right]\right\}. \qquad \text{E2}$$

We can define the function g as follows:

$$g(Z,S,d) = \frac{\langle I_v I_w\rangle}{\langle I_v\rangle\langle I_w\rangle} =$$

$$= 1 + \frac{2\langle|A_x|^2\rangle\langle|A_y|^2\rangle}{\left(\langle|A_x|^2\rangle + \langle|A_y|^2\rangle\right)^2}\cos\left(k\left(r_{vx}-r_{wx}-r_{vy}+r_{wy}\right)\right) \qquad \text{E3}$$

If $Z \gg S$, so $k\left(r_{vx} - r_{wx} - r_{vy} + r_{wy}\right) = \bar{S} \cdot (\bar{k}_v - \bar{k}_w)$ with $\bar{k}_v$ the wave-vector of the light in v and $\bar{k}_w$ the same for w.

For a given d, the geometrical factor that multiplies k depend only by the distance S (de)magnified by the source distance Z, so the only unknown variable is related to S/Z. Or, in other words, for a given S/Z ratio (i.e. a given angular separation between X and Y, if $Z \gg S$), g varies in function of the detector separation d. So, the way in which $g(Z, S, d)$ varies with d gives information about the angular separation between the sources.

If X and Y are replaced by a continuous distribution, let say $\Sigma(\bar{r})$, then one can perform similar calculations to achieve:

$$\Im\left(\bar{d}\right) - 1 \approx \left|\int \Sigma(\bar{r}) e^{i(\bar{k}_v - \bar{k}_w)\cdot\bar{r}}\ d^3r\right|^2 = \left|\left(\hat{\Sigma}\right)\right|^2 \qquad \text{E4}$$

The correlation function is related to the Fourier transform (indicated with the hat $\hat{\#}$) of the source distribution.*

Basically, what the Intensity Interferometer does is to detect the correlation in intensity fluctuations based on the term with the amplitudes multiplication in equation E3: if the amplitude varies randomly, a positive fluctuation produce a correlated increase in signals measured by w and v, but the correlation decreases increasing the distance between the telescopes (the detectors) and between the sources, because of the cosine term.

Looking at what we said in §4.1, a thermal source emits photons with a statistics following the Bose distribution (bunched photons). The short-time intensity fluctuations are highlighted in E2 by the amplitudes multiplication term, if d is little enough to keep limited the argument of cos(#). On the contrary, if intensity of light are statistically flat (e.g. a laser emission), no effect arise from the multiplication term in E2.

From a classical undulatory point of view, the fluctuations arise from the beatings between the Fourier components of the incoherent light that two nearby telescope receive "correlated"; instead a coherent light does not allow these fluctuations.

Looking at the function g defined in E3 one can recognize the same function defined in formula E1 on page 68, $g^{(2)}[r_1, r_2]$.

One of the main advantages of Intensity Interferometer is the mechanical robustness: this technique is based on the detection of intensity fluctuations between different collectors and is insensitive to the light phase. Then the optomechanical requirements are very much less stringent than the Michelson interferometer case. Furthermore the atmosphere does not affect the performance of the instrument and, moreover, the mechanical stability implies the possibility to easy realize long baselines (d) and thus very high angular resolutions. A further advantage of intensity interfero-

* Result related to the Van Cittert – Zernike theorem.

metry over the phase interferometry is that it works over the entire visible spectrum, in particular in the blue

On the other hand, one of the major drawbacks of this technique is the need for huge fluxes of light. The interesting part of the signal is a tiny fraction of the total signal and it is overwhelmed by the shot noise. This very low sensitivity is one of the reasons why the technique has not been replicated since the time of Narrabri. In parallel, intensity interferometry has had a strong expansion in the field of nuclear physics: in particle and ion collisions is a useful tool to investigate the geometry of the collisions.

An example is given in Figure 52 taken from [JEL]. The first graph is the $g^{(2)}$ function for a stream of bosonic composites (He^4) plotted in function of the separation d=ΔZ between the detectors. Exactly as in the photon case, in this case the intensity (the number of atoms detected) correlation is analyzed. The attractive or repulsive Coulombian interactions between atoms are negligible; therefore, the behavior of $g^{(2)}$ is dictated by the quantum statistics of the bosons. A comparison with the $g^{(2)}$ function for fermionic composites (He^3) is given in the second graph. The shape of the fitting curve reveals details of the atomic ensemble spatial density generating the beam, exactly as in the photons case, since it depends on the angular diameter of the source.

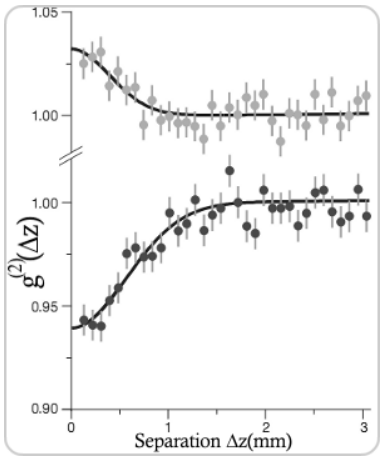

Figure 52:comparison of $g^{(2)}(d)$ function for fermions and bosons in the same apparatus, using two different isotopes of helium: He^3 (a fermionic composite) and He^4 (a bosonic composite)..

4.3 HBT with IQuEYE

Performing the HBT intensity interferometry means essentially to compare the signal detected by two telescopes separated by a distance d and to search for the coincidences in photon detection. The strength of IQuEYE-like instruments is the capability of storing the data as acquired at the telescope, without performing any manipulation. This, if there was an accurate absolute timing system (much beyond the threshold obtained

with IQuEYE) and two telescopes equipped with such kind of instruments, would allow the elimination of physical links between the telescopes and, so, the implementation of baselines d indefinitely long. On the other hand, the absence of a direct hardware correlator gives rise to the need for post-processing analysis of huge amounts of data. In this section it is presented the implementation of a correlator software for post-processing analysis and a first approach to the topics of Quantum Astronomy with IQuEYE.

4.3.1 Post processing Intensity Interferometry

IQuEYE stores the time tags of every photon coming from the target, digitalized at 25ps with 28bits. In particular for bright stars, those data take up a large amount of memory, for example an observation for a bright star produces approximately 100GB of data per hour.

For the correlation in time of the data acquired by two IQuEYE-like instruments, let's say with one SPAD each, the two chronological distributions of the detected events have to be compared. The original data are lists of 21bits-number* but, in order to perform the correlation, they must be placed in two "intensity temporal vectors" that associate the number of event detected in a time bin to a precise instant (when there's no event detected – the great majority of occurrence if the time bin is short – the element associated at that time exists in any case and is 0). For example, if ten photons are collected in 1s long acquisition, the original string is composed by ten 21-bits number. For a time-binning of 0.1ns the "intensity temporal vector" have 10^{10} integer elements, where, at maximum, $(10^{10} - 10)$ elements are 0 and the other ten are equal to 1. Performing a correlation on short time scales means increasing the number of time bins for a given acquisition time, so increasing the number of vector elements.

Usually, fast correlation functions are calculated by means of FFT algorithms, passing from time to frequency domain. The strings we have to correlate are *long* sparse arrays of bits. *Long* means that, for example, one hour of observations binned at 0.25ns (i.e. 10 times the CAEN board minimum time step) corresponds to arrays with 1.5×10^{13} elements: each string would have a dimension of ~ 2TB. Standard correlation algorithms would need an enormous amount of mass memory and the result would have a vast amount of useless information.

Such huge amount of data to handle make necessary the implementation of a software correlator working in different way, directly on the time tags t_i.

We implemented software based on the idea of using directly the time-tags without going through the construction of an intensity temporal vector. In a usual correlation procedure, the two strings of data to correlate are translated one respect to the other and, at each translation, the number of coincidences are counted.

* 21 for the time-tag + 7 used for other purposes, see §1.4.1

In the correlator software implemented, instead, the correlation function is obtained calculating the differences in time between one time-tag and all the others and then moving forward to the next time-tag. Indicating with t_i the time tags of the events detected by one SPAD (let's say the SPAD A) and with t_j' the time tags of the events detected by SPAD B, it is sufficient to increase by one the value of the correlation function at the time tag differences $t_j' - t_i$ ($t_j' > t_i$) for all the i,j events. Since we are interested in coincidences, it is possible to stop the process if the time differences exceed a conveniently chosen interval Δt (a coincidence window, in our case). The $t_j' - t_i < \Delta t$ restriction greatly reduce the computation time. This approach works on a smaller data set since it uses time tags and it does not require the *intensity temporal vectors* as above explained.

Figure 1Figure 53 shows a schematic idea of the correlator software core.

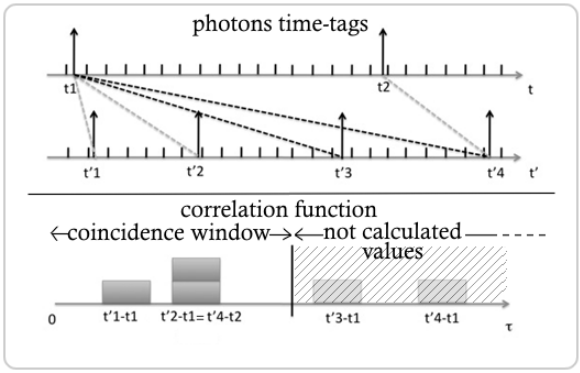

Figure 53: building the correlation function step by step: **Top**: SPAD A and SPAD B time-tags. Only the photons connected by the gray dashed lines are counted by the software. The photons connected by dark dashed have t_i-t_i'>Δt and they are not considered. **Bottom**: the correlation inside the coincidence window is calculated counting the number of equal t_i-t_i' differences.

The coincidence window Δt is chosen considering the instrument accuracy but a real critical analysis has yet to be discussed (see [IQ5] for details). We chose Δt =244.1ps, ten times larger than the CAEN board resolution, in line with the time-tags uncertainty found in §1.4.2.

4.3.2 HBTII test with IQuEYE

The design of IQuEYE allows the possibility of using each channel as a small isolated telescope: in fact the NTT mirror is subdivided in 4 sub-pupils each focused on a SPAD (see §1.2 for the details).

The collecting area of each sub-aperture is small (1\4 of the total area) and the baseline distance d are fixed (the physical distance between two portions of the mirror).

Actually no real astrophysical results were expected, indeed the baseline is not mobile and the maximum overall photon rate allowed by the tele-

scope is lower than the minimum rate necessary to achieve an acceptable signal-to-noise ratio.

We therefore develop this analysis tool foreseeing the last step on the way to QuantEYE: an observation with two larger and more widely separated telescopes, such as two VLTs, and two improved IQuEYE-like instruments. Nevertheless this is a first attempt of performing post processing intensity interferometry, avoiding real-time analog or digital correlators, which do not store the original data and need direct link between the detectors.

In practice, with our instrument, what we did is a zero-baseline observation. We tried to apply this correlator software to an observation performed on ζ-Ori (HD 37743, V mag=1.8, SpT=O9.5Ib). This star was chosen from the list of stars observed with the intensity interferometer at Narrabri [HBD]. In the paper the authors quoted a zero baseline correlation coefficient $g^{(2)}_{NARR}(0) = 0.6 \pm 0.06$, very far from the value of 1 expected for a single unresolved star. Their explanation was that the difference is due to the resolution of the stellar disk, corresponding to an angular extent of the order of 0.5 milliarcsec for a uniformly illuminated disk. (Actually ζ-Ori is a triple star, with the secondary approximately 2.5arcsec far from the primary, so near to the edge of IQuEYE pin-hole).

The star was observed on January 21st, 2009 at UTC (start) 01h06m24s for 1h8m through the wide band *B* and neutral density 2 filters (unfortunately, as said, the maximum count rate allowed by the timing system is around 8MHz), using the 5.2arcsec pinhole. This analysis can give an example of the computational saving obtained with our correlator software: the observation time lasts for ~1.7×10^{14} time units (the ~25ps TDC resolution) and approximately 2×10^{10} photons were detected and stored using 28 bits each. All the time tags of this observation were stored in 7771 files each of 10 MB, for a total of 78 GB, instead of the 21 TB needed to store all the time units for the creation of an *intensity temporal vectors* as described above.

Coming back to the HBT correlation, NTT diameter is 3.5m, while each Narrabri telescope had a diameter of ~6m. We than expected a value for the zero-baseline correlation function closer to that of an unresolved star, if compared to the one quoted by Hanbury Brown and Twiss. That is

$$1 > g^{(2)}_{NTT}(0) > g^{(2)}_{NARR}(0) = 0.6$$

We calculate the zero-baseline correlation between the six pairs possible of SPAD (we had 4 sub-pupils), and between the sub-pupils there are two effective distances for which the resolving angle is $\theta \approx \lambda/d$ with λ = 430 nm (Blue filter central peak). Table 4 summarizes the results obtained, assuming a time coincidence window Δt=244.1 ps. The data set was divided in seven subsets (1110 files each), and the reported values are the average of the seven obtained results. The Standard deviation column is simply the deviation obtained from these seven subsets, so it not represents the true error in the value of $g^{(2)}_{NTT}$

Table 4: Results for the calculation of zero baseline $g^{(2)}(0)$ for ζ Ori

Channel pair (SPAD id.)	Sub-pupils distance *d* (m)	Resolving angle θ (arcsec)	$\langle g^{(2)}(d) \rangle$	Standard deviation
A-B	1.7	0.052	0.886	0.002
A-C	2.4	0.037	0.912	0.003
A-D	1.7	0.052	0.931	0.001
B-C	1.7	0.052	0.909	0.002
B-D	2.4	0.037	0.909	0.004
C-D	1.7	0.052	0.932	0.004

The correlator software algorithm is very stable, in fact the obtained values in the signal fragmentations differs each other by less than 1%, moreover the results are internally consistent, and even gives values slightly less than 1 as expected.

However we emphasize that this analysis was not designed to provide a true measurement, but simply to confirm the feasibility of the technique. The small aperture of the telescope and the already mentioned limitation in the maximum rate tolerated by acquisition system provided a signal-to-noise ratio too low to achieve significant astrophysical results.

4.3.3 Outlook

We made a first attempt of quantum analysis with IQuEYE. But which results are obtainable with IQuEYE-like instruments? Here we try to estimate the capability of some configuration with different collecting areas and different number of SPADs available per telescope.

When considering a photon counting device such as IQuEYE applied to two telescopes each with collecting area A, the signal to noise ratio S/N is given by :

$$\left(\frac{S}{N}\right)_{RMS} = \frac{1}{2} A \cdot Q \cdot N \cdot \tau_0 \left|\gamma(\bar{d}, t)\right|^2 \sqrt{\frac{T_0}{2\Delta t}}$$

(see for ex. [FOE]) where Q is the quantum efficiency of the instrument, N is the number of photons from the star per unit of optical bandwidth, τ_0 is the coherence time of the radiation ($1/\Delta\nu$; for example the IQuEYE OIII filter has $\Delta\nu \approx 1$ nm = 1.2×10^{12} Hz), $\gamma(\bar{d}, t)$ is the complex degree of coherence (=1 for an unresolved source) and its absolute value is essentially what measured in the formula E4 on page 73, T_0 is the exposure time and Δt is the coincidence window defined above.

We performed an analysis in the visible, for 1h of acquisition. We have assumed the Q.E. as in §2.3 for a total Q=0.4 (including atmosphere, mir-

rors and detector quantum efficiency), $\Delta\nu$ = 1.2x10^{12}Hz (=1nm filter) and Δt =100 ps.

In Figure 54 the results for S\N calculation is shown in function of the star magnitude. The double line indicate the performance of the original Narrabri experiment (calculated using two 6.5m apertures, Q=0.2, $\Delta\nu$=10nm and Δt=10ns). The curves related to the IQuEYE-like instruments saturate at high fluxes because of the SPADs dead time. A pair of 1.8m class apertures (≈ a pair of 3.5m NTT sub-pupils) would provide data with S/N ratio (dark continue line) better than the Narrabri case. This is the case considered without acquisition limits: in the real case examined above, the 8MHz limitation in the acquisition system stops the curve below the S\N limit (horizontal line in figure). With more resources such limitation can be raised by at least a factor four even with current technology.

The other two curves show the expected S\N for a case similar to two sub-pupils of the VLT, i.e. two 4m apertures –light gray line– and with two 20m apertures, case similar to two sub-pupils of the 42m EELT –circles–. With the increase of the detection area, also the number of SPADs considered was increased, in order to raise the limit dictated by the dead time of the detectors.

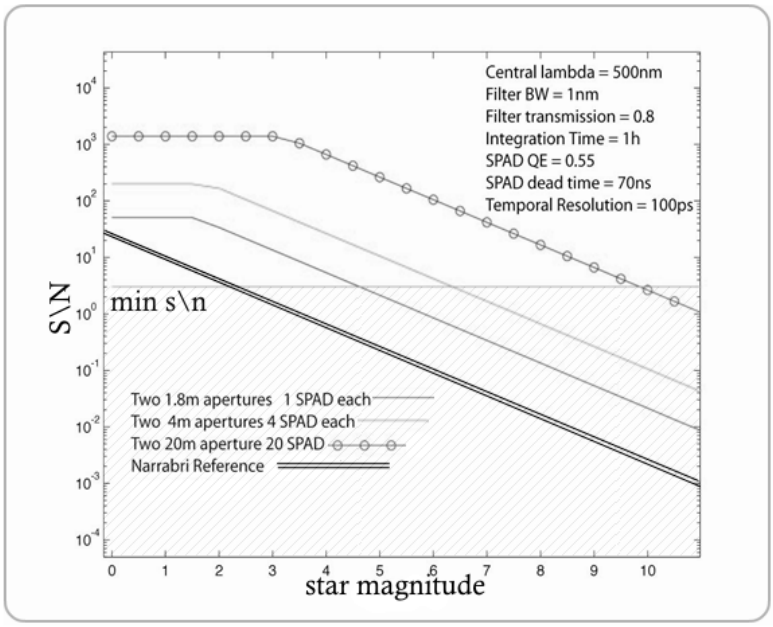

Figure 54: Signal to noise ratio (S\N) for IQuEYE like instruments attached to different telescopes, in 1h data acquisition time. The S\N is calculated for visible light after an optical bandpass with width=1 nm.

This analysis shown that two VLT, equipped with two IQuEYE-like instruments would resolve in blue and visible spectral band essentially all naked eye stars in the Main Sequence.

5 Exoplanet

In the last (for the time being!) NTT observation run we proposed a program for high speed photometry observations of three known planetary transits. We planned to use our instrument during the primary transits of Corot-2b, HD189733b, and WASP2b, plus other minor targets.

The main goal was to determine the mid-transit times with accuracy of the order of 1s, resolution that could allow the detection of a third body (characterized by a very small mass) in these systems.

Due to some problems that occurred in the new acquisition software in the storage of large quantities of photons, and that require a long correction in post processing, at the time of writing this thesis the data collected are still being analyzed, so this chapter presents only some preliminary analysis and is intended as further demonstration of the capabilities of the instrument.

5.1 Introduction to the topic

The study of extrasolar planets is a very new field, because bodies billion times fainter than stars around which they orbit are not easy to detect. Their existence was considered plausible for long time, but there was, however, no direct evidence of their existence.

The first discovery was announced by Van de Kamp in 1963, after many years of astrometric measurements, but was disproved ten years later. It took several decades and the development of new technologies, before they could really be identified: the first planet outside the Solar System was found around a pulsar in 1992.

In almost 20 years the explosion of the detection programs number and the implementation of increasingly powerful technologies have allowed us to achieve more than 500 discoveries. Dozens of programs ground-based and from space are still in developing phase, some close to starting (eg. GAIA in 2011), and some, more ambitious or based on different ideas, are still under study. For an overview of project in progress or proposed, see [*exo*].

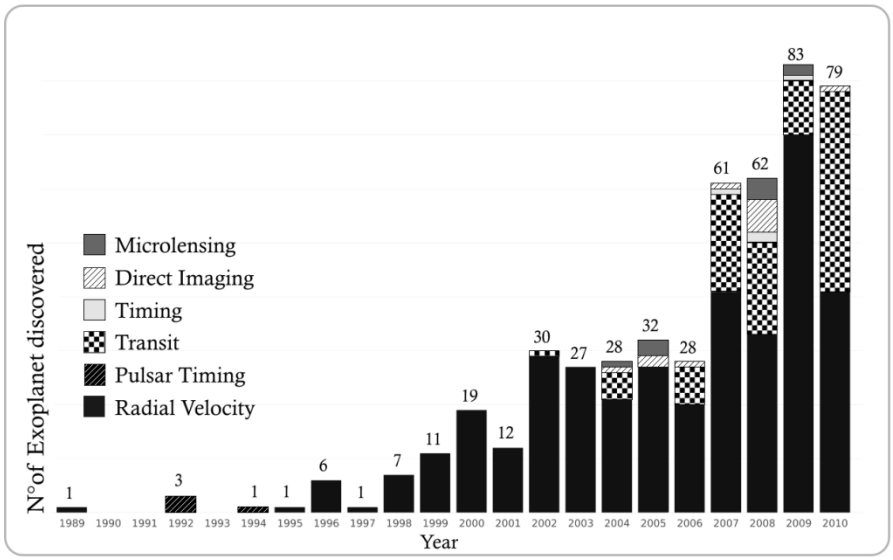

Figure 55: Number of extrasolar planet discoveries per year until 3 October 2010. The different texture indicates the detection method. Image adapted from [*epw*].

The methods to detect the presence of extrasolar planets are based mainly on the observation of the effects that they cause on their parent star, except for a few cases (today) of direct imaging. The ways to detect these effects are basically two: or the detection of perturbation in the star motion (with astrometric or spectral analysis) or the observation of the changes induced in the light received (reflections or shielding by the planet). Here it's briefly presented a quick overview of the methods used.

5.1.1 Exoplanets: detection methods

The technique that has allowed identifying the greater part of the extrasolar planets known and has so far detected hundreds of planets is the **radial velocity method**. The existence of a planet is inferred from the small-amplitude periodic variations it induces in the radial velocity of a star. The radial velocity method is similar to the astrometric, but it is not the star's position, but the star's spectrum shift that are being precisely measured as the star orbits around the barycenter of the star-planet system. The sensitivity of this technique to the massive planets, the short orbital period and to the low-mass stars with low intrinsic radial velocity variability is a heavy observational bias.

Similarly to the radial velocity technique, the **pulsar timing** is a way to find planets that orbit pulsars. Since minimal anomalies in the pulses timing is noticeable because of the great regularity of the pulsation, variations in the pulses arrival times can indicate the radial motion of a pulsar due to an orbiting body. The first known extrasolar planetary system, consisting of three terrestrial-mass planets around the pulsar PSR1257+12 was found by Wolszczan and Frail in the 90s using this method [WOL].

Another possible technique is the direct **high-precision astrometry** used to detect the tangential component to the optical axis of a star's motion due to an orbiting planet. By precisely measuring a star's position in

the sky and observing how that position changes over time, it is possible to infer the presence of a second body. In contrast to the radial velocity technique the astrometric method is more sensitive to planets in larger orbits, and can potentially detect less massive planets. This technique has not borne fruit, in fact only one planet VB10-b orbiting the star Gliese752B has been discovered in this way [*exp*].

The **microlensing technique** refers to the apparent brightening of a star due to gravitational lensing by a foreground star. If the source and lens-star are aligned, the apparent brightness of the source can grow even by an order of magnitude for some weeks. If present, a body orbiting the lens-star may distort the detected lightcurve. An analysis of the lightcurve can give information about the mass ratio and about the star-planet separation. This method is more sensitive to lower mass planets than the others seen above and it is currently considered to be the best way to detect terrestrial planets around ordinary main-sequence stars.

Obviously the method has no repeatability and this, combined with a low probability of alignment between lens-star and source, is a major limitation. To date only few candidate exoplanets have been identified. Microlensing searches are typically used in areas of high stellar density, such as, for example, the galactic center.

The most obvious method is the **direct imaging** of the planets: the reflected light from a planet typically is a factor of 10^9-10^{10} fainter than the parent star and the projected separation between the two bodies is at most 1arcsec. That makes the planet very hard to detect as a separate source. Some planets as Fomalhaut-b [KAL] or the three orbiting HR8799 (shown in Figure 56), have nevertheless been identified in recent years.

Another possible method consists in measuring **photometric variations of reflected light** due to the planetary phases. This reflected light would constitute a faint periodic photometric signal added to the light of the star. But also for high-albedo planets closer to the parent star, the variations expected are of the order of a few mmag, detectable only by space-based telescopes.

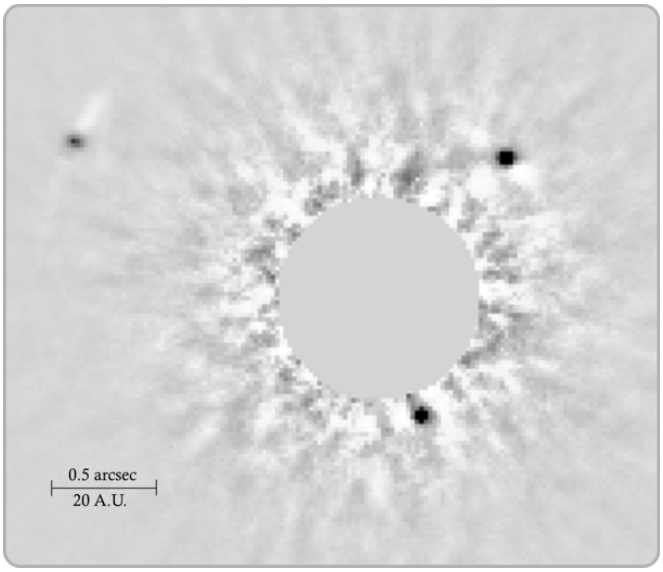

Figure 56: A K-band (2.2μm) image of the HR8799 planetary system, in the constellation of Pegasus, made using Gemini/Altair/NIRI and acquired on September 5, 2008.Planet b (top left) has about 7 Jupiter masses and orbits at about 70 AU, c (top right) is the ~10 Jupiter-mass planet orbiting the star at about 40 AU and d (closest to the star) has mass between 7 and 10 Jupiter masses and orbits at about 25 AU with an orbital period of 100y. In order to increase visibility of the planets the central star has been occulted. Image taken from [*gem*].

For a single pixel instrument such as IQuEYE, most of the techniques described here are forbidden. However, it remains the possibility of identifying the planet with **photometric measurements of the transit** if its orbital plane is parallel to the optical axis.

Basically the point is to measure the weak decrease that occurs in the light signal from the star when the planet passes through the line of sight. Having a model describing star edge luminosity, the light curve slope analysis can also give information about the spatial extension of the planet detected.

Such measures can be also refined in order to search for secondary bodies: a second orbiting body may change slightly the transit lightcurve intensity, producing a detectable signal in it. But if it does not happened, the second body may still be detected indirectly through the gravitational effects induced on the first body. There are two kind of effect that can be considered: in practice, the planet would appear to wobble during its orbit around the parent star then the transits would occur sometimes slightly earlier and sometimes slightly later than expected, causing an observed **transit time variation** (TTV) with an oscillation amplitude proportional to the mass of the perturber and to the distance of the perturber from the planet. But the gravitational effect of an extra body also would cause changes in the velocity of the planet each transit, and so in the duration of the transit too. This gives rise to **transit duration variation** (TDV). For most of the known transiting exoplanets, an exomoon can induce a TDV signal comparable and often larger than the TTV.

The main problem is related to the fact that TTV and TDV can be caused not only by gravitational effects of a third body but by a lot of other effects. These techniques require that a planetary transit be observed at least 3 times, because the effect of the rotation is a periodical time shift of the lightcurve mid-point or a contraction/distension of the transit duration.

5.2 IQuEYE and the Exoplanets

Transiting planets play a key role to the understanding of the formation and evolution of planetary systems. When photometric data are coupled with radial velocity data, it is possible to derive mass radius and density of the planet, and hence its physical structure can be understood. To date, space and ground surveys of transiting planets (Corot, HAT, Kepler, OGLE, SuperWASP, TrES, XO) have discovered over 60 planets and the number is constantly increasing. The vast majority of these planets are the so-called hot Jupiters, with orbital periods of few days. Few Neptune-mass transiting planets (like Corot 7b, GJ 436b) are also known. As said, detection of super-Earth planets could be performed measuring transit time variations (TTV) or transit duration variation (TDV). The measurement of the mid-transit times with high temporal resolution can be used to detect the presence of a third body perturbing the orbit of the known transiting planet. This technique is more sensitive to resonant orbits of the third body, because the induced variations are larger. For the detection of these planets, mid-transit times need to be measured with accuracy better than 10 seconds [SRT]. Current knowledge of transit mid-time for the three planets proposed for observations is around 15 s. Analysis of HD189733b transits obtained with MOST satellite have excluded only the presence of very massive perturbers and planets of masses larger than 1-4 earth masses [MIR]. A search for Trojan planets (i.e. a planet orbiting in the Lagrangian point of a star and a massive planet) in known transiting systems was performed by Madhusudhan and Winn in 2009 [MAD], combining photometric and RV data. The authors obtained upper limits on mid transit-time variations of the order of several minutes for each planet analyzed. To exploit the possibility of detecting small exoplanets, several instrumental features are needed: high quantum efficiency, high temporal resolution, high stability and high accuracy clock running for hours, acquisition devices capable to sustain high photon rates. Our instrument fulfills all these requirements, and offers additional benefits like the possibility of simultaneous observations in multiband (§ 291.2).

TDV due to an Earth-mass planet orbiting around our target planets is of the order of 40 s, which can be easily detected with temporal precision granted by IQuEYE. TTV could be of order of minutes for a third body near a resonance, so easily detectable, but also we can infer very low limits on the masses of additional perturbers. As mentioned, the possibility to perform simultaneous observations in 4 different bands is another unique characteristic of IQuEYE. We have planned to use these characteristics during the data analysis of the planetary transits for estimating the differ-

ences in the depth of the transits and then estimate the stellar limb darkening coefficients that is in some way related with the composition of the planetary atmosphere. During the transit, in fact, the height at which the planetary atmosphere becomes opaque to the grazing star light varies with wavelength. The depth of the transit at various wavelenght, which is related to the planetary radius, allows one to recover the transmission spectrum of the planetary atmosphere along its limb.

As mentioned earlier, during the observations a problem in the acquisition software was noticed. After the changes to the instrument and the addition of the fifth SPAD for the sky monitoring, which needed a change in the acquisition software, the acquisition board, especially at high flow rates (the magnitude of the star hosting the listed target are between V=10 ÷ 12) gives a large number of error messages in data files, although the data are correctly stored. The presence of these warnings, however, makes impossible the de-rollover automatic procedure. Waiting for the implementation of a script for automatic cleaning of data, few acquisitions were cleaned by hand and analyzed.

5.2.1 A transit: WASP-6 b

Figure 57 shows the normalized signal detected from WASP-6 on 31 Jul 2010 (few days after the full moon). The transit observed refer a sub-Jupiter mass planet transiting every 3.36 days a solar-type star of magnitude V=11.9. Data is binned in 1s bin (for clarity we show only the 20% of the points). The airmass trend is removed with a low order polynomial. The acquisition is performed through the 6.1 pinhole and, in order not to lose the correct centering of the detectors (see § 1.2.2) defocusing the image was not considered appropriate.

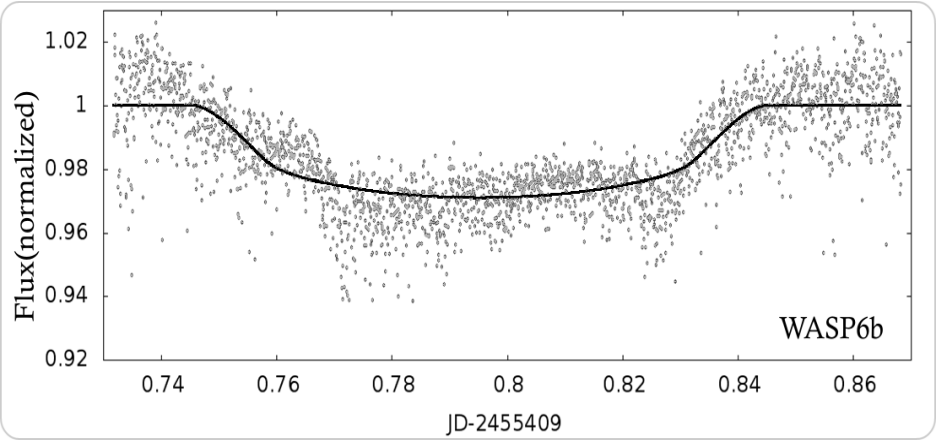

Figure 57: WASP-6 b light curve. The x-axis report the fraction of the Julian day. The time bin is 1s and, for clarity, only the 20% of the points is shown. The airmass trend is removed using a low order polynomial.

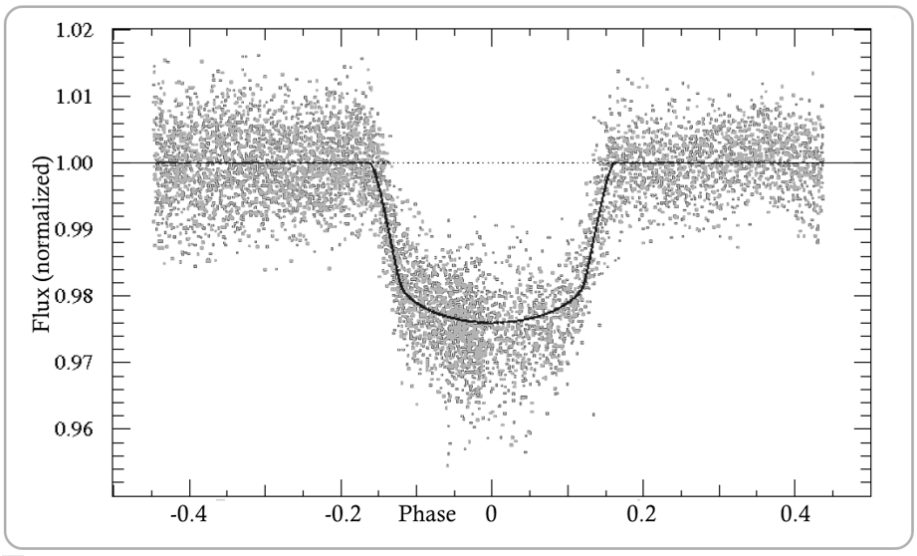

Figure 58: Wasp-6 light curve folded over two night of observation taken from the discovery paper [GIL].

The results of the preliminary analysis are in perfect agreement with the discovery paper of Gillon et al [GIL] from which Figure 58 was taken and presented here for comparison. We determine the mid transit time as Tc=2455409.795296 ± 5 s, value that has an accuracy 2 times higher than that quoted in the discovery paper.

Table 5 reports some physical characteristics and orbital parameters of the exoplanet observed as inferred in [GIL].

Table 5: Basic data for WASP-6 b. From [GIL].

Distance	307 pc
Mass	0.5 M_J
Radius	1.2 R_J
Orbital period	3.36 days
Semi major axis	0.04 AU
Eccentricity	0.05

5.2.2 Conclusions

The results obtained are very preliminary and it is possible to improve them in the near future simply by using correct limb darkening parameters for our system response. Another shrewdness is the removal of the airmass trend and other systematic (as, for example, the flux variation due to the moonlight hitting the gray side of the telescope building) not using a simple model but the data collected with the field camera.

With regard to the optical design of the instrument, the fact that IQuEYE cannot perform imaging represents a problem for this kind of observations, mostly because it is not possible to have an acquisition field obtained with the same kind of detectors acquiring the target. Such acqui-

sition would allow the direct analysis of the various spurious contributions and changes in intensity not due to the target. However as a good stopgap measure for this lack may be represented, as said, by the use of the data collected with the field camera. The fifth SPAD is not mobile and only provides information about the sky brightness (or a fixed point in the sky) and it is not possible to point a target at will. Some solutions for a new version of the instrument were considered: without referring to the arrays of SPAD still under development, an alternative is a SPAD fed by an optical fiber (as the actual sky monitoring SPAD is) in with a non bulky optical tapering can be positioned as desired by a precision movements on a target in the FOV, detected through a sliding field mirror.

However, although almost all of the data must still be analyzed, looking at the few ones presented here, it is possible to see that, thanks to its characteristics, IQuEYE can improve the current precision timing of the transits and it can be used in a field for which it was not conceived, thus strengthening the reasons for the use of very fast photometers of such kind.

6 Pulsars

Pulsars are strongly magnetized and fast rotating neutron stars, the result of the massive core collapse after the supernova at the end of its life. Neutron stars have been theorized since the 1930s and in the 1960s, they were discovered at Radio frequencies. Their radii should be of the order of few kilometers and their masses of the order of the Chandrasekhar mass (~1.4 solar masses) or higher. Their central density reaches values of a billion tons per cubic cm.

Their pulsating electromagnetic radiation was observed over the whole spectrum but, even though pulsars have been known for the last 50 years, the mechanisms producing the emission of electromagnetic radiation are hardly known. Is commonly accepted, although not verified, that the emission of electromagnetic radiation is related to relativistic electrons and positrons accelerated by the electric field induced by the strong rotating magnetic field. Photons are emitted by the charged particles by means of the synchrotron mechanism or other mechanisms theorized in the models. Pulsars are the equivalent of lighthouses on a neutron star.

Non-thermal radiation at a variety of wavelengths is emitted through the magnetic poles, which are generally misaligned with the spin axis. We see a pulse at the Earth every time this magnetic axis points towards us.

In order to better understand the mechanism underlying the radiation emission and the equations of state of the neutronized matter, it is useful to increase the observational knowledge of these objects, nowadays very studied but not yet fully understood. This chapter contains the results of the analysis performed on the optical signal of the three observed pulsar: PSR B0531 +21 or Crab pulsar, PSR B0540-69 pulsar in the LMC and the PSR B0833-45, the Vela pulsar. The data was collected during the three observation campaigns at NTT but here it is presented only the data of January and December 2009. The first part of the chapter is devoted to a rapid overview on standard analysis methods, and then the work carried out with particular tools for each pulsar is described.

The results obtained lead to the conclusion that, at least for the observation of rapidly varying objects, it is worth to continue on the road taken in the developing of ultra-fast photometers as IQuEYE.

6.1 Data analysis

6.1.1 Precise time tagging

Going back to what was said in § 1.4, the final datum coming from IQuEYE consists in a series of time-tags digitalized at 25ps. Where the analysis of acquired data requires a high temporal precision, the effects of motion of the Earth along the entire frame of acquisition and other minor effects could no longer be considered negligible. It is, indeed, the case of

pulsars that require extremely accurate timing analysis. Before any kind of analysis on the signal detected from a particular target, it is convenient to "correct" the times of arrival (ToA) of every individual photons so that the contributions of apparent contractions or expansions of the signal are eliminated or, at least, minimized.

For this purpose we made use of a tool widely used in radio astronomy, called Tempo2 [*tem*], a software devoted to model with extreme precision (nominally 1 ns) ToAs as collected by an inertial observer.

The largest effect to correct is due to the proper motion of the Earth, therefore Tempo2 process the times of arrival of photons in a way that make them as they would be acquired in a reference frame that approximates an inertial frame. Each ToA is modified by considering the motion and the position of the Earth at the moment in which it was acquired, in this way the rotation and revolution effects are corrected and the ToA is hence referred to the solar system barycenter.

The Tempo2 models consider also the polar motion of Earth, on the contrary the previous version of the software (Tempo1) does not: this fact gave us some trouble in the comparison between radio data treated with Tempo1 and our data, as we will show below.

The frame obtained in consequence of these modifications is only "quasi-inertial" and further corrections are needed. Tempo2 take in account the space-time distortions due to the presence of massive bodies of the solar system. The curvature of the photons trajectories introduces a delay on ToAs, known as Shapiro delay, dependent on the mass and positions of the perturbing bodies and on the angle formed between target-telescope-perturbator. The bodies considered in the model are Venus, Jupiter, Saturn, Uranus Neptune and, obviously, the Sun. Another correction performed is related to the time dilatation induced by the gravitational potential of the solar system itself, in fact, in a gravitational field, clocks run slower and this effect is also differential, depending on the gravitational potential the clock lies in. This effect is known as Einstein delay.

The photons incoming from the pulsar travel through the interstellar medium which acts as a dispersive medium, causing differential delays on ToAs, depending on the radiation frequency. That dispersion could become relevant, for example, in the comparison between optical and radio frequencies (as is done in § 6.2.3). This kind of corrections needs a model of the dispersion measure of the interstellar medium (see [BAK] for an example). The proper motion of the pulsar also introduces effects affecting TOAs and needs to be taken into account.

In summary, the corrections to theToAs performed by Tempo2 can be written as follow:

$$\Delta t = \Delta_C + \Delta_A + \Delta_{E_\odot} + \Delta_{R_\odot} + \Delta_{S_\odot} - \frac{D}{f^2} + \Delta_{vP} + \Delta_B$$

Where Δ_C is a term that contains various clock corrections transforming the time in Terrestrial Time, Δ_A is the Earth atmospheric propagation delays, $\Delta_{E_\odot}$ is the Solar System Einstein delay, $\Delta_{R_\odot}$ is the Solar System Roemer delay, $\Delta_{S_\odot}$ the Solar System Shapiro delay, the term D/f^2 models the dispersive component of the light travel time, Δ_{vP} describes the excess vacuum propagation delay due to secular motion of the pulsar and Δ_B contains terms that describe any pulsar orbital motion (used mostly for binary systems).

The description of how the software models and corrects all the effects mentioned is beyond the scope of this thesis, for further information the reader is referred to [TE1] and [TE2].

Table 6, taken from [TE1], shows the typical order of the corrections performed by Tempo2 to each individual effect considered. The third column shows which corrections were also implemented in the previous version of the software, Tempo1.

Table 6: typical order of the corrections performed by Tempo2. Data taken from [TE1]

Correction	Typical value	Tempo1
Observatory clock to TT	1 μs	✖
Hydrostatic tropospheric	10 ns	
Zenith wet delay	1.5 ns	
Precession/nutation model	5 ns	(*)
Polar motion	60 ns	
Earth rotation	1 μs	✖
Einstein delay	1.6 ms	✖
Roemer delay	500 s	✖
Shapiro delay (sun)	112 μs	✖
Shapiro delay (venus)	0.5 ns	
Shapiro delay (jupiter)	180 ns	
Shapiro delay (saturn)	58 ns	
Shapiro delay (uranus)	10 ns	
Shapiro delay (neptune)	12 ns	
Solar Shapiro delay (2nd order)	9 ns	
Interplanetary medium dispersion	100 ns**	✖
Interstellar medium dispersion	1 s**	✖

*Tempo used an earlier precession/nutation model.

**Observing frequency and pulsar dependent, typical radio value listed.

6.1.2 Tools for standard analysis

Of course in photometry the direct analysis of the signal is the best solution, but this may not be possible when the signal is not strong enough, so it is necessary to use different techniques of analysis, which will be presented here very briefly. There are a lot of approaches for the analysis of the variability in time of astrophysical sources and the choice for the most appropriate depends on the timescale involved, the intensity and the duration of the signal collected. For sources pulsating, as in our case, on short time scales (tens of ms), a first technique to find a periodic or quasi-

periodic behavior is the Fourier analysis, here not described and on which we do not dwell in detail, considering it known. For example in Figure 59 the Fourier transforms for the three pulsars are collected. All three panels are obtained from acquisitions 60 minutes long.

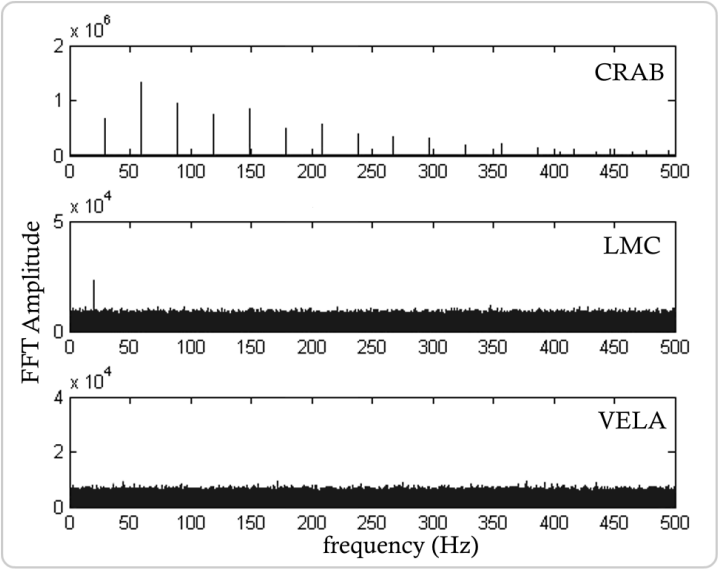

Figure 59: FFT for the three pulsars observed. The respective magnitudes are: V=16.5 for the Crab Pulsar, V=23 for the LMC Pulsar and V=23.6 for the Vela Pulsar.

In the Crab FFT the peaks are evident with all the harmonics, while for the LMC pulsar only the main frequency is visible. No special features seems to be in the third panel for the FFT on the Vela pulsar signal.

In a similar way, information about the periodicity of the signal and the shape of the pulse can be recovered through an autocorrelation analysis: Mathematically, under precise conditions, we can define the function $c(\tau)$, the convolution between two functions $f(t)$ and $g(t)$ as

$$c_{fg}(\tau) = [f * g](\tau) = \int_{-\infty}^{+\infty} f^*(t)g(t+\tau)dt \qquad \text{E5}$$

where the superscript asterisk denote the complex-conjugate operation.

Applying the convolution between the signal and itself $c_{XX}(\tau)$ the randomly distributed noise tends to produce a constant contribution for each value of τ, while the repetitions of the intensity peaks periodically overlap, giving rise to peaks in the function c_{XX}. A slight shift of the period can be noticed by analyzing the tail of the autocorrelation function, where the peaks tend to broaden and to become lower. For a discrete and finite vector $X=(x_1 \ldots x_N)$, i.e. the binned signal, E5 can be expressed in the form:

$$C_{xx}(i) = \sum_{k=1}^{N-i} (x_k - \bar{x})\,(x_{k+i} - \bar{x}) \Big/ \sum_{k=1}^{N} (x_k - \bar{x})^2$$

that is the normalized autocorrelation function for the vector X. In the formula the second summation and the difference with $\bar{x}$ take in account the normalization of the function C_{xx} forcing $C_{xx}(0)$ to be equal to one; N is the length of the vector X and $\bar{x}$ is its mean; i is an integer number and it represents the lag between the two correlating vectors (that is X and X itself in the case of autocorrelation) as the variable τ in formula E5. An example of autocorrelation for the data of the Crab pulsar is shown in Figure 60 with i varying in steps of 1ms.

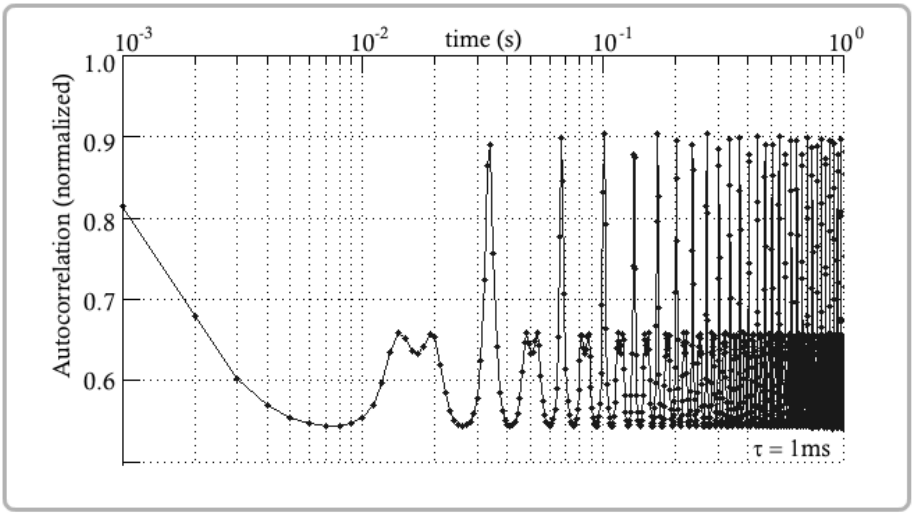

Figure 60: Autocorrelation of the Crab pulsar signal.

In order to obtain the shape of the original emission from the source (the so-called light curve), a standard technique, called phase or epoch folding technique, is used. The basic idea is fairly similar to that summarized in the paragraph devoted to the autocorrelation function: the contribution of the noise can be considered random distributed on each period of rotation (each phase), consequently its average contribution to the light curve is flat. On the contrary, the pulsar signal immersed in the noise is periodic (for the moment we can consider negligible the slowing down of the rotational period of the pulsar) and it gives a non flat contribution, detectable by putting in phase the periods.

So, starting from the signal opportunely binned in an N-elements vector $X=(x_1 \ldots x_N)$, the first stage is to subdivide X into intervals of length equal to the seed-period P_s obtained through the Fourier Transform or the Autocorrelation of the signal. If necessary, the length of the time bin can be slightly modified in order to obtain an integer number (let's say q) of bin per period.

The second stage is to sum in phase all the periods in the vector, that means the sum of the vectors $[(x_1 \ldots x_q)+(x_{q+1} \ldots x_{2q})+\ldots+(x_{kq-q+1} \ldots x_{kq})]/k$ where k is the number of periods contained in the whole observation. The result is a vector $Y=(y_1 \ldots y_q)$, the folded light curve.

The third stage is dedicated to the choice of the best period and, so, the best light curve: the value of the initial period P_s can be slightly changed, obtaining variations in Y that can be considered as a q-dimensional func-

tion of the period *P,* Y(*P*)=(y_1(*P*)…y_q(*P*)). A chi-square test is performed on Y(*P*), looking for the maximization of the χ^2 with respect to the average value of the series.

$$\chi^2(P) = \sum_{i=1}^{q} \frac{(y_i(P) - \bar{y})^2}{\sigma_i^2} \qquad \text{E6}$$

where, summarizing, *P* is the independent variable period chosen around P_s, *q* is the number of bins the folded light curve is divided into, $\bar{y}$ is the average value of the signal and σ_i is the associated error of the i^{th} bin. Maximizing E6 in function of *P* means that the corresponding light curve is far from being statistically consistent with a flat curve, and this value of *P* maximizes the repetitiveness of the signal for each P. Further details can be found, for example, in [LE1]

The error on the period P_χ obtained in this way can be estimated through a formula derived by Larrson in [LAR] that follow a work by Leahy [LE2]:

$$\sigma_P^2 = \frac{6\sigma_{tot}^2}{\pi^2 N T^2} \frac{P_\chi^2}{\sum_{j=1}^{m} j^2 A_j^2} \qquad \text{E7}$$

in which σ_{tot} is the standard deviation of the unfolded signal vector X, *N* is the total number of elements of X, *T* is the total time length of the acquisition and the summation is a weighted sum over the many Fourier components of the signal, calculated through an iterative fit procedure. The formula will not be discussed here and for information on how it was derived, the reader is referred to [LAR].

6.2 Crab Pulsar

PSR B0531+21 in the Crab nebula is the brightest optical pulsar and one of the most observed objects in the sky. It is a 33ms pulsar emitting in the whole spectrum, the first to be detected as a pulsating source in the optical band and it is the pulsar by which it was understood the link between pulsar and supernova explosions.

Since it provides a relatively bright (V=16.5) highly periodic signal and thanks to the large amount of data in the literature, as well as numerous observations for comparison, it represent an excellent test bed for IQuEYE.

The observations we performed are spread over a period that covers a year and half, between January 2009 and August 2010, although the acquisitions in August were devoted mainly to the exoplanets area and those dedicated to crab are concentrated mainly in the first two run.

The analysis procedures described in the previous section was applied to the large amount of data collected. Arrival times of detected photons are

corrected to the Solar System barycenter using the software TEMPO2 and most of the analysis was performed with timing analysis software XRONOS2 v.5.21, [*kro*]. To give an idea of the quality of the data collected and, so, of the capabilities of IQuEYE in conventional high speed photometry, Figure 61 shows the resolved 33ms single pulses of the Crab pulsar. The signal is binned at 0.5ms and the pin-hole in use is the 5.2" one.

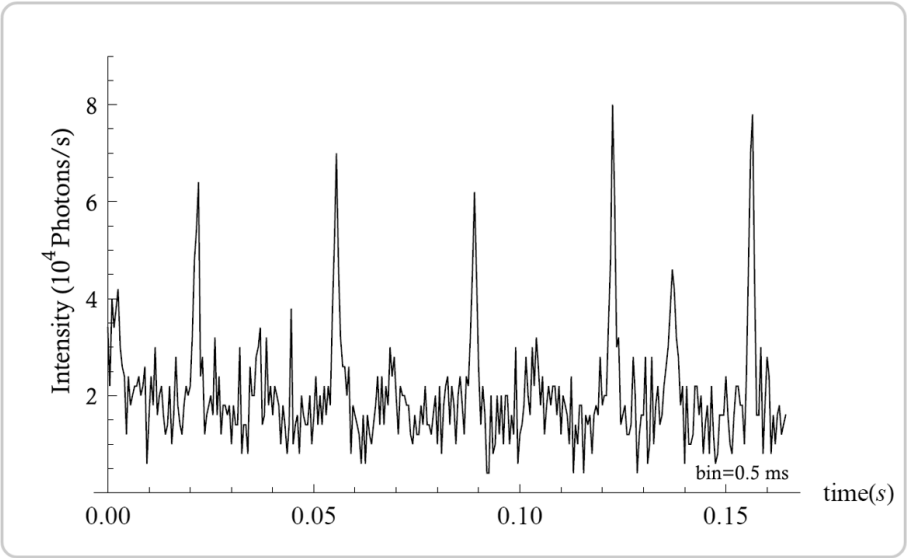

Figure 61: The first five pulses detected from the Crab pulsar. The bin time is 5×10^{-4}s

6.2.1 Standard analysis

We searched for periodicities by folding the data over a range of periods and by looking for a maximum chi-square as a function of period. In Crab pulsar case, the $\chi^2(P)$ function is absolutely well peaked and identifies a precise period. In Figure 62 an example is given. A folding performed for a 15 minutes long acquisition give the result depicted in Figure 63. The statistical error calculated on the curve is indicated for each point (but not visible). Since IQuEYE can achieve this level of precision, one more step can be done.

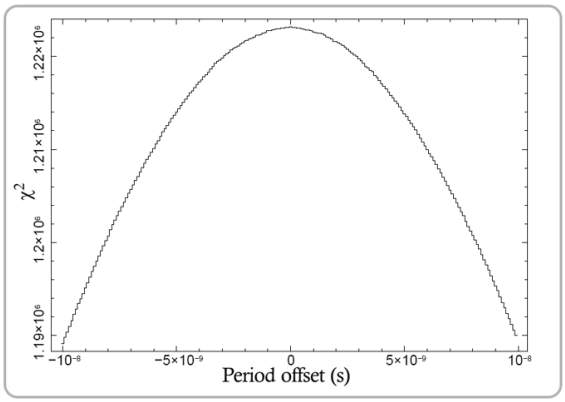

Figure 62: Chi square function for the Crab pulsar. No noise contribution seems to affect the analysis.

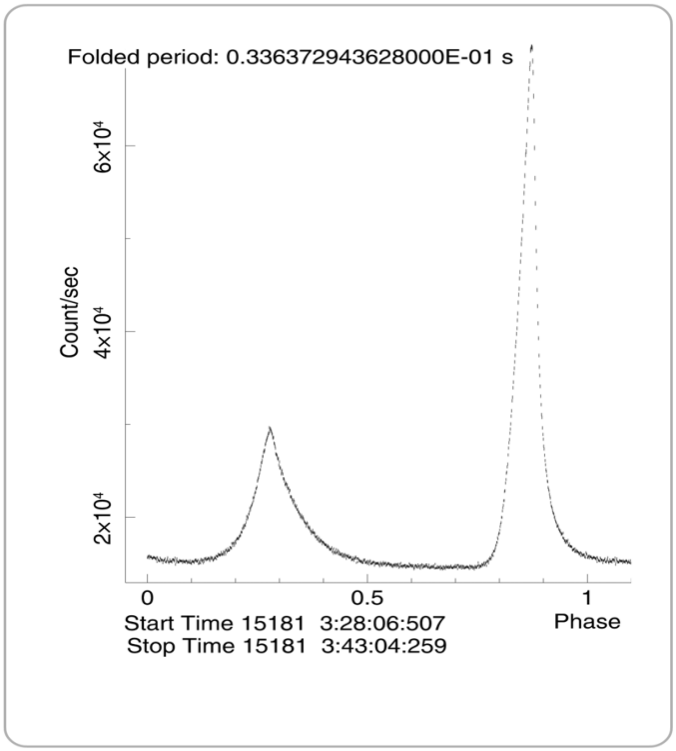

Figure 63: Light curve of Crab pulsar. The curve is obtained folding the data acquired in 15 minutes.

Thanks to the high information content in the higher order harmonics of Fourier Transform, using formula E7, with a 15minutes long acquisition it is possible to reach value of σ~1ns for the estimated error on the period. But the period derivative of the Crab pulsar is about 1.5ns per hour: the accuracy achieved with our instrument in 1h brings errors below the ns limit, and it is, for this reason, comparable to the intrinsic slowdown of the rotational period. Therefore, the phase folding technique presented in §6.1.2 is not sufficient to perform an accurate analysis.

A method more laborious but more precise consists in individuating the phase of a specific feature of the light curve (i.e. the primary peak in our case) and in studying how this phase changes in time.

6.2.2 Phase analysis

This part of the analysis was developed by C.Germanà et al. and for the details the reader is referred to [GER]. Only few results will be reported in these sections sole intended to demonstrate the capability of IQuEYE.

Basically the procedure forecast to build up an analytical approximation $S(\phi)$ of the light curve, a function continuous and periodic with period 1 (in phase units) and differentiable at all expect two points, corresponding to the peaks of the two Crab pulses.

Using standard pulsar analysis one obtain the initial period P_{in} and determine $\phi(t)$, the initial phase of the pulsar as a function of time with respect to the chosen period.

So, $\nu(t) = \frac{d\phi}{dt}$; $\dot{\nu}(t) = \frac{d^2\phi}{dt^2}$.

The phase ψ(t) we are searching for is obtained via a phase function Ψ that represents a sort of convolution between the original pulsar signal W(ϕ (*t*)) expressed in function of the phase, and the derivative *S'* that cross the Y axis in very steep way in a point corresponding to the maximum peak position of *S*. The integration is performed over a short domain (a little integer number *N* of periods, giving typically *NP* ≈ one second or two), this ensure that the pulsar period variation is negligible over the integration domain. The expression of Ψ is:

$$\Psi(t_0, \psi) = \int_{t_0 - NP_{in}}^{t_0 + NP_{in}} W\big(\phi(t)\big) S'\left(\frac{t}{P_{in}} + \psi\right) dt$$

The spin down of the pulsar can be written in terms of the frequency:

$$\psi(t) = (\nu - \nu_0)t + \frac{1}{2}\dot{\nu}t^2 + \frac{1}{6}\ddot{\nu}t^3 \qquad \text{E8}$$

Where ν_0 is the frequency at zero epoch t_0, ν is the rotational frequency and the dots indicate the first and second derivative.

The behavior of ψ is approximate by a parabola, since the term in $\ddot{\nu}$ is negligible; from the behavior of the observed phase one can estimate the rotational period and its derivatives. Moreover, the residuals left out after fitting this model could provide a way for finding unknown features of the source.

This procedure was applied to the data acquired in January and December 2009.

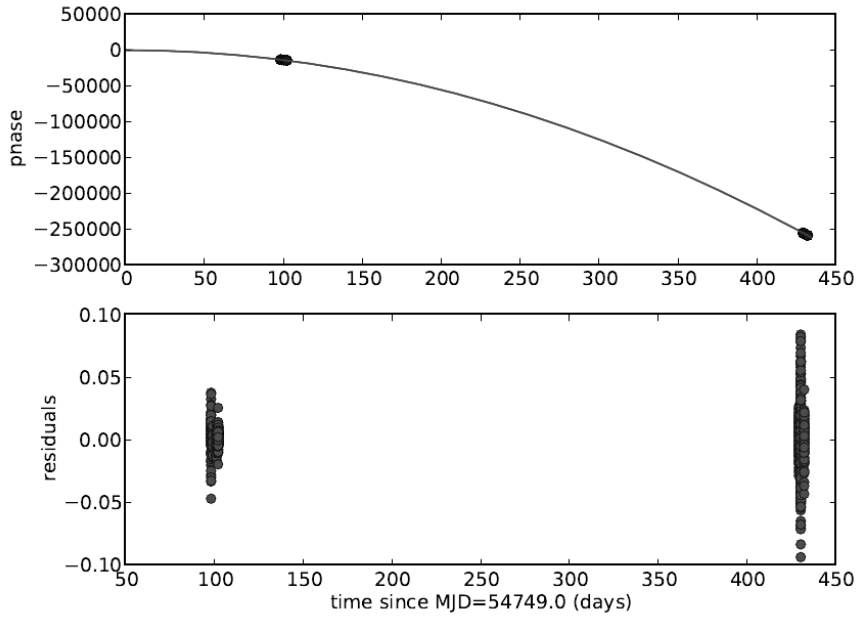

Figure 64: Phase-connection between January and December 2009 runs. The symmetry of the residuals after the parabola subtraction, shows the IQuEYE capability in measuring with high accuracy the phase of the pulsar.

The phase of the Crab pulsar was calculated at each 2s long integration time interval. From the phase behavior in time we calculated rotational periods in January and December, with a Poissonian statistical error of the order of $10^{-14}s$ for the January data and $10^{-13}s$ for December data. A log of the observation, listing the rotational periods at each starting observation epoch is shown in Table 7.

The frequency derivative gives value around $\dot{\nu} \approx -3.7 \cdot 10^{-10}s^{-2}$ with an error $\approx 2.6 \cdot 10^{-16}s^{-2}$ and the data spanned over a one year long period allows the estimate of the second derivative $\ddot{\nu} \approx 1.5 \cdot 10^{-20}\ s^{-3}$.

Last column in Table 7 (JB ref.) contains the data derived from Crab Pulsar Monthly Ephemeris released by Jodrell Bank Centre for Astrophysics: in order to have a benchmark for the goodness of our data (lack of bias, systematics etc.) they were compared with those, as described in next subsection.

Table 7: Log of the observation of the Crab pulsar and period calculated. Last column indicates the period obtained by Jodrell Bank data. Both are baycentrized with Tempo1 to avoid problems due to software difference.

Date	MJD (d)	Duration (s)	Period (s)	JB Ref. (s)
January 16 01:55:33	54847.08587011805557	1197	0.03362516470042	0.03362516469808
January 16 02:31:07	54847.11459567151620	1797	0.03362516574368	0.03362516574136
January 17 01:22:18	54848.06272740807870	3597	0.03362520017813	0.03362520017654
January 19 00:48:19	54850.03901748245370	3597	0.03362527195367	0.03362527195304
January 20 01:28:31	54851.07300875886574	3712	0.03362530950662	0.03362530950632
December 13 03:51:16	55178.16707177530092	1792	0.0336371877769	0.0336371877689
December 14 02:36:51	55179.11539707857639	2602	0.0336372222108	0.0336372222034
December 14 04:40:15	55179.20109179855324	2596	0.0336372253224	0.0336372253150
9 December 15 03:20:17	55180.14556120746528	2570	0.0336372596163	0.0336372596096
10 December 16 02:18:16	55181.10249429464120	1922	0.0336372943628	0.0336372943567
11 December 16 03:18:48	55181.10249429464120	892	0.0336372958892	0.0336372958831

6.2.3 Jodrell Bank

Jodrell Bank Centre for Astrophysics [*jba*] releases Crab Pulsar Monthly Ephemeris containing the dispersion-corrected time of arrival of the center of the main pulse (in TDB time system), the frequency and its first derivative and the range of validity

First comparative analyses gave a discrepancy between JB calculated phase and IQuEYE data. The phase calculated from IQuEYE data gives

a period that are systematically 0.9 ns longer than those reported in the JB ephemerides; value completely outside the estimated error. This means that the function $\psi(t)$ measured does not match the one from JB radio ephemerides.

After a long search, the reason for this difference was found in the difference between the barycentrization procedures used for JB and IQuEYE data. As anticipated, JB data were barycenrized with Tempo1. In Tempo1 the events are referred to Barycentric Dynamical Time (TDB). Instead Tempo2 refers the ToAs to Barycentric Coordinate Time (TCB), the two Times have a little difference consisting in the time dilation due to the earth potential pit on the Geoid surface; using TDB leads to a loss of about $1.55 \cdot 10^{-8}\ s\backslash s$ (see [IRW]).

This accounts for only half of the found error. Other 0.5ns is explained by a difference in Roemer delay model between Tempo1 and Tempo2: the first does not correct the ToAs for the Earth polar motion. Moreover, Tempo1 is based on out-of-date precession/nutation model. If the IQuEYE ToAs is barycentrized with Tempo1, the differences between the periods is reduced to value of the order of few picoseconds.

In Figure 65 the behavior of the Crab pulsar main peak phase drift is shown. The dark points indicate the value of the phases calculated for December 2009 run. The curve superimposed (labeled NTT) is the best-fitting parabola (as obtained in equation E8 on page 97). The curve marked with JB is the Jodrell Bank radio ephemerides parabola.

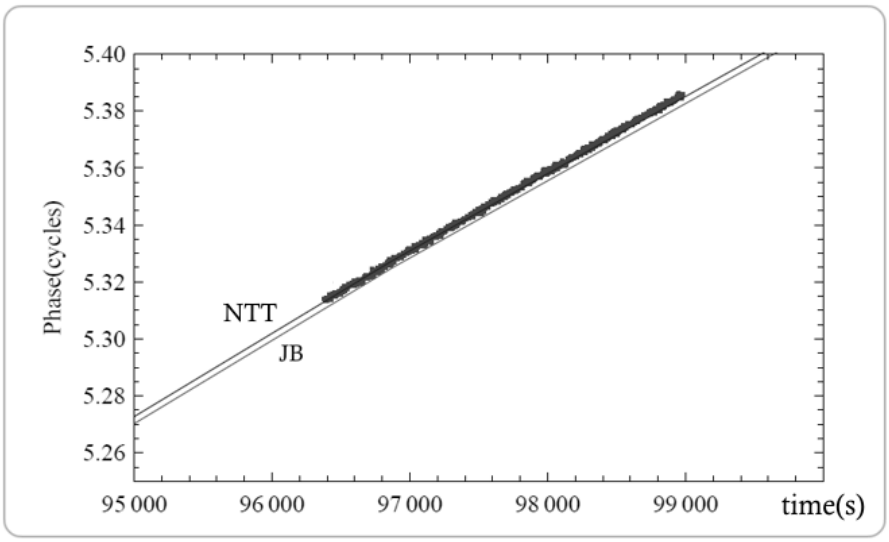

Figure 65:difference in phase between IQuEYE data and Jodrell Bank ephemeris.

Discrepancies with the Jodrell Bank radio ephemeris, over the two runs, are included in a range that varies from 0.3 to 8 picoseconds. The estimated statistical error on NTT data is $\sim 7 \cdot 10^{-14}$ s, and the error on Jodrell Bank data is $1.8 \cdot 10^{-13}$ s. Therefore the difference exceeds the errors dozens of times.

At this level of precision, however, the residual discrepancy cannot be attributed with certainty to the instrument.

Several authors, in fact, reports observation indicating the presence of a not yet explained noise component in ms pulsars phase behavior, see for ex. [LYN], [SCO], [CA1], [CA2] or [PAT]. This means, in practice, the existence of not-modelized effects that make the behavior of the phase differ slightly from that described by equation E8. One hypothesis advanced is that the varying dispersion measure affects the phase behavior: in such a way the radio phase derived from the JB archive ephemeris would be slightly different than the actual one and, therefore, the radio-optical phase drifts leading to rotational periods a few ps longer, might be caused by a "real" extra-noise component.

In conclusion, the data analyzed demonstrate the capabilities of IQuEYE: the instrument, in fact, is able to detect the timing difference induced by the bad modeled Earth polar motion or by the gravitational effects on the Geoid. Beyond these problems, however, the phase analysis can be pushed down to error for the periods of the order of picoseconds, to match those calculated from JB ephemeris. The residual differences do not indicate an error plausibly linked to the instrument. The signal from the Crab pulsar as collected by IQuEYE may be affected by some unknown noise component. To reach a decision on these issues, additional information is needed and future observations will make us able to understand the phenomenon.

6.3 LMC Pulsar

B0540-69 is a 50ms optical pulsar, the second brighter in the sky and it is located in the Large Magellanic Cloud. We have observed the LMC pulsar with IQuEYE during the two NTT observation campaigns during January and December 2009. The obtained data have unparalleled timing accuracy and provide the most detailed optical light curve available so far for this pulsar. The observations were performed using the two 3.5 or 5.2 arcsec pin-holes, without filters (for the q.e. of the instrument see § 2.3).

The spectra of the data present frequency peaks over 20σ out of the noise, at the expected values (19.7433 Hz in January and 19.7380 Hz in December); no other signal was visible above 3σ of noise in the range 0-200 Hz. The arrival times of the photons are corrected to the barycenter of the solar system, as depicted in § 6.1.1, assuming the celestial coordinates of the target equal to

RA2000 = 05h40m11s.202 ± 0s.009;
DEC2000 = –69°19'54''.17 ± 0''.05

with zero proper motion, as in [MIG].

In order to determine the period with the highest possible accuracy we scan a 3μs window around the period obtained through the FFT in steps of 0.1ns by means of the phase-folding technique exposed in § 6.1.2. The best period P obtained in each observation night is shown in Table 8.

For each period a well defined $\chi^2(P)$ distribution, peaked around the expected value, is obtained and the best value for the periods is then de-

duced by considering the maximum of the Gaussian fit of the distribution, with the error associated using the formula E7.

Table 8: Periods and frequencies of the LMC pulsar determined with IQuEYE data obtained during Jan. and Dec. 2009. The column PH indicate the pin-hole dimension used.

Date	MJD (d)	PH (")	Obs. Length (s)	Period (s)	Error ($s \times 10^{-9}$)
2009 01 18	54849.21665	3.5	5994	0.050 649 974 5	43.8
2009 01 20	54851.16190	5.2	5874	0.050 650 017 3	23.8
2009 12 14	55179.31111	3.5	3600	0.050 663 549 8	44.4
2009 12 15	55180.11250	3.5	3600	0.050 663 632 9	25.4
2009 12 16	55181.06944	5.2	3000	0.050 663 671 5	49.1
2009 12 18	55183.10417	3.5	3600	0.050 663 753 2	24.3

The combined IQuEYE light curve for all nights of January and December 2009 is shown in Figure 66 for a 50bins phase subdivision. Given the high number of acquired photons (indicatively, a mean rate of 2500 counts/sec), and the extremely accurate time tagging guaranteed by IQuEYE, the light curve shown in Figure 66 is the best available so far in visible light. The total duration of the main peak is approximately 22ms (FWHM), with a central shallower feature suggesting the superposition of at least two peaks, as already found from X-ray data by De Plaa et al. [DEP].

Moreover, the high quality of the data allows us to determine the first derivative of the LMC pulsar rotation frequency and we obtain

ν_0=19.7379712 ± 4.83 ×10^{-6} Hz

$\dot{\nu}_0$=1.86346 × 10^{-10}±2.65 ×10^{-13} Hz/s.

Where the reference point considered in the fit is t_0=55183.1042 (MJD)

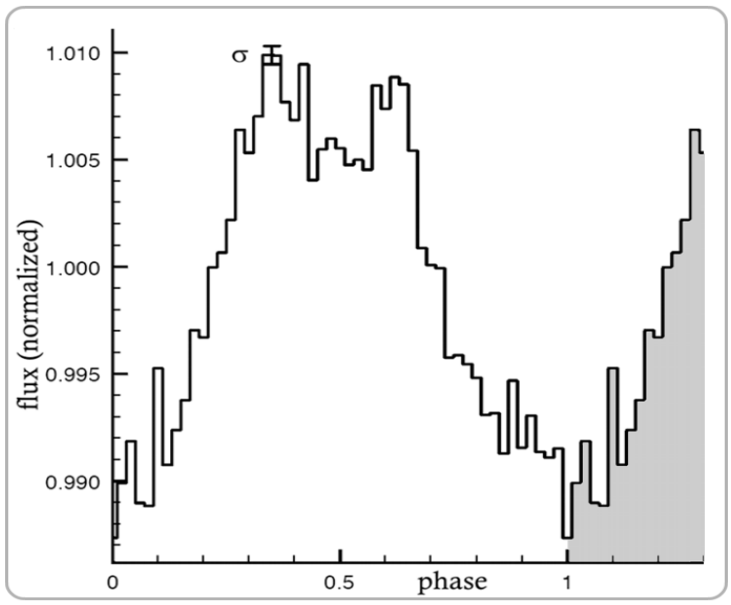

Figure 66: The overall IQuEYE light curve in January2009 and December 2009, from the single light curves weighted according to their respective χ^2 value and binned in 50 phase intervals. The counts have been normalized to the average count value during a period. For clarity the curve is shown over two cycles. The vertical bar shows the 1 sigma error.

6.3.1 Braking Index

The braking index n of a pulsar, which describes the dependence of the braking torque on rotation frequency, is a fundamental parameter of pulsar electrodynamics. It is usally defined as:

$$n = \frac{\nu\ddot{\nu}}{\dot{\nu}^2}$$

so that the variation of the pulsar frequency can be expressed in a simple way as $\dot{\nu} = K\nu^n$ where K is a constant and the dots above the letters indicate, obviously, the first and the second derivative of the frequency. The braking index is strictly related with the pulsar spin-down mechanism and, typically, it is assumed that magnetic dipole radiation mechanism plays the main role in the loss of rotational energy. For this kind of models one can obtain a theoretical result giving n=3 (see for ex [MA1]). Different values of n indicate the presence of other processes underlying the spin-down mechanism; in particular, values lower than 3 indicate that an additional torque is contributing to the dipole radiation, for example the loss of relativistic particles or gravitational radiation or quadrupole magnetic radiation. Also the distortion of the magnetic dipole geometry, a time variable magnetic field, a change with time of the inclination angle between rotation and magnetic axes and the presence of particles or currents in the magnetosphere have been proposed as additional contributions ([GHO],[LIV]). At present the braking index has been measured for only few pulsars (typically the younger ones with rapid spin-down and few glitches) and, in particular, for the LMC pulsar some incompatible values of n are reported in the literature (see Table 9).

Our results is calculated by adding the frequency values measured with IQuEYE in January and December 2009 to the previously published data sets covering the entire spectrum from radio to X-ray. For further details see [IQ2]. Than these values is simply fitted with a second order polynomial fit

$$\nu(t) = \nu(t_0) + \dot{\nu}(t - t_0) + \tfrac{1}{2}\ddot{\nu}(t - t_0)^2$$

where t_0 is still our last observation date. The resulting value for the braking index obtained from the fit is

$$n = 2.087 \pm 0.007.$$

Our result is consistent within 3 combined σ with the value calculated by Manchester et al. in [MA2] and Gouiffes et al. in [GOU].

Table 9: Braking Index calculated by various autors**.**

n	*σ*	band	year	Ref.
2.140	± 0.009	X	2005	Livingstone et al. [LIV]
2.01	±0.02	opt	1989	Manchester et al. [MA2]
2.04	±0.02	opt	1992	Gouiffes et al. [GOU]
2.28	±0.02	opt	1995	Boyd et al. [BOY]
2.087	**± 0.007**	**all**	**2010**	**IQuEYE [IQ2]**

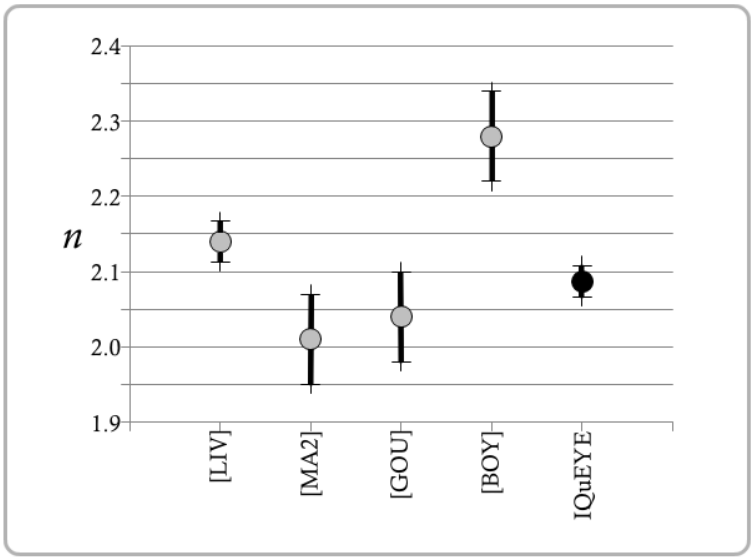

Figure 67: Braking index as calculated by various authors. The vertical lines indicates the 3σ errors.

6.4 Vela pulsar

6.4.1 introduction.

To conclude this chapter we go forward with the third pulsar observed, PSR B0833-45, the Vela pulsar. Although it is the third most luminous optical pulsars in the sky (V=23.6), it is almost at the visibility limit for NTT. It is clear that in this case the extraction of signal from noise is an operation that is more difficult than in the cases treated in the previous sections, because the signal is overwhelmed by the noise. Even the pointing operations at the telescope are made more difficult by the weakness of the signal; in fact the impossibility of distinguishing the source directly with the camera field implies the need for an offset centering procedure. But beyond the technical difficulties, also in the data analysis the difficulties grow: the Fourier transform itself is a tool of little help, an example of the FFT of the signal for a 60 minutes-long observation was seen in Figure 59 and did not show particularly significant peaks around the expected frequency. Before one can see at least one component in the spectrum of the signal it is necessary to extend the observation to 180 minutes: in Figure 68 a peak at about 11Hz, which stands barely from the background, is noticeable.

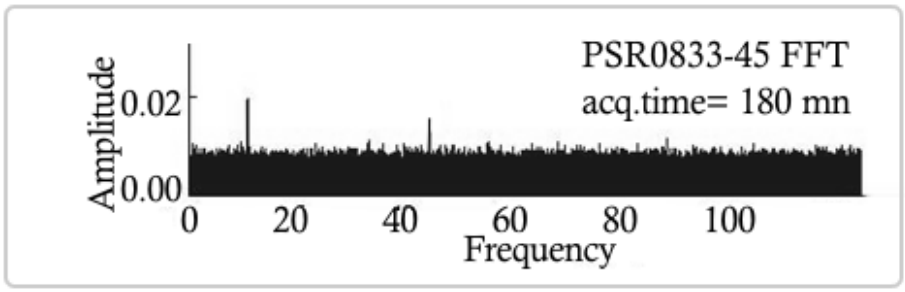

Figure 68: FFT obtained on an acquisition 180minutes long performed observing the Vela pulsar.

Whereas the poor results obtained with standard tools seen in § 6.1.2 in the analysis of the Vela pulsar we have chosen a different approach: in [BEA] the Karhunen-Loève transform (KLT) is used as a tool for denoising a signal totally immersed in noise. The field of research and the nature of the data used in the article are completely different from those in this thesis, but the paper has still provided a basic idea to follow. These paragraphs summarize an attempt to perform a KLT analysis to the Vela pulsar data: the tools we implemented are not yet wholly developed, but some interesting results were found.

Actually the direct approach has proved difficult to be implemented because of the excessive computational resources needed to apply the KLT in its most straight formulation to the large amount of data collected. The best results are obtained with a derivation of the KLT developed and used mostly for the analysis and/or compression of images and study of statistics, the so-called Principal Component Analysis (PCA).

6.4.2 ***New analysis tools***

The mathematical theory underlying the KLT is quite complicated and it is not described here. For further details see [COD] and [MAC]. In this section, however, we will simply present the basic idea of the KLT and some attempts to apply it to the acquired data with IQuEYE.

The concept behind the KLT can be summarized in a suitable transformation of the coordinate axes, with respect to which the vector (signal) was acquired, highlighting the periodic components. This means that through the KL series expansion of a signal affected by noise and a subsequent analysis of the eigenfunctions associated with a dominant eigenvalue (or, more generally, a few dominant eigenvalues), it would be possible to obtain a detection of the coherent part of the signal, and even more, its reconstruction.

The algorithm for KLT performs the autocorrelation of the signal and uses it to build an array.

Considering input vectors of at least 10^6 elements, the matrix on which the algorithm work has at least 10^{12} elements (64 bits double precision floating points each). Storage space needed in memory to hold the entire matrix becomes, at the best, 2^{46} bits, more than 7TB, but exceeding one hundred TB for longer acquisitions or denser binning.

In practice the data analyzed by the direct version of the KLT are limited to pieces few seconds long, giving better results than the FFT, if applied to acquisition of comparable lengths. But ultimately, it is true that, from a "mathematical" point of view, the KLT is a very promising tool: Figure 69 shows a comparison between the two transforms. The test signal is a sine wave of frequency 300Hz "dirtied" by a white Gaussian noise, sampled at 1kHz for 5 seconds, in which the signal to noise ratio is 0.005. Panel A shows a simple FFT of the signal, and the peak at 300Hz is hardly visible, while the second panel shows the FFT of the first component of the KL series expansion, that is the projection of the signal on the dominant eigenvector. The spectrum of the first KL component is essentially the sinusoidal part of the original signal, as evidenced by the extremely well-defined peak.

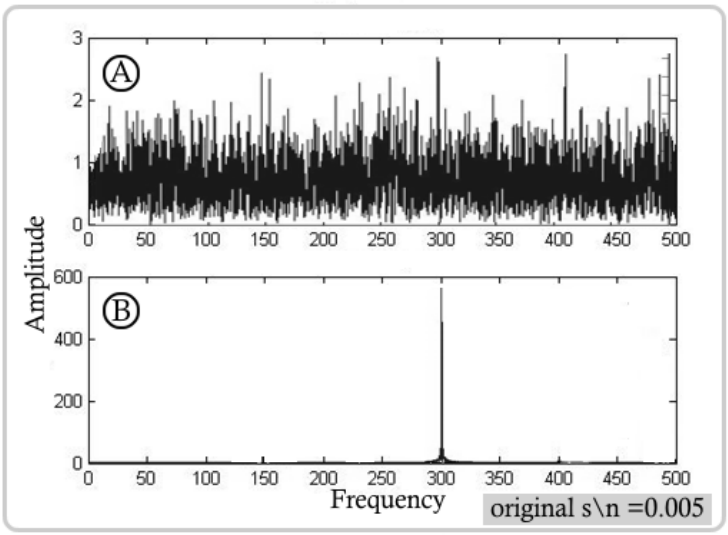

Figure 69: Comparison between FFT (panel A) and KLT (panel B) for a signal having snr=0.005. (see text for the details)

At present the benefits obtained are certainly overshadowed by the burden of the computational request. In other words the amount of data to which the KLT can be applied (or at least the version we developed!) makes the usual Fourier transform (Fast Fourier Transform) able to recover the gap and, indeed, get better results simply because it is applicable in far less time to a signal that is some order of magnitude longer.

6.4.3 **Waterfalls**

It is useful to introduce the waterfall diagrams because we handle them in the next subsection. The waterfall diagrams are sometimes used in the standard analysis too, to refine the determination of the initial pulse period or to get an idea of the variation of the period in time.

Let's consider the signal vector opportunely binned, $X=(x_1 \ldots x_N)$ and let's divide X in various subintervals of equal length containing a number p of periods P each. Considering each of these subintervals as a single short acquisition, one can build a folded light curves for each subinterval (the length of which varies depending on the signal considered and may

range from some periods to several minutes) and produce in this way p vectors of q elements each: ($z_{1,1}$ ... $z_{1,q}$) ... ($z_{p,1}$...$z_{p,q}$) where, precisely, q is the number of bins per period and p is the number of light curves in which the original signal X was divided. The vectors obtained in this way can be tabulated in a matrix of size p × q, which can be displayed as an image by assigning to the values $z_{i,j}$ a chromatic scale varying between z_{min} and z_{max}.

The resulting image represents a time sequence (along the lines) of short folding, a waterfall made of light curves.

To give an example, the Figure 70 shows two waterfalls obtained, with an arbitrary grayscale indicated in the lower left corner, for an acquisition 500s long of the Crab pulsar. The time-bin used is 0.1ms and every subinterval (the rows) is obtained by folding 1s of signal (that means p=500 and q≈330). In the panel A the period used for folding is approximately correct, then all the light curves are in phase and the emission peaks produce the image of a vertical line. On the contrary, the initial period used in the panel B is slightly too short, this causes a drift of the light curves on the right.

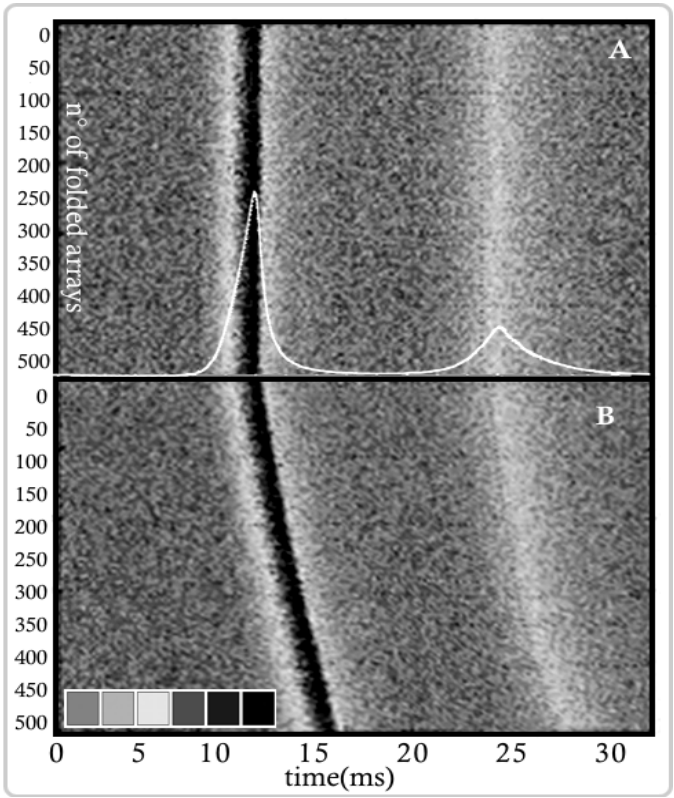

Figure 70: Waterfall diagrams obtained for the Crab pulsar signal. The total length of acquisition is 500s, the time bin is 0.1ms and the subintervals are 1s long. The panel A shows the diagram performed with the right period, instead in the panel B a period too short is used. The white lightcurve superimposed on top panel indicate the meaning of the plot.

6.4.4 PCA

The basic idea of the Principal Component Analysis (PCA) is to reduce the dimension of the data set in which there are a large number of related variables, keeping as much variance as possible in the data. This is achieved through a linear transformation of the variables that projects the original ones in a new Cartesian frame in which the variables are sorted in descending order of variance: therefore, the variable with greater variance is projected onto the first axis, and so on. Unlike other possible linear transformations, in this case the data itself determine the transformation vectors. Although the basic idea is similar to that of pure KLT and also to that described in § 6.1.2 regarding the method of identifying the optimal period through the maximization of χ^2, PCA operates on matrix of data (henceforth called images).

The original idea was to apply the PCA to the waterfall diagrams described above.

Again we search for the best period to fold the data, and once again we do it maximizing a quantity indicative of the maximum variance in the data as a function of the independent variable *P*. In this case this quantity is the percentage of signal reconstructed using only the first principal components, i.e. how much the signal can be "summarized" by the projection of the signal on the first new basis vectors.

The mathematical processes behind the PCA will not be discussed here; the reader may consult [COD] or [HYV] for a detailed description. Here, however, a qualitative introduction is given in order to allow the reader to understand how the PCA could be applied to our data.

The data under analysis are labeled in the waterfall diagram $Z = z_{ij}$ having size $p \times q$, and can be considered, from a certain point of view, as a sequence of measures of the same variable: the rows, in fact, are repeated measures of the same phenomenon (i.e. the emission of the pulsar folded on few periods).

A way to understand how the rows vary together or how a row is related to each other, is calculating the covariance matrix $C_Z = ZZ^T$ that is a symmetric matrix $p \times p$ in which the values placed on the diagonal correspond to the single row variance and the values outside the diagonal correspond to the covariance between the row. In order to maximize the variance in directions containing relevant information, represented by the diagonal of the matrix C_Z, and to minimize data redundancy and noise, represented by the covariance in the non-diagonal elements, the covariance matrix C_Z can be written in diagonal form with a suitable change of reference system: $V^{-1} C_Z V = D$

So D is a $p \times p$ diagonal matrix containing the eigenvalues of C_Z and V is another $p \times p$ matrix where each column is an eigenvector of C_Z. The j-th column of V is the eigenvector associated with eigenvalue D_{jj}.

The new reference system corresponds to the eigenvectors of the covariance matrix and the new variables are no longer measured data (let's say observable quantity, the subject of measurements) but linear combinations of them. Those new variables are called Principal Components (PC)

and the procedures for calculation and interpretation of the PC is called principal component analysis. The purpose of PCA is the representation of a data set with non-diagonal covariance matrix of size p × p in a space in which the same data is represented by a diagonal covariance matrix, but with dimension smaller than p × p. This is obtained by taking only the more "representative" projections (this process can be considered as a compression of the data). The collateral effect in this procedure is to reject the portion of data containing the noise and to retain the portion containing the signal. So the diagonalization is achieved with a rotation of the coordinates in the base of eigenvectors; each eigenvector has an associated eigenvalue corresponding to the variance of its principal component. If the original variables are partially related to each other (as in our case), some eigenvalue has a negligible value and the corresponding eigenvector may be neglected, so the data representation can be limited to eigenvectors with larger eigenvalues. Since the covariance matrix in the base of the principal components is diagonal, the variance is the sum of the variances of each principal component.

If one is interested in a good signal reconstruction it is therefore necessary to have a decisional criterion to select which PCs are to be kept or discarded. Once normalized the total sum of the eigenvalues λ_j to the sum of all the eigenvalues, a typical criterion is to retain the first h (which, as they are sorted in descending order, are the largest ones), determined by a chosen value k, that is the variance threshold to be reached. For example, if k=0.9, h is such that $\sum_{j=1}^{h} \lambda_j \geq 0.9$, which indicates that 90% of the information contained in the waterfall diagram can be represented using the first h principal components.

But in our case we are not interested in the reconstruction of the signal (pulsar+noise) but in the extraction of the pulsar signal alone. Again, the initial folding period can be varied and, therefore, the final variance expressed by the eigenvalues λ_1 becomes, once again, a function of *P*. The variance increases when all the periods composing each subinterval are in phase, so an analysis for understanding which period can maximize the eigenvalue related to the part of the signal represented by the first PC, leads to the correct period. Figure 71 is intended only for illustrative purpose and concerns the PCA applied to a waterfall of the Crab pulsar obtained from a short observation performed in December 2009 where the subinterval considered for the row-folding is about 1s long. It depicts the results obtained from a scan of the period with steps of 100ns in a window around the rotation period indicated by the FFT. The value plotted is the variance of the first PC (normalized to the total variance, i.e. the sum of all eigenvalues) in function of *P*. It is clearly visible that, as *P* approaches a certain value, the variance of the first PC dramatically increases until it reaches the maximum value of 0.8, which means, in a nutshell, that 80% of the information contained in the Crab pulsar waterfall diagram can be reproduced using only the first PC.

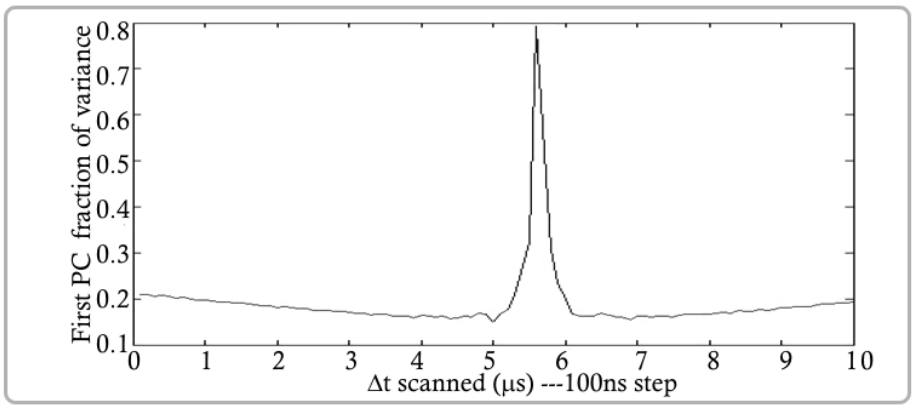

Figure 71: Normalized Eigenvalue for the First PC in function of the period variations. The X axis shows a window of 10μs around the value obtained through the Fourier transform.

Clearly, in the case of the Crab pulsar some information about the light curve and the optimal period can be obtained directly from the waterfall diagram (see the example in Figure 70). In the Vela pulsar case, however, the diagram shows absolutely no features, and does not provide specific information, as can be clearly seen in Figure 72. In this case one PC is not enough to obtain a good level of the variance, but, however it is enough to try to maximize the first PC variance.

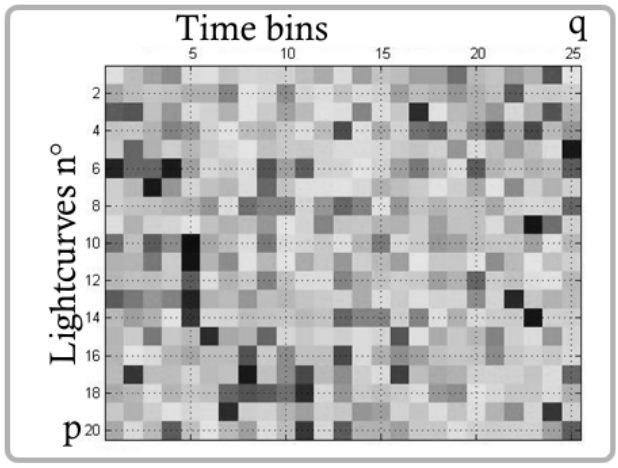

Figure 72: A waterfall diagram for the signal acquired from the Vela pulsar. No features are recognizable.

6.4.5 Results

The algorithm we implemented for the PCA was applied to the best set of data from Vela pulsar acquired in December 2009. The observation is 180 minutes long and it was performed through the 5.2arcsec pin-hole. A raw scan of period around the value suggested by the FFT was carried out on the first PC in steps of 100ns, and then other scans were performed with increasingly fine resolution. Figure 74 shows the eigenvalue λ_1 related to the first principal component (normalized to the eigenvalues sum) in function of the period *P*. The coarse scan is performed in a window ten

microseconds long, while in the panel at the top right, a fine scan with 0.1ns steps adds details to the peak obtained in the first one.

In this way the best period determination is achieved by applying the PCA to a waterfall of 20 rows. The $\lambda_1(P)$ maximum is selected fitting with a Gaussian curve the distribution and is:

Table 10: Vela pulsar period. The question mark near the error indicate that the method implemented for finding the error with for the PCA is still under investigation (see text)

Period	**0.0893669875s ± 50(?)ns**
Date	2009 12 18
Starting time	04:26:50 UTC
Total acquisition time	10080 s

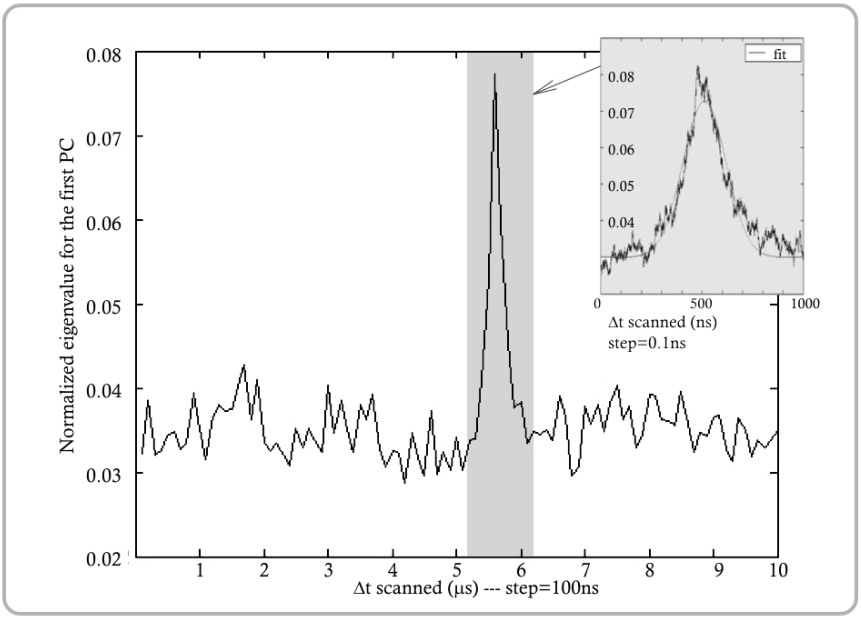

Figure 73: Normalized Eigenvalue for the First PC in function of the period variations. The X axis shows a window of 10ms around the value obtained through the Fourier transform. The gray panel on right side shows a scan performed with step of 0.1ns and a Gaussian curve fitting the curve.

In the implemented method, it is not yet clear how we can give a reliable estimate of the error. The error listed in Table 10 has been calculated simply by considering the standard deviation of the curve $\lambda_1(P)$ compared to the peak of the Gaussian fit shown. This should indicate a plausible estimate of how the noise may have affected the correct maximum position of the curve $\lambda_1(P)$, but a more accurate procedure is still developing.

The found value of P allowed a reconstruction of the light curve over the entire signal; the results are summarized in Figure 74, where the panels A and B show two light curves obtained by Wallace et al. [WAL] more than 30 years ago, the only ones available in the literature.

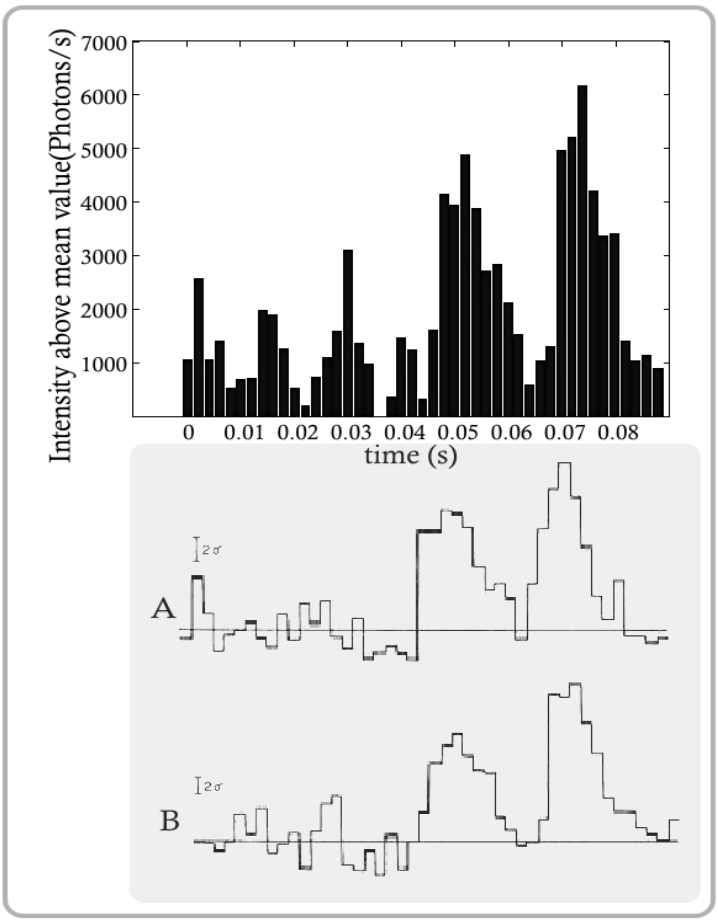

Figure 74: Vela lightcurve obtained folding a detected signal 180 minutes long with the Period calculated through the PCA. The curves on bottom are those obtained by Wallace et al. in 1977 (A) and 1979 (B).

7 Conclusions

The very fast photon counting photometer IQuEYE was built and successfully used at NTT in three observation campaigns. The instrument permits hours of uninterrupted observation with timing accuracy superior to 100ps (and 500ps if referred to UTC).

Some of the achievements have been discussed in the second part of the thesis and some conclusions have been outlined in the respective chapters. The three categories of observed objects refer to three different time domains.

In §.5 we investigate the observation of sources with variations on relatively long time scales (unless the study of planetary atmospheres through the effects of atmospheric lens is considered). In this field, probably, the timing capability of the instrument is actually oversized. The single photon counting solution certainly improves the time resolution in the analysis of transit (and these considerations are equally valid in the case of objects observed with variations on long time scales, which were not presented here for brevity), however, some intrinsic characteristics of the instrument balance the timing performance. First, the absence of comparison stars acquired with the same type of detector used for the target makes it difficult a good denoising of the signal, allowing the introduction of spurious components not due to real source fluctuations. Some ideas to bypass the problem were discussed; the implementation (we are speaking about new instruments) of a mobile collector in the FoV that, through an optical fiber, feeds a SPAD, could represent a good solution. Basically it is the equivalent of the IQuEYE sky monitoring SPAD (see §3.1.1) implemented with improvements introduced after the first run at NTT, but with the ability to be electronically moved on a reference object. This involves a different field monitoring and pointing systems (shiftable field mirror etc).

The second problem is instead related to the instrument intrinsic structure and is more difficult to eliminate. In fact, IQuEYE remains a non-imaging single pixel instrument and its field of view is however confined. This causes the impossibility of identifying the spatial fluctuations of the source or any spread caused by excessive atmospheric fluctuations. Moreover in case of sources close to the target, the noise contribution entering the pin-hole is not discernible from the real signal or, if the FoV is limited to avoid this problem, signal loss and seeing interferences with the edge of the diaphragm affect the acquisition. Not even the design of QuantEYE avoids these problems, because, however, it is not an imaging instrument.

At present there is no SPADs array (or so rapid and sensitive sensors) available, because the problems discussed and clearly highlighted in (§ 3.2.1). A total change of the optical design architecture would provide the

imaging capability, for example through the introduction of a sparse array of sensors fed by an array of microlenses, but this solution drastically lower performance in terms of quantum efficiency and eliminates the possibility of multi-channel photometry. Furthermore it does not allow the subdivision of the telescope pupil, required to make the HBTII (for example between the various sub-pupils of the EELT).

However, a final evaluation on the actual improvements carried by an IQuEYE-like instrument in the field of non-extremely rapid variations will be made when the definitive analysis of data collected during last campaign will performed. For the moment we can conclude that the observations have demonstrated the great versatility of the instrument, allowing the analysis of the source with accuracy at least comparable to that of common instruments in use.

In §.4 a first approach to Quantum Astronomy was dealt. The small size of the telescope does not allow us to obtain real results; nevertheless, as we have seen, the analyses carried out pave the way for the implementation of similar instruments designed for larger telescopes and demonstrate that the QuantEYE goals could be reached.

In §.6, instead, rapidly varying objects are treated. The results have already been discussed. It can be concluded from the analyses proposed that the single photon counting solution represents a real push forward in the field of the high time resolution astronomy (HTRA) and can be an useful tool for advancement in scientific knowledge of the phenomena involving extremely fast variability; in fact many topics in this field are not yet well understood, as, for example, white dwarfs surface convection, variability near black holes, non-radial oscillations and surface structures on neutron-stars, free-electron lasers and so on, the list could be lengthened at will.

The excellent performances of IQuEYE in this area derive from a combination of many factors: very precise timing of each incoming photon, low dark noise, no read out noise, very wide dynamic range and good quantum efficiency. IQuEYE provides the best determination of photon arrival times than any other current astronomical instrument. So we can safely say that IQuEYE-like instruments mounted at NTT-size telescopes represent an innovative tool capable of providing excellent scientific results without the need for larger telescopes.

To get an idea of the performance in comparison with the actual astronomical landscape, the Table 11 shows the timing resolution performance of some of the best instruments existing or under development.

Table 11: Current detector types showing time resolution, and quantum efficiency. Table adapted from [HTR].

Detector type	t res.	Q.E.	Instrument
CCD	5ms	0.9	Many
EMCCD	+ms	0.15	Ultraspec GASP
pnCCD	10ns	0.9	XrayCCD
SPAD	+ns +ns **100ps**	0.8 0.15 **0.5**	Optima GASP **IQuEYE**
STJ	+ns	0.9	SCAM
PhotoCatodes	+ns ms	<0.3 0.4	Many

EMCCD: Electron Multiplying CCD
STJ:Superconducting Tunnel Junctions

The next crucial goal is the construction of two single photon counters, conceptually similar to IQuEYE, for larger telescopes (VLTs) where a real approach to quantum astronomy is feasible. So we proposed to realize a "Twin Advanced IQuEYE" (TAI), that is a couple of upgraded versions of IQuEYE, able to time-tag up to 80 million events per second with an absolute (UTC) time accuracy better than 50 ps, that is 10 times better than IQuEYE.

This instrument would represent the last fundamental step along the road towards Quantum Astronomy with the E-ELT

Bibliography

Note: publications referred in this thesis and (co)-authored by E.V. are labeled by [IQ#] and are indicated in bold characters.

[AND] Anderson et al. *Observation of Bose-Einstein condensation in a dilute atomic vapor below 200 nanokelvins* Science 269 198 – 201 (1995)

[ARE] F. T. Arecchi, E. Gatti and A. Sona. *Time distribution of photons from coherent and Gaussian sources*. Physics Letters, 20(1):27–29, (1966).

[BAK] Backer, D. C., Hama, S., van Hook, S., & Foster, R. S. 1993, ApJ, 404, 636

[BEA] Bean, Ralston, Snow, *Evidence for observation of virtual radio Cherenkov fields,* Nuclear Instruments and Methods in Physics Research A, Vol 595, (2008)

[BEC] W. Becker, "Advanced Time-Correlated Single Photon Counting Techniques" Berlin: Springer (2005)

[BIL] Billotta et al. *Quantum Efficiency of Single Photon Avalanche Diode (SPAD),* Mem. S.A.It. Suppl. Vol. 9, 433 (2006)

[BOI] Boiko, D., Gunther, N., Brauer, N., et al., New J. Phys., 11, 013001 (2009)

[BOY] Boyd et al. *High-Speed Photometer Observations of the LMC Pulsar B0540-69* ApJ,448, 365 (1995)

[BRO] R. Brouri, A. Beveratos, J.P. Poizat, and P. Grangier, *Photon antibunching in the fluorescence of individual color centers in diamond,* Optics Letters, Vol. 25, Issue 17, pp. 1294-1296 (2000)

[CA1] Čadež, A. & Galičič, M., A&A 306, 443 (1996)

[CA2] Čadež, A. & Galičič, M., Calvani, M. A&A, 324, 1005, (1997)

[COD] Giacomo Paolo Codogno, *Analisi dell'applicazione della trasformata di Karhunen-Loève a segnali da pulsar ottiche.* Master Thesis (2010).

[COV] Cova, S., Ghioni, M., Lotito, A., Rech, I., & Zappa, F., J. Mod.Opt., 51, 1267 (2004).

[DEP] De Plaa J., Kuiper L., Hermsen W., A&A, 400, 1013-1019 (2003).

[DR1] D. Dravins, et al., Proc. of the Instrumentation for Extremely Large Telescopes workshop, MPIA Heidelberg Spec. Publ. 106, pp. 85-92 (2005)

[DR2] D.Dravins, C.Germanà, *Photon Correlation Spectroscopy for Observing Natural Lasers* in D.Phelan, O.Ryan & A.Shearer, eds., "The Universe at sub-second timescales", AIP Conference Proceedings (2008)

[DR3] D.Dravins, *Quantum-Optical Signatures of Stimulated Emission* "Eta Carinae and Other Mysterious Stars: The Hidden Opportunities of Emission Spectroscopy", ASP Conf. Proc., Vol.242. San Francisco: Astronomical Society of the Pacific, (2001)

[FOE] Foellmi C. *Intensity interferometry and the second-order correlation function $g^{(2)}$ in astrophysics* A&A 507, 3, (2009)

[GER] Claudio Germanà *Timing studies of compact objects.* PhD Thesis (2010)

[GHO] Ghosh "Rotation and accretion powered pulsars" World Scientific Publishing Co. Pte. Ltd.

[GIL] Gillon et al. *Discovery and characterization of WASP-6b, an inflated sub-Jupiter mass planet transiting a solar-type star* A&A 501, 785-792 (2009).

[GL1] Roy J. Glauber, *Photon Correlations* Phys. Rev. Lett. 10, 84–86 (1963).

[GL2] Roy J. Glauber *Coherent and Incoherent States of the Radiation Field* Phys. Rev. 131, 2766–2788 (1963)

[GL3] Roy J. Glauber *The Quantum Theory of Optical Coherence* Phys. Rev. 130, 2529–2539 (1963)

[GOU] Gouiffes et al. *Rotational parameters of PSR0540-69 as measured at optical wavelengths* ApJ, 394, 581-585 (1992).

[HBD] Hanbury Brown, R., Davis, J., & Allen, L. R. *The angular diameters of 32 stars* Mon. Not. R. Astron. Soc., Vol. 167, p. 121-136 (1974)

[HBR] R. Hanbury Brown, "The intensity interferometer. Its applications to astronomy" London: Taylor & Francis, 1974

[HTR] Shearer et al. *High Time Resolution Astrophysics in the Extremely Large Telescope Era : White Paper*, eprint arXiv:1008.0605.(2010).

[HYV] Hyvärinen, Karhunen, Oja, "Independent Component Analysis" John Wiley & Sons, 2001.

[IQ1] Naletto, Barbieri, Occhipinti, Capraro, Di Paola, Facchinetti, Verroi, Zoccarato. *IQuEYE, a single photon-counting photometer applied to the ESO new technology telescope.* A&A 508, 531–539 (2009)

[IQ2] S. Gradari, M. Barbieri, C. Barbieri, G. Naletto, E. Verroi, T. Occhipinti, P. Zoccarato, C. Germanà, L. Zampieri, A. Possenti. *The optical light curve of the LMC pulsar B0540-69 in 2009* Mon. Not. R. Astron. Soc. 000, 1-7 (2010) [accepted]

[IQ3] L. Zampieri, C. Germanà, C. Barbieri, G. Naletto, A. Čadež, I. Capraro, A. Di Paola, C. Facchinetti, T. Occhipinti, D. Ponikvar, E. Verroi, P. Zoccarato, *The Crab pulsar seen from Asiago – Cima Ekar observatory*, Adv. Space Res. 47, 365-369 (2011).

[IQ4] C. Barbieri, G. Naletto, I. Capraro, T. Occhipinti, E. Verroi, P. Zoccarato, S. Gradari, M. Barbieri, C. Germanà, L. Zampieri, E. Giro, V. Da Deppo, A. Di Paola, C. Facchinetti, P. Bolli, C. Pernechele, S. Billotta, G. Bonanno, M. Belluso, F. Messina, M. Zaccariotto, *IQuEYE, a single photon counting very high speed photometer for the ESO 3.5m NTT*, invited paper in Advanced

Photon Counting Techniques IV, SPIE Proc. 7681, 7681-10 (2010).

[IQ5] I. Capraro, C. Barbieri, G. Naletto, T. Occhipinti, E. Verroi, P. Zoccarato, S. Gradari, *Quantum Astronomy with IQuEYE*, in Quantum Information and Computation VIII, SPIE Proc. 7702, 7702-0M (2010).

[IQ6] G. Naletto, C. Barbieri, E. Verroi, I. Capraro, C. Facchinetti, S. Gradari, T. Occhipinti, P. Zoccarato, V. Da Deppo, *Upgrade of IQuEYE, a novel photon-counting photometer for the ESO New Technology Telescope*, in Ground-based and Airborne Instrumentation for Astronomy III, SPIE Proc. 7735, 7735-45 (2010).

[IQ7] I. Capraro, G. Naletto, C. Barbieri, T. Occhipinti, E. Verroi, P. Zoccarato, A. Di Paola, *A first attempt to intensity interferometry with IQuEYE*, in Proceedings of the Quantum of Quasars Workshop, Proc. of Science, SISSA (2009). Published online at: http://pos.sissa.it/archive/conferences/101/012/QQ09_012.pdf

[IQ8] C. Barbieri, G. Naletto, E. Verroi, C. Facchinetti, T. Occhipinti, A. Di Paola, E. Giro, P. Zoccarato, G. Anzolin, M. D'Onofrio, F. Tamburini, G. Bonanno, S. Billotta, C. Pernechele, P. Bolli, V. Da Deppo, S. Fornasier, *First Results of AQuEYE, a Precursor "Quantum" Instrument for the E-ELT*, in Science with the VLT in the ELT Era, Astrophysics and Space Science Proceedings, pp. 249-253 (2009).

[IQ9] C. Barbieri, G. Naletto, T. Occhipinti, C. Facchinetti, E. Verroi, E. Giro, A. Di Paola, S. Billotta , P. Zoccarato, P. Bolli, F. Tamburini, G. Bonanno , M. D'Onofrio, S. Marchi, G. Anzolin, I. Capraro, F. Messina, M. Belluso , C. Pernechele, M. Zaccariotto, L. Zampieri, V. Da Deppo, S. Fornasier, F. Pedichini, *AQuEYE, a single photon counting photometer for astronomy*, J. Modern Optics 56(2-3), pp. 261-272 (2009).

[IQ10] C. Germanà, L. Zampieri, I. Capraro, C. Facchinetti, G. Naletto, T. Occhipinti, E. Verroi, P. Zoccarato, C. Barbieri, *Crab pulsar observations with AQuEYE*, in Simbol-X: focusing on the hard X-ray universe, Proceedings of the 2nd International Simbol-X Symposium. AIP Conference Proceedings, 1126, 370-372 (2009).

[IQ11] C. Barbieri, G. Naletto, I. Capraro, T. Occhipinti, E. Verroi, P. Zoccarato, C. Facchinetti, C. Germanà, M. Parrozzani, M. Zaccariotto, G. Anzolin, F. Tamburini, A. Di Paola, E. Giro, G. Bonanno, S. Billotta, C. Pernechele, P. Bolli, L. Zampieri, A. Possenti, A. Čadež, *Very fast photon counting photometers for astronomical applications: IQuEYE for the ESO 3.5m New Technology Telescope*, invited paper in Photon Counting Applications, Quantum Optics, Quantum Information Transfer and Processing II, SPIE Proc. 7355, 73550R (2009).

[IQ12] C. Germanà, L. Zampieri, I. Capraro, C. Facchinetti, G. Naletto, T. Occhipinti, E. Verroi, P. Zoccarato, C. Barbieri, *Optical pulsations of the Crab nebula pulsar with AQuEYE*, in Proceeding of Polarimetry days in Rome: Crab status, theory and prospects, Proc. of Science, SISSA (2008). Published online at: http://pos.sissa.it/archive/conferences/078/031/CRAB2008_031.pdf

[IRW] Irwin, A. W. & Fukushima, T. 1999, A&A, 348, 642 (1999)

[JEL] T. Jeltes et al. *Comparison of the Hanbury Brown–Twiss effect for bosons and fermions* Nature 445, 402-405 (2007)

[JOH] S. Johansson and V. S. Letokhov, *Astrophysical lasers operating in optical Fe II lines in stellar ejecta of Eta Carinae*, A&A 428, 497-509 (2004)

[KAL] Kalas et al. *Optical Images of an Exosolar Planet 25 Light-Years from Earth* 322, 5906 pp.1345-1348 (2008)

[KOE] Koen, Donoghue, Pollacco, Charpinet, *The EC14026starsXII. PG1219+534, PG0911+456: successes and new challenges for the Fe driving mechanism* Mon.Not.R.Astron.Soc.305 (1999)

[LAR] Larrson, *Parameter estimation in epoch folding analysis.* A&AS, 117, 197 (1996)

[LE1] Leahy, Elsner, Weisskopf, *On searches for periodic pulsed emission - The Rayleigh test compared to epoch folding.* ApJ, 272, 256, (1983)

[LE2] Leahy, *Searches for pulsed emission - Improved determination of period and amplitude from epoch folding for sinusoidal signals.* A&A, 180, 275 (1987)

[LIV] Livingstone et al. *Long-Term Phase-coherent X-Ray Timing of PSR B0540–69*, ApJ, 633, L1095 (2005)

[LOD] Loudon R. "The Quantum Theory of Light" Oxford University Press; 3rd ed. (2000)

[LOU] B. Lounis et al. *Photon antibunching in single CdSe/ZnS quantum dot fluorescence* Chemical Physics Letters 329 399-404 (2000)

[LYN] Lyne, A. G., Pritchard, R. S., & Graham-Smith, F., MNRAS 265, 1003, (1993)

[MA1] Manchester & Taylor "Pulsars" Freeman, SanFrancisco 1977

[MA2] Manchester et al. *A braking index for PSR 0540-69* ApJ, 342, L23-L25 (1989)

[MAC] C. Maccone, "Telecommunication KLT and Relativity" IPI Press, Colorado, 1994.

[MAD] Madhusudhan and Winn, *Empirical constraints on Trojan companions and orbital eccentricities in 25 transiting exoplanetary systems* ApJ 693 784 (2009)

[MAN] A. G. Manning, S. S. Hodgman, R. G. Dall, M. T. Johnsson, and A. G. Truscott, *The Hanbury Brown-Twiss effect in a pulsed atom laser,* Opt. Express 18, 18712-18719 (2010)

[MI1] Michalet, X., Siegmund, O., Vallerga, J., et al., in Optical Biopsy VI, ed.R. Alfano, & A. Katz, SPIE Proc., 6092, 14 (2006)

[MI2] Michalet, X., Siegmund, O., Vallerga, J., et al. J. Mod. Opt., 54, 239. (2006)

[MIG] Mignani R.P., Sartori A., De Luca A. et al., A&A,1003, 786 (2010)

[MIR] Miller-Ricci et al. *MOST Space-based Photometry of the Transiting Exoplanet System HD 209458: Transit Timing to Search for Additional Planets* ApJ 682 586 (2008)

[NIC] Niclass, C., Favi, C., Kluter, T., Gersbach, M., & Charbon, E., IEEE J. of Solid-State Circuits, 43, 2977 (2008)

[PAR] Marco Parrozzani, *progettazione opto-meccanica del fotometro astronomico IQuEYE,* master thesis (2008).

[PAT] Patruno, A., Wijnands, R., & van der Klis, M. ApJ, 698, L60 (2009)

[PRE] Prendergast, K. H., Spiegel, E., *Photon Bubbles*. A.Comments on Astrophysics and Space Physics, Vol. 5, p.43 (1973)

[PTK] W. Patrick Ambrose, Peter M. Goodwin, *Fluorescence photon antibunching from single molecules on a surface,* Chemical Physics Letters Volume 269, Issues 3-4, 2 May 1997, Pages 365-370

[QE1] Dravins, D., Barbieri, C., Fosbury, R., et al., in "The scientific requirements for extremely large telescopes" ed. P. Whitelock, B.Leibundgut, & M. Dennefeld, IAU Symp., 232, 502 (2006).

[QE2] Barbieri, C., Da Deppo, V., D'Onofrio, M., et al., in "The scientific requirements for extremely large telescopes" ed. P. Whitelock, B. Leibundgut, & M. Dennefeld, IAU Symp., 232, 506 (2006).

[QE3] Barbieri, C., Dravins, D., Occhipinti, T., et al., J. Mod. Opt., 54, 191 (2007).

[REC] I. Rech et al. *Optical crosstalk in single photon avalanche diode arrays: a new complete model*. Optics Express, Vol. 16, Issue 12, pp. 8381-8394 (2008).

[SAR] M.S. Sarazin, *Automated seeing monitoring for queue-scheduled astronomical observations.* Proc.SPIE Vol. 3125, 367 (1997)

[SCO] Scott, D. M., Finger, M. H., & Wilson, C. A. MNRAS, 344, 412, (2003).

[SRT] Sartoretti, Brown, Latham, Torres, *A search for substellar companions around nine weak-lined T-Tauri stars with the Planetary Camera 2 of the Hubble Space Telescope* A&A, v.334, p.592-598 (1998).

[TE1] Hobbs, Edwards and Manchester, *Tempo2, a new pulsar-timing package – I. An overview.* Monthly Notices of the Royal Astronomical Society, 369: 655–672. (2006).

[TE2] Edwards, Hobbs and Manchester T*empo2, a new pulsar timing package – II. The timing model and precision estimates.* Monthly Notices of the Royal Astronomical Society, 372: 1549–1574. (2006).

[US1] Uslenghi, Fiorini, Sarri *Wide dynamic range photon counting ICCD for ground-based astronomy.* Nuclear Instruments and Methods in

Physics Research Section A: Accelerators, Spectrometers, Detectors and Associated Equipment, Vol.518, Issues 1-2, (2004).

[US2] Uslenghi, Fiorini, Sarri, *A PC-ICCD for fast optical photometry* Mem. S.A.It. Suppl. Vol. 5, 407 (2004)

[WAL] Wallace, Peterson, Elliott, *The optical pulse profile of the Vela pulsar* Mont. Not. R. Astr. Soc. 190, 9P-11P. (1980)

[WOL] A.Wolszczan, D.A.Frail, *A planetary system around the millisecond pulsar PSR1257+12* Nature 355, 145-147 (1992)

Sitography

[*epw*] http://en.wikipedia.org/wiki/List_of_extrasolar_planets
[*esk*] http://www.vt2004.org/genfac/pubs/astclim/lasilla/index.html
[*elt*] http://www.eso.org/public/teles-instr/e-elt.html
[*eso*] http://www.ls.eso.org/sci/facilities/lasilla/astclim/
[*exp*] http://exoplanet.eu/searches.php
[*fli*] http://www.fli-cam.com/FLIproducts/MaxCam.htm
[*gem*] http://www.gemini.edu/node/11151
[*jba*] http://www.jb.man.ac.uk/ pulsar/crab.html
[*kod*] http://www.fli-cam.com/downloads/kaf-261e.pdf
[*kro*] http://xronos.gsfc.nasa.gov/
[*mpd*] http://www.microphotondevices.com/media/pdf/PDM_v3_3.pdf
[*owl*] http://www.eso.org/sci/facilities/eelt/owl/